NANOSTRUCTURED NOBLE METAL CATALYSTS FOR WATER-GAS SHIFT REACTION

by

Shuang Liang

Bachelor of Science, Chemical Engineering, Tianjin University, 2005

Master of Science, Chemical Engineering, Tianjin University, 2007

Submitted to the Graduate Faculty of

Swanson School of Engineering in partial fulfillment

of the requirements for the degree of

Doctor of Philosophy

University of Pittsburgh

2012

UNIVERSITY OF PITTSBURGH

SWANSON SCHOOL OF ENGINEERING

This dissertation was presented

by

Shuang Liang

It was defended on

January, 18, 2012

and approved by

Robert Enick, PhD, Professor, Department of Chemical and Petroleum Engineering

J. Karl Johnson, PhD, Professor, Department of Chemical and Petroleum Engineering

Alexander Star, PhD, Associate Professor, Department of Chemistry

Dissertation Director: Götz Veser, PhD, Professor, Department of Chemical and Petroleum Engineering

NANOSTRUCTURED NOBLE METAL CATALYSTS FOR WATER-GAS SHIFT REACTION

Shuang Liang, PhD

University of Pittsburgh, 2012

The water-gas shift (WGS) reaction ($CO + H_2O = CO_2 + H_2$) has attracted great research attention because of its applications in adjusting H_2/CO ratio for the Fischer-Tropsch process, providing hydrogen-rich streams for fuel cells and processing exhaust gases from automobiles. However, the current WGS process suffers from certain drawbacks of traditional catalysts, such as the toxicity of Fe-Cr-based catalysts and the instability/low space velocity of Cu-based catalysts. In the search for alternative catalysts to overcome these drawbacks, novel metal-based catalysts have been the focal point of most recent studies. The structures and properties of CeO_2, on which the rate determining step proceeds (i.e. water dissociation), are believed to fundamentally impact the performance of this catalyst.

In this project, the objective is to develop a rational design of novel metal-based WGS catalyst which combines high activity with stability against sintering and poisoning. In order to achieve this objective, we have prepared pure and mixed lanthanum-cerium oxide supports, and investigated the effects of these compositions and morphologies to the material's reducibility and catalytic activity. For the composition, it was found that a proper amount of La doping can improve the WGS activity by tailoring the Ce^{4+}/Ce^{3+} ratio. When we change the morphology, the CeO_2 nanorods were observed to be a better support for Au than the CeO_2 nanoparticles. The outstanding performance of the CeO_2 nanorods were attributed to its predominantly exposed

crystal plane {110}, which is more active to be reduced and to form oxygen vacancies than the {111} exposed by CeO_2 nanoparticles.

After obtaining the high activity WGS catalysts, we have improved our catalysts against particle sintering and S-poisoning. Surface decoration technique has been applied to prepare layered La_2O_3/M/CeO_2 (M = Au, Pt) with sulfur resistance and regeneration ability during cyclic sour WGS. On one hand, La_2O_3 has been demonstrated as a protective overlayer against H_2S in syngas feedstocks in addition to its stabilizing effect to prevent Au nanoparticles sintering. On the other hand, reducible CeO_2 supports enable complete regeneration of sulfur-poisoned Pt catalysts due to the strong metal support interaction (SMSI).

TABLE OF CONTENTS

LIST OF TABLES

LIST OF FIGURES

ACKNOWLEDGEMENTS

Firstly, I would thank Dr. Götz Veser for all his helpful advice, inspiring discussion, and constant support during my entire Ph.D. study. It has been an absolute pleasure to work, learn and grow in his group. I cordially thank all of my committee members Dr. Enick, Dr. Johnson and Dr. Star for providing me with many helpful insights on my work.

I would also thank my lab mates Anmin Cao, Yanan Wang, Tom Sanders, Yi Zhang, Lu Zhang, Michelle Najera, Sen Liu, Saurabh Bhavsar and Karen Uffalussy for their help and cooperation in the lab.

In addition, I would thank the staff of the Chemical Engineering and Materials Science departments at Pitt, especially Al Stewart, Cole Van Ormer and Sushen Tang for their great help.

Furthermore, I would thank my friends at Pitt, especially, Jiamin Wu, Chuan Yang and Anmin Cao, who provide the warmest help when I came to the U.S. from China 5 years ago.

Last but not least, I can never adequately express my gratitude to my family. My parents, who constantly support me, are the two most influential people in my life. Their love and wisdom encouraged me to overcome many obstacles. To my wife, Ping, I am endlessly grateful to you for your entire warm support and indefinite sacrifices which help me to finish this dissertation work.

1.0 INTRODUCTION

1.1 NANOCATALYSIS

The recent advances in the controlled synthesis and characterization of materials on the nanoscale, in combination with the insights from developments in surface science over the past few decades, have resulted in a dramatic improvement in our understanding of how catalysis works on a molecular level and how catalysts can hence be rationally designed towards their desired functionality. It is frequently claimed that catalysis has always been a "nano-science". While this statement is certainly true, it misses the crucial aspect that catalysts were more "accidental" nanomaterials than rationally designed as such, and it is this capability to rationally design functional materials – and catalysts in particular – that has recently allowed catalysis to transition from a "black art" to a science [1, 2].

The defining element of a "nanocatalyst" is hence not the actual size of the particle, but rather the rational design of catalytic functionality on the nanoscale, which itself is often embedded – or even an integral part – of a material with dimensions well beyond the nanometer regime. Such a functionality can be added, for example, via functional groups, careful design of the size or shape of catalytically active particles to expose a large fraction of highly active surface orientations or highly undercoordinated sites (such as edges, steps, and kinks), or via electronic modification via quantum confinement effects in ultra-small particles or via metal-

support interactions. In either case, a major challenge lies in understanding of what constitutes the active site for any specific reaction, in the carefully controlled synthesis of this site or ensemble, and in incorporating this "motif" into the larger scale of a final catalyst. The latter is further constrained by the fact that – beyond catalytic functionality – an efficient catalyst must also provide for fast and easy access to this functional site, i.e. it must allow for efficient mass transfer of reactants and products to and from the active site. This can be considered a complementary goal to the (nano)structuring of a catalyst for functionality: Rather than structuring the catalyst surface, it requires structuring of the void space. For example, ordered mesoporous materials, such as SBA-15, which provide controllable and uniform pores within the size range of 5-30 nm, offer well-suited environments for anchoring catalytic nanoparticles [3, 4]. Similarly, irregular oxide matrices, such as barium-hexaluminates (BHA) with an irregular, but well defined network of interconnected pore necks and pore cages, allow fast transport of reactants and products while limiting the mobility of the embedded nanoparticles [5-9].

Finally, since the vast majority of such designed nanomaterials depend on non-equilibrium shapes and hence are subject to thermodynamic driving forces that acts towards destruction of the carefully designed functionality, a critical aspect of transitioning these model nanocatalysts to technical application is stabilization of the structure [5]. This is an aspect that has only recently found significant attention in the literature, but will be crucial in order to harvest the vast potential of nanomaterials for industrial catalysis. For example, even at the mild temperatures typical for low-temperature water-gas-shift (250-450 ^{o}C) or even CO oxidation (<250 ^{o}C), the stability of uncapped metallic nanoparticles, such as Au, is critical and strongly depends on the preparation and reaction conditions [10].

1.2 WATER-GAS SHIFT (WGS) REACTION

The Water-Gas Shift (WGS) reaction is one of the most fundamental reactions for fuel processing in the current petrochemical industry, and intensive efforts towards utilization of biorenewable fuels will only further increase the importance of this reaction. WGS has attracted great attention because of its application in adjusting the H_2/CO ratio for Fischer-Tropsch processes [11, 12], providing hydrogen-rich streams for fuel cells [13, 14] and processing exhaust gases from automobiles [15-18].

Currently, the primary industrial process for hydrogen production is steam reforming of hydrocarbons:

$$C_nH_m + n\ H_2O \leftrightarrow n\ CO + (n\text{-}m/2)\ H_2 \qquad (1)$$

However, steam reforming results in typical CO concentrations of 1-10% in the effluent stream, which poses significant problems for many downstream processes for which CO is a strong catalyst poison. Hence, a WGS step is critical to adjust the CO to hydrogen ratio and/or to provide clean hydrogen:

$$CO + H_2O \leftrightarrow CO_2 + H_2 \qquad \Delta H = -41.1\ kJ/mol \qquad (2)$$

WGS is an exothermal reaction and thus constrained by thermodynamic equilibrium limitations at high temperatures. The decreasing equilibrium constant with increasing temperature is given (Eq. (3)), for example, by the following correlation in the temperature range of 315-480 ^{o}C [19, 20]:

$$K_p = exp\left[\left(\frac{4577.8}{T}\right) - 4.33)\right] \qquad (3)$$

At low temperatures, the thermodynamics are favorable, but the reaction is constrained by slow kinetics. Current industrial WGS processes therefore utilize a two-stage process

involving a high-temperature shift (HTS, 350-450 ^{o}C, typically with Fe-Cr-based catalysts) and a low-temperature shift (LTS, 190-250 ^{o}C, typically with Cu/ZnO/Al_2O_3 catalysts) in order to take advantage of fast reaction kinetics at high temperature and high equilibrium conversion at low temperature.

However, these current industrial catalysts suffer from several drawbacks. Most importantly, due to the relatively low reactivity of these catalyst and hence low space velocities, in particular for the LTS step (GHSV = 3,000-5,000 h^{-1} for LTS and 10,000-15,000 h^{-1} for HTS) [21], large catalyst bed volumes are necessary. Furthermore, the Cr^{+6} in HTS catalyst is highly toxic and harmful for human health and the environment, while the Cu-based LTS catalyst is pyrophoric if exposed to air and hence requires careful activation before use. These issues pose significant concerns and conflict in particular with the requirements of WGS applications in emerging technologies such as fuel cells for use in transportation. Hence, much effort is focused on the development of alternate WGS catalysts which combine high activity at low temperatures with good stability at high temperatures, i.e. operability over a broad temperature range.

Mechanistically, two reaction pathways have been proposed for WGS on oxide-supported metal catalysts: A redox mechanism, in which CO binds to the active metal component of the catalyst and is then oxidized by oxygen supplied from the support, followed by reoxidation of the support by H_2O, releasing H_2 [22-24]; and an associative mechanism, in which a formate species is first formed from absorbed CO and dissociated hydroxyl groups, and then decomposes to CO_2 and H_2 [25-27]. Although it is difficult to conclusively rule out one or the other of these mechanisms through direct experimental investigations (largely due to the uncertainty whether surface formates are spectator species or reaction intermediates), most evidence points towards the redox mechanism as the dominant reaction pathway over typical WGS catalysts. For

example, recent studies via steady-state isotopic transient kinetic analysis (SSITKA) coupled with in-situ spectroscopy showed that LTS over Pt/Ceria at 300 ^{o}C proceeds largely via the redox mechanism, and to a lesser extent via an associative mechanism [28, 29]. At even lower temperature (160 ^{o}C), combined in-situ DRIFTS and computational studies suggest that formates are indeed spectator species, at least over Cu- and Pt- based WGS catalysts [29].

From this insight into the reaction mechanism, which requires a synergetic action between the metal nanoparticle and the (active) support, it can be concluded that the interface between the CO-bonding metal phase and the oxygen supplying support will play a major role in WGS as the location of the active sites for the oxidative half step in the reaction. This understanding hence yields a rational design target for a WGS catalyst via optimization of the metal-support interface on the nanoscale.

1.3 ACTIVE METALS

While a wide variety of metals have been investigated for WGS, most recent studies on nanocatalysis have focused on Au and Pt. [30] A direct comparison between the various results reported in the literature is difficult, if possible at all, due to the very different reaction conditions, catalyst formulations, feed compositions, and reactor configurations used. However, Schuurman et al. conducted a direct comparative evaluation of several different metal/oxide WGS catalysts, the results of which are summarized in Figure 1 [31, 32]. It is worth noting that the most active catalysts in their study, such as Au/CeO_2 and Pt/TiO_2, are also the most investigated ones in recent work.

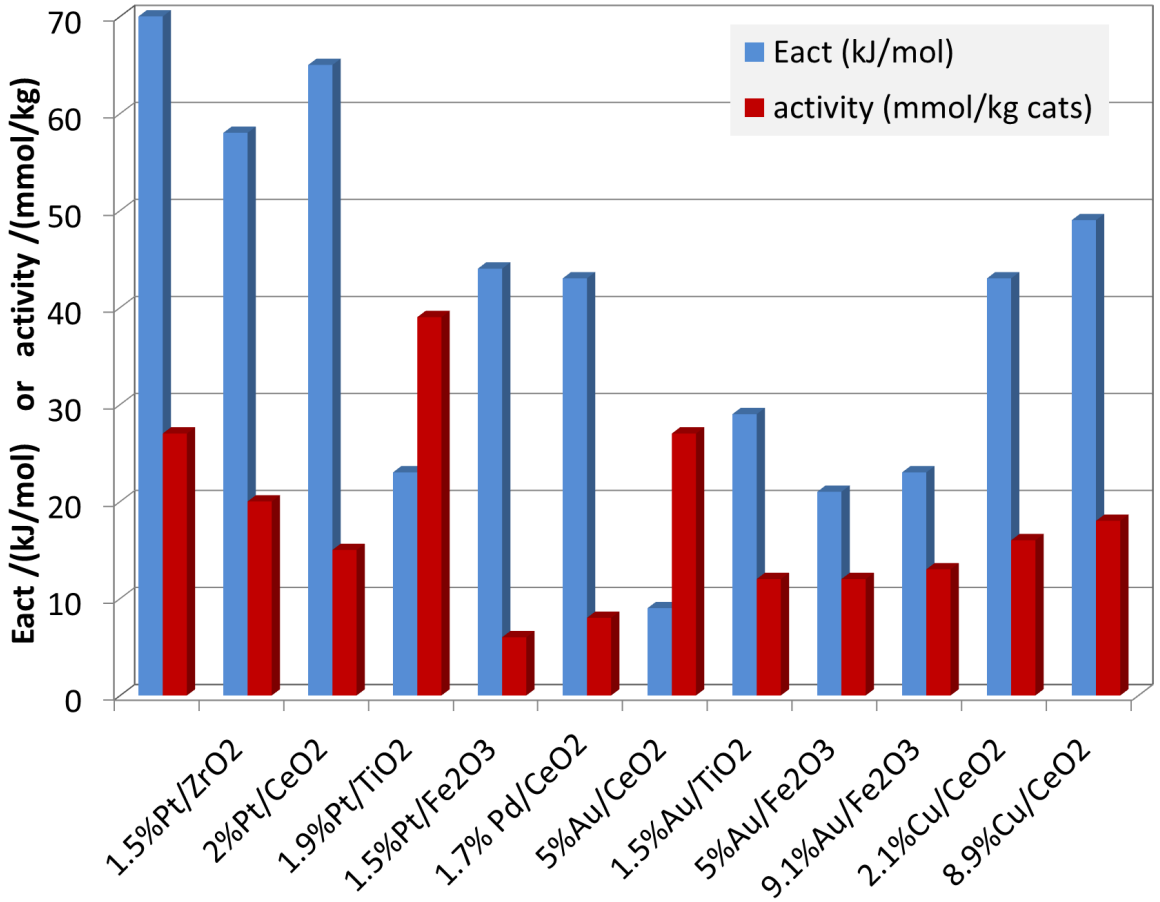

Figure 1. Apparent activation energies and catalytic activities (at 300 ^{o}C) of Pt, Au and Cu based catalysts. Activity is defined as $F_{CO} \times X_{CO} / W_{cat}$, in which F_{CO} is the molar flow rate of CO, X_{CO} is the fractional conversion and W_{cat} is the weight of catalyst. Adapted from [32].

1.3.1 Gold

Gold supported on metal oxides has been widely investigated as catalyst for CO oxidation and, more recently, for WGS. This interest is due to the - in comparison to Pt - lower cost and relatively high WGS activity at temperatures as low as 250^{o}C. Although Pt is a more active oxidation catalyst than Au, typical Pt catalysts show a higher activation energy in WGS (see

Figure 1) and hence their activity drops rapidly with decreasing temperature, making Au the preferred low-temperature catalyst.

As bulk Au is known to be the least reactive among the transition metals, Au must be highly dispersed as small nanoparticles on the oxide support, and this size effect of Au nanoparticles has been the object of intense investigations [33]. In fact, the early reports by Haruta and coworkers that Au with particle sizes below 5 nm is highly active for CO oxidation - one half-step of the WGS reaction - can be regarded as the starting point of the rapidly exploding field of "nanocatalysis" [34-37]. The importance of these small Au particle sizes was confirmed in a number of later investigations. For example, Hua et al. reported high activity of Au-Fe_2O_3-MO_x catalysts at temperature as low as 160^oC for Au particles size around 2 nm [38]. More recently, Herzing et al. extended the study of active Au particle size to sub-nanometer range for CO oxidation [39]. After careful examination of iron supported Au catalysts, they deduced the 0.5 nm bilayer Au clusters are responsible for the high activity, rather than the 0.2 - 0.3 nm monolayer clusters.

Given the overwhelming number of reports on this topic alone, it is fascinating to see that ~20 years after Haruta's initial reports the current understanding of this catalyst system is still incomplete, with many contradictory reports in the published literature throughout these years. One of the most controversial points has become the very particle size effect that started all these investigations: While many reports on particle-size dependent Au reactivity in CO oxidation and WGS followed Haruta's early reports, Flytzani-Stephanopoulos and coworkers found that Au nanoparticles appear not to be the carriers of the reactive site in WGS at all [40, 41]: Removing Au nanoparticles quantitatively via NaCN leaching had no effect on WGS activity. They concluded that remaining, atomically dispersed Au cations are the true reactive site. This

conclusion seems to agree with recent computational studies that found supported $Au^{\delta+}$ has sufficiently strong CO chemisorption ability, allowing WGS to occur on an ensemble of several $Au^{\delta+}$ in the vicinity of an O vacancy [42]. However, several other groups claimed the nonionic or metallic Au contributes significantly, if not exclusively, to the activity of WGS [43-47]. For example, X-ray absorption near edge structure (XANES) studies by Jacobs et al. showed that the partial reduction of ceria, which is necessary for generating bridging OH groups in WGS, is not facilitated except in the presence of Au^0 [43]. Similarly, Rodriguez and coworkers conducted a series of investigations on Au/CeO_2 in WGS and found that AuO_x was completely transformation to metallic Au at reaction conditions, thus ruling out cationic $Au^{\delta+}$ as the active species [44].

More recent work from Flytzani-Stephanopoulos and coworkers seems to allow reconciliation of these contradictory findings, at least to some degree [48]: They probed the oxidation state of Au in low-loading Au/ceria catalysts (<1 wt% Au) in WGS by combining in situ XANES and extended X-ray absorption fine structure (EXAFS) studies in-situ at 100-200 ℃, and found that Au in the fresh catalyst was indeed atomically dispersed. However, at reaction conditions (5% CO, 3% H_2O, balance He), the oxidized gold species were reduced and slowly agglomerated as indicated by an increase in the Au-Au coordination number from zero in the fresh catalyst to 6.5 ± 2.4 after use at 100 ℃ and 8.7 ± 1.5 after 200 ℃. The maximum WGS activity was observed on fully dispersed Au-O-Ce catalyst, i.e. the fresh catalysts. The loss of surface oxygen, corresponding to the deactivation, can be reverted by oxygen treatment at 400 ℃, resulting in a full recovery of the initial activity. Remarkably, they also observed that the extent of reduction of the oxidized Au species depends strongly on gas composition: Lowering the reduction potential of the reaction gas mixture resulted in higher oxidation of the Au, which

correlated with an increase in activity. Overall, these findings thus allow reconciliation of the previous contradictory reports: They confirm the typically metallic state of Au at WGS conditions, but correlate the most active state of the catalyst with the presence of a highly dispersed cationic species.

However, a most recent report by Daly et al. re-opens the debate again by claiming that metallic Au is active species "in contrast with the recent work of Deng et al." [45]. They confirmed that the cationic gold species is highly unstable and will convert to Au^0 at temperatures as low as 200 ^oC. However, they argued that, at WGS reaction conditions, it is unlikely that the very small number of cationic gold is responsible for the activity since the change of this species does not match the long-term deactivation of the catalysts, while the Au^0-CO does correlate at all their tested conditions.

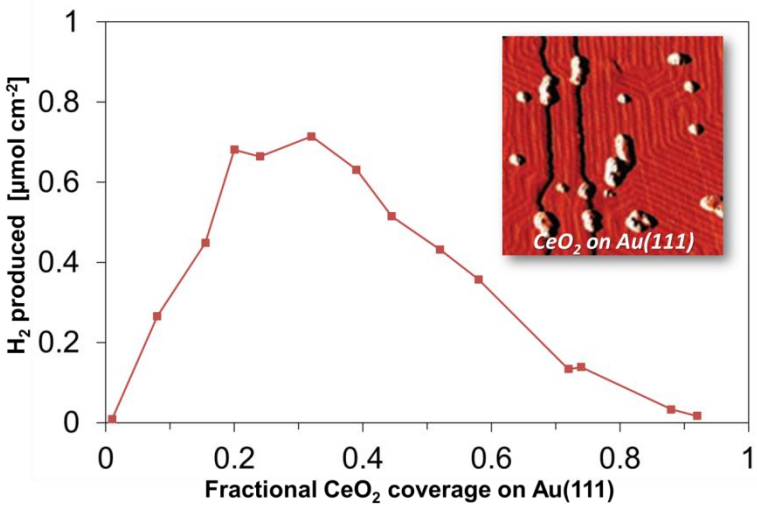

Figure 2. WGS activity (shown as H_2 production rate) for an "inverted" WGS catalyst in which ceria clusters were deposited onto a Au (111) surface (inset shows a STM image of a 100 by 100 nm section of the catalyst surface). Maximum activity is observed for intermediate surface coverage, emphasizing the importance of the ceria-Au interface for WGS activity. Adapted from [49].

In addition, it is not just the state of the Au nanoparticles that needs careful control and monitoring in order to deconvolute the complex and contradictory reports on this reaction system in the literature: In a particularly elegant approach, Rodriguez and coworkers prepared "inverted catalysts" by supporting ceria and titania nanoparticles on extended Au(111) single crystal surfaces (Figure 2) [33, 49-53]. Despite the fact that extended Au(111) surfaces—essentially bulk Au—are known to have very little catalytic activity, these inverted catalysts were highly active WGS catalysts. A combination of experimental and computational studies showed that a moderate coverage of the Au(111) surface with oxide nanoparticles resulted in the most active catalyst state, at which ~14–17% of the O atoms in the CeO_2 and TiO_2 NPs were removed to produce partially reduced ceria and titania. The degree of reduction decreased again substantially when the surface coverage of oxide NP on Au became too high (>35%), suggesting that the WGS reaction "likely involves O vacancies that are near oxide-gold interfaces", i.e. it involves cooperative effects between the nanoparticles and the Au support, implying that the WGS activity of oxide supported Au catalysts is strongly correlated with the metal/oxide interface and the state of the supporting oxide, rather than the state of the Au nanoparticles, although one correlation certainly does not necessarily exclude the other.

1.3.2 Platinum

As mentioned above, Pt is generally a more active oxidation catalyst than Au. However, due to the high activation energies reported for typical Pt catalysts (see figure 1), the low temperature (180–300 ^{o}C) activity of Pt-based WGS catalysts is generally lower than that of Au-based catalysts. Hence, a significant number of studies explored different approaches to improve the low-temperature activity of Pt-based catalysts, including the addition of metal promoters (such as

Re [54-58], Na [59-62], Mg [63], V [64] and Mo [65]) and the incorporation of metal oxides (ZrO_2 [66], CeO_2 [67-69], TiO_2 [70]). For example, Kim et al. investigated ceria-promoted Pt/TiO_2 prepared by a single step co-impregnation of platinum and ceria, and found that - in contrast to an unpromoted Pt/TiO_2 catalyst - this catalyst shows excellent low temperature activity and good stability during long time operation and the start-up and shut-down processes [67]. They attributed the high catalytic activity to enrichment with active CO chemisorption sites, which include not only Pt but also ceria in proximity to Pt.

A more complex Pt nanocatalyst with improved low temperature WGS activity was reported by Hegde and coworkers [66, 70]. They prepared and compared several mixed oxide catalysts containing titania, ceria, and platinum. Temperature programmed reduction (TPR) and XPS study of $Ce_{1-x}Ti_xO_2$ (x = 0.1–0.4) shows complete reduction of Ti^{4+} to Ti^{3+} and reduction of ~ 20% Ce^{4+} to Ce^{3+} compared to 8% Ce^{4+} to Ce^{3+} in the case of pure CeO_2 below 675 ℃, indicating the substitution of Ti ions in CeO_2 enhances the reducibility of CeO_2. Catalytic activity of $Ce_{1-x-y}Ti_xPt_yO_{2-x}$ is higher than that of $Ce_{1-x}Pt_xO_{2-x}$, and the hydrogen uptake of ionic Pt in the mixed oxides is much higher than the of Pt nanoparticles (H/Pt ratio = 4~5 for lattice Pt ion vs. 0.078 for 8nm Pt nanoparticles) [70]. In WGS, both platinum substituted zirconia and platinum substituted ceria-zirconia mixed oxides reach equilibrium CO conversion below 300^oC [66]. These results suggest that, similar to Au-based WGS catalysts, the oxidation state of the metal plays a crucial role for WGS catalysis, with ionic species showing higher reactivity than metallic ones.

Beyond these oxide-based studies, alkali promotion of Pt catalysts results in excellent WGS activity, as already reported more than 20 years ago without, however, truly elucidating the reason for this promoting effect [59]. Two recent studies started to shed some light on this, albeit

with very different conclusions. Pigos et al. used DRIFTS to demonstrate that Na results in the activation of C-H bond scission and can hence accelerate the decomposition of surface formate intermediates, which is considered as rate determining step based on the formate mechanism [60]. In contrast to that, Zhai et al. reported a stabilizing effect of Na via formation of Pt-OH_x species with high activity in WGS reaction [61]. HAADF/STEM analysis showed that a small amount of alkali metal (Na or K) stabilizes atomically dispersed, oxidized Pt species (Pt-OH_x), which is suggested to be the active site for WGS. Interestingly, the highly active Pt-OH_x species do not require reducible oxide supports (such as ceria). This is further confirmed via kinetic studies which yield similar activation energies (albeit different activity) for all alkali-stabilized catalysts with non-reducible supports, with a value that is similar with alkali-free Pt-based catalyst such as Pt-CeO_2, Pt-TiO_2 and Pt-ZrO_2 (E_{act} = 70±5 kJ/mol). This suggests that the active site is identical between these catalysts, and that the difference in (absolute) reaction rates can be attributed to the different number of active sites (Pt-OH_x). This is further confirmed by recent reports by Zhu et al. on Na-promoted Pt/TiO_2, i.e. an alkali promoted Pt on a reducible support [62]. For this catalyst they found that 4% Na addition results in an increase of reaction rate and turn-over-frequency (TOF) by about one order of magnitude compared with a Na-free Pt/TiO_2 at 300 ^{o}C. In a good agreement with Zhai et al.'s work, the strong interaction between Pt-O-Na was proposed to be the reason of the reactivity enhancement, and similar activation energies (74-80 kJ/mol) were found for both Na-free and Na-promoted Pt catalysts.

1.4 OXIDE SUPPORTS

The above discussion already demonstrated that the support plays a crucial role in WGS catalysis, independent of which active metal is chosen, albeit the role varies from stabilizing an active metal species, to acting as electron donor/acceptor, and finally being an quasi-independent co-catalyst for part of the overall reaction (by supplying oxygen for CO oxidation and/or directly catalyzing the reduction of water). Hence, a wide range of (mostly reducible) oxides have been studied extensively in recent years (CeO_2 [23, 24, 53, 71-78], TiO_2 [55, 62, 79, 80], ZrO_2 [52, 57, 60, 65, 81-83]) and have been shown to be typically more "active" compared with nonreducible oxides (SiO_2, Al_2O_3, MgO) [84].

Most of the recent work on reducible oxides has focused on compositional tailoring and morphological tailoring of the catalyst on the nanoscale in order to improve the reducibility of the oxide support. The addition of promoters to the supporting oxides was shown to be an effective method to tailor their reducibility [82, 85-88]. For example, based on computational work, Balducci et al. reported the reduction energy of CeO_2 can be tailored by various dopents, such as La, Mn, Sc, Gd and Y [86]. Ricote et al. showed the doping of Zr to CeO_2 can not only decrease the reduction temperature of CeO_2, but also increase the decomposition rate of formate, and hence improve the WGS activity of Pt-based catalysts [82].

On the other hand, in addition to the compositional tailoring of oxide supports for WGS, morphological control on the nanoscale has been shown to have a strong impact on the catalytic activity of nanomaterials in WGS. Early work focused on the size-dependency of catalytic activity of reducible oxides (CeO_2, TiO_2) in CO oxidation and WGS [80, 89, 90]. The size dependence could be traced back to an increase in defect density with decreasing particle, creating more oxygen vacancies and hence Ce^{3+} in the ceria lattice, which have been shown to be

the active redox sites in WGS [89]. Computational studies further confirmed that the metal-oxygen binding energy in ceria nanoclusters increase roughly linear with increasing cluster size towards the bulk limit, and that strong lattice expansion in these nanoclusters is due to the formation of oxygen vacancies [91]. Furthermore, partially reduced Ce^{3+} was found to preferentially occupy undercoordinated edge and corner sites on the nanoparticles, indicating a similar size-dependent mechanism as reported for Au nanoparticles [92].

Beyond size-dependence, a strong dependence of the WGS activity on the shape of the active oxide support was established as well [93, 94]. Zhou et al. reported enhanced CO-oxidation activity of ceria nanorods prepared by hydrothermal synthesis due to preferential exposure of highly reactive {110} crystal planes, which are more active than closely packed {111} planes preferentially exposed by near-spherical ceria nanoparticles [95]. More recently, Si *et al.* prepared nanostructured ceria with different shapes (polyhedral, rods, nanocubes) via controlling temperature and pH during the hydrothermal synthesis, followed by Au loading via deposition-precipitation [94]. Again they found a strong correlation between particle shape and WGS activity, with ceria nanorod-supported Au showing higher reactivity than nanoparticle and nanocube based catalysts. This shape dependence could be attributed not only to the formation energy of anion vacancies (i.e. oxygen defects), but also to differences in lattice strain on the different crystal planes.

Another approach towards using nanostructuring methods to improve WGS activity of nanocatalysts is based on the insight that the reactive sites are located at the metal-oxide interface, where metal-bound CO can react with oxide-supplied oxygen. Hence, one can expect that maximizing the metal-support interface should result in increased reactivity. This approach was pursued by several research groups via synthesis of core-shell nanocatalysts, such as

$Pt@CeO_2$ [96-99] and $Pd@CeO_2$ [100-102]. Yeung et al. reported that $Pt@CeO_2$ core-shell catalysts exhibit excellent WGS activity and selectivity suppressing methanation as undesired side reaction [96-99]. They proposed that encapsulation of metal nanoparticles in a core-shell geometry creates a unique metal-oxide interface, which results in an electronic promotion of the CeO_2. Cargnello et al. also prepared $Pd@CeO_2$ via a microemulsion-templated approach and demonstrated enhanced stability of this catalyst albeit at the challenge of improving accessibility of core-shell structure [100, 101].

While all the above catalysts rely on the use of reducible oxides, based on the cooperative mechanism where the metal acts as CO sorbent and the oxide as the redox center for the reaction, the significance of reducible supports was challenged recently by several reports, which attribute the activity to the M-O or M-OH complexes [71, 103]. Kim et al. found a strong promoting effect of oxygen pre-coverage on Au(111) surfaces on low-temperature CO-oxidation by H_2O (i.e. WGS) which seems to indicate that no reducible oxide (or any support, for that matter) is required for WGS [103]. As already discussed further above, Flytzani-Stephanopoulos and coworkers carefully examined Pt-based WGS catalysts on different supports and found similar activation energies (70 ± 5 kJ/mol), which implies identical rate limiting steps and suggests that the different reaction rates are mainly due to differences in metal dispersion rather than the different supports [61]. Furthermore, they also demonstrated that this concept can be extended onto Au catalysts, which, in contrast to Pt, had to-date been considered strongly dependent on the presence of a reducible support. Au-CeO_2, -ZnO, and -Fe_3O_4 nanoshapes were tested in WGS, and showed similar apparent activation energies [71]. They attributed the differences between crystal planes of different oxides to the different concentrations of oxygen defects, in agreement with the above discussed interpretations, although the role of the oxygen defects was proposed to

be the stabilization of Au-O active species rather than in a direct participation in the WGS reaction.

1.5 STABILITY

Deactivation is a major concern for catalysis in general, and emerging catalysts based on carefully controlled nanostructures are often even more sensitive to stability issues than conventional technical catalysts. This issue is further exacerbated by the expensive, multi-step synthesis methods used for the production of many nanostructured catalysts, and the reliance on expensive noble metals (Au and Pt) for most emerging WGS catalysts.

Major reasons for deactivation in WGS include sintering of metal nanoparticles [22, 54, 104] and poisoning of catalyst by fuel contaminants, most notably sulfur (which needs to be kept below 0.1 ppm for current Cu-based LTS catalyst, for example[21]).

1.5.1 Sintering

Sintering, i.e. agglomeration of metal nanoparticles, resulting in the loss of surface area and/or active sites specific to the nanostructures, is well established in heterogeneous catalysis. However, the well-known melting point depression on the nanoscale exacerbates this problem significantly for catalysts which rely on well-defined metal nanoparticle. Hence, even at the comparatively low temperatures of low-temperature shift (LTS), many metals, including in particular Au, suffer from rapid sintering [105]. Buffat and Borel derived in their pioneering

work a correlation (Eq. (4)) for the size dependence of the melting point melting ($T_m(r)$) on particle radius r [106]:

$$\frac{T_m(r)}{T_m(0)} = 1 - \frac{2}{\rho_s L}\left\{\gamma_s - \gamma_l\left(\frac{\rho_s}{\rho_l}\right)^{2/3}\right\}\frac{1}{r_s} \qquad (4)$$

where ρ and γ represent density and surface free energy of the solid (s) and liquid (l), L the molar heat of fusion, and $T_m(0)$ the bulk melting point, respectively. Based on this equation and in good agreement with experimental observations, the melting point of 2 nm Au nanoparticles is lowered by several hundred degrees below the bulk value, down to ~600K. Since sintering sets on temperatures well below melting (as low as 0.3–0.5xT_m, often correlated with the empirical Tamman and Hüttig temperatures [5]), this imposes a stringent stability limit on catalysts based in particular on Au nanoparticles.

Beyond temperature alone, the presence of relatively high concentrations of water in WGS is another reason for the sintering of metal nanoparticles [107]. Goguet et al. recently reported that the hydrolysis of Au nanoparticles starts at temperatures as low as <250 ^{o}C, resulting in reduced metal-support interactions [107]. DFT calculations confirmed progressive detachment of Au nanoparticles from the support surface during LTS through a water-assisted dewetting mechanism.

Generally, two approaches exist to overcome the stability limits for catalysts, and both have been broadly explored for WGS catalysts: On one hand, the catalyst can be stabilized via modification of the metal nanoparticle through alloying [108, 109], on the other hand, engineering of the support composition and structure can yield improved stability [6-8, 96, 100, 102, 110].

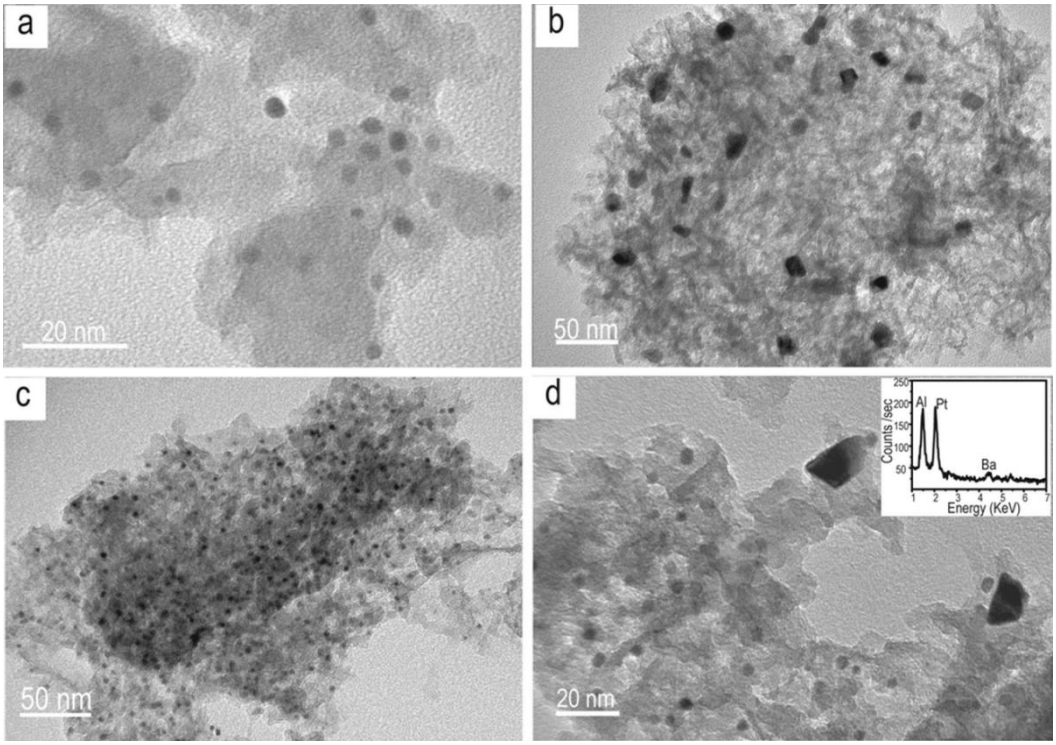

Figure 3. Stabilizing metal nanocatalyst via alloying: TEM images for Pt-BHA calcined at (a) 500 ℃ and (b) at 600 ℃; (c) PtRh (1:1) calcined at 850 ℃; and (d) PtRh (3:1) calcined at 700 ℃. The inset is the EDAX pattern of the larger nanoparticles in (d), showing their identity as pure Pt. Adapted from [5, 108].

We have recently shown that Pt nanoparticles can be stabilized to very high temperatures in a straightforward way via alloying with Rh: PtRh alloy nanoparticles with a Pt:Rh=1:1 atomic ratio exhibit exceptional stability up to 850 ^{o}C, compared to only ~500 ^{o}C for monometallic Pt (Figure 3). More interestingly, however, the alloy nanoparticles do not simply sinter at high temperature, but selectively 'bleed out' the lower melting point Pt (i.e. Pt selectively diffuses out from the PtRh particles), stabilizing the (Rh-enriched) alloy nanoparticles in a self-adaptive way: After high-temperature treatment, two distributions of nanoparticles are identified in TEM: larger Pt nanoparticles (>20 nm), separated from bimetallic nanoparticles and agglomerated due to the sintering; and small nanoparticles (~3 nm) with increased Rh content. As a result, the original nanoparticle population remains intact (albeit with slightly changed composition), and the catalyst shows excellent stability.

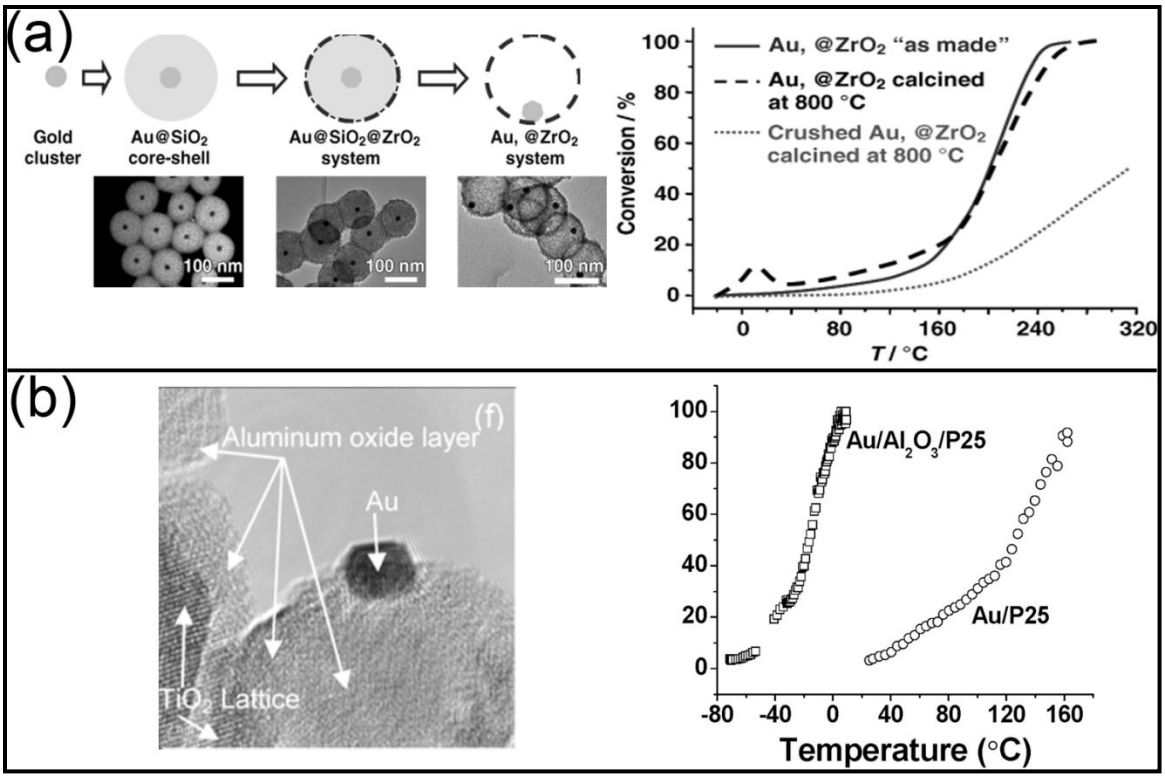

Figure 4. Stabilizing the metal nanocatalyst via nanostructuring of the oxide: (a) Synthesis scheme and corresponding TEM images of hollow ZrO_2-encapsulated Au nanoparticles (left), showing no significant change in activity after calcination at 800 ^oC (right). Adapted from [111]. (b) High-resolution TEM image of amorphous Al_2O_3-modified Au/TiO_2 (left). The modified catalyst exhibits better CO oxidation activity after high-temperature calcination than the unmodified catalyst, indicating improved thermal stability (right). Adapted from [112].

Alternatively, stabilization via support regulation has been explored by several groups, including encapsulation [96, 97, 99-102, 111] and caging of the metal nanoparticles in a carefully nanostructured support [5, 9]. Pablo et al. prepared $Au,@ZrO_2$ core-shell catalyst (see Figure 4 (a)) and demonstrated enhanced thermal stability up to 800 ^oC [111]. The porous zirconia coating allows access to the encapsulated metal nanoparticle, while encapsulating the particle and hence suppressing particle migration and agglomeration. In a slightly different approach, Dai and coworkers found that surface modification of TiO_2 by amorphous Al_2O_3 can improve the thermal stability of Au nanoparticles without a significant effect on activity (Figure 4 (b)) [112]. In an extension of this approach, they recently carefully controlled deposition of a

layer of SiO_2 on Au/TiO_2 via atomic layer deposition (ALD) results in improved sintering resistance of the catalyst [113, 114]. First-principles density-functional calculations showed that the deposited SiO_2 slows the atomic surface diffusion and thus inhibits Au nanoparticle growth/sintering [114]. The same approach was used recently by Xia and coworkers for Pt/TiO_2 [115]: A porous silica layer restricted the Pt on TiO_2 and hence stabilized the catalyst up to 750 ^oC.

However, it should be mentioned that most studies use a "shortcut" approach to test stability: The catalysts are simply calcined at high temperature in air or Ar, followed by reactivity tests in relatively low-temperature reactions (such as CO oxidation), rather than conducting actual long-term stability test under high-temperature reaction conditions [111-115]. As a result, these tests can probe stabilization against sintering induced by particle mobility, but not against other types of deactivation, such as gradual surface reconstruction of metal nanoparticles [115] or the weakening of metal-support interactions [107].

1.5.2 Poisoning

Last, but not least, WGS catalysts can deactivate not only due to site blocking by reaction intermediates or spectator species, but also due to contaminants in the reactant stream. Among those, sulfur is generally the main concern, as typical syngas streams result from gasification, partial oxidation, or reforming of fossil fuels, which contain significant amounts of sulfur. Sulfur poisoning can eventually lead to the shut-down of LTS, since Cu-based catalysts can be poisoned even by very low sulfur concentrations [116, 117]. Although molybdenum sulfide based catalysts have been developed as sulfur tolerant WGS catalysts, these catalysts actually require a minimum sulfur concentration in the fuel stream in order to maintain their activity, which again

limits their application mainly to production of syngas from coal and heavy oil gasification [118].

While sulfur poisoning has been a well-known issue for WGS catalysis for a long time, the mechanism of poisoning is still under investigation [119-123]. The main challenge for the study of S-poisoning on nanocatalysts in particular is the extremely low amount of S which can cause complete deactivation but which is too low to be identified by techniques such as XPS [120]. Although ICP-MS or XRF (X-ray fluorescence spectroscopy) can be used to perform elemental analysis for extremely low S concentrations, these techniques cannot provide "deeper" information such as oxidation states. A recent study via X-ray absorption near edge structure (XANES) spectroscopy performed by Chen et al. identified the sulfur species on the surface of CeO_2-Al_2O_3-supported Ni and Rh-based catalysts and hence the deactivation mechanism of these catalysts in steam reforming [120]. Different sulfur compounds (metal sulfide and organic sulfide on Ni, sulfonate and sulfate on Rh, and organic sulfide and sulfate on supports) were found. Their study also suggested that, at least in steam reforming, the sulfur is only responsible for the initial deactivation of Ni-based catalysts, while carbon deposits contribute to the subsequent deactivation.

One widely adopted approach against S-poisoning is incorporation of protective and sacrificial metals, which can increase the sulfur tolerance of noble metal catalysts [124, 125]. For example, recent work by Strohm et al. suggested that a bimetallic Ni-Rh catalyst has a higher S-tolerance in steam reforming than monometallic Rh on CeO_2-Al_2O_3 [124]. The addition of 5-10% Ni and formation of the bimetallic Ni-Rh catalyst significantly delays the deactivation until all the surface Ni are saturated by sulfur (S_{fuel} : $Ni_{surface}$ = 0.59). The authors suggest that either

the preferential poisoning of Ni or the strong interaction between Ni and Rh, resulting in S transfer from Rh to Ni, is the mechanism of protection of Rh by Ni.

S-poisoning of noble metal based nanocatalysts in WGS has been given very little attention to-date, and the few existing studies focus on Pt- and Pd-based catalysts, despite the well-known affinity of Au to S. Xue et al. studied the deactivation of a Pt/ZrO_2 catalyst in WGS in the presence of 50 ppm H_2S at 300 ^oC and found initial deactivation, which, however, was fully reversible after H_2S removal from the feed stream [126]. In the following, Luo and Gorte studied deactivation of Pd/CeO_2 catalysts in WGS through ex-situ poisoning with SO_2 [127]. Combining steady-state, pulse-reactor, and FTIR studies, they found that SO_2 exposure reduced the rate of Pd/ceria to that of Pd/alumina, indicating that the S poisoning affected the support rather than the metal component. The observations were explained by the formation of cerium sulfates upon SO_2 exposure, which were reduced to oxysulfates in the WGS stream, but could not be re-oxidized by H_2O or CO_2. The deactivation was hence a result of blocking the support redox cycle. Most recently, Liu et al. revisited Pt/ceria catalysts for sour WGS in the presence of rather low levels (20 ppm) of H_2S [128]. They found that the catalysts performed stable after an initial deactivation phase, and that the degree of deactivation was reduced with increasing temperature (from 550–750 K) and increasing Pt content (from 0.38–2 wt% Pt). The pore structure of the catalyst was not significantly affected by S, but the metal particle sizes were not further characterized. Changes in CO chemisorption were tentatively attributed to changes in the concentration of surface hydroxyl groups, possibly due to formation of surface sulfates.

2.0 OBJECTIVES

One major target of current project is to obtain a novel highly active WGS catalyst without disadvantages of current industrial catalysts as discussed in section 1.2. In addition, through this investigation, we can obtain a better understanding of the function of oxide supports and the mechanism of WGS on metal/oxide(s) catalysts.

Due to the high activity at low temperature and interesting catalytic mechanism, Au/CeO_2 was selected as our starting point. Although the size effect and oxidation state of gold have been widely studied, the reducibility of oxide supports has been believed as a determining factor to the WGS activity, since the water dissociation, which is the rate-determining step, occurs on the oxide supports. In order to evaluate the effect of reducibility, the composition and morphology of CeO_2 and doped CeO_2 were tailored in this project. In chapter 3.0 , the composition effect of oxide supports to the WGS activity was investigated and discussed. However, due to the reported solubility limitation of La_2O_3 in CeO_2, we used a novel microemulsion method to prepare homogenously mixed oxides for WGS catalyst. As a result, the reducibility and WGS activity of Au supported catalysts is dramatically affected by the dopant concentration.

In addition, since the shape of nanostructured CeO_2 has a strong impact to the reducibility and the WGS activity, the combined effects of composition and morphology were investigated to optimize the our catalyst design (chapter 4.0). The results showed that although the nanorod shape CeO_2 exhibits higher reducibility and WGS activity than the nanoparticles, the doping of

lanthanum cannot further improve nanorod catalysts. However, the correlation between the reducibility of oxide supports and the WGS activity of Au-based catalysts was established.

After the highly active WGS catalyst was obtained, the stability and robustness issues were discussed in chapter 5.0 and 6.0 . Since the noble metals, especially Au and Pt, are well-known for their instability due to sintering and S-poisoning, the surface decoration techniques were applied to deposit a La_2O_3 layer on catalyst to protect the active metal nanoparticles. The La_2O_3 can stabilize the catalysts during cyclic WGS by regulating the mobility of Au nanoparticles. In addition, since the La_2O_3 has high S-capturing capacity, this protective layer can capture H_2S in sour WGS reaction, leading to a multifunctional periodic sulfur resistant catalyst.

Last but not least, although the sulfur poisoning and regeneration of Pt-based catalysts have been widely acknowledged, the mechanism of regeneration has not been clearly reported due to the simultaneous S-poisoning and regeneration in sour WGS. In chapter 6.0 , we were aiming at a better understanding of Pt-based catalysts' performance in sour WGS and regeneration, which can eventually help to design a sulfur resistant WGS catalyst. Pt/Al_2O_3 and Pt/CeO_2 with different morphologies (nanoparticles and nanorods) were characterized and tested in sour WGS. The reducible CeO_2 shows strong impact to the regeneration of sulfurized catalyst due to the strong metal support interaction (SMSI) between platinum and ceria.

3.0 COMPOSITIONAL TAILORING OF GOLD-BASED WGS CATALYSTS

Gold supported on metal oxides has been widely used in CO oxidation and, more recently, in WGS. Since the nature of the catalyst support exerts a decisive influence on the catalytic activity [84, 129], the impact of metal oxide supports has been investigated extensively in WGS [54, 130]. Among those, CeO_2 is one of the most effective (and active) supports for Au catalysts, although the role played by CeO_2 is still a matter of debate [131]. Previous studies showed that the active species are isolated $Au^{\delta+}$ cations [40], and that the redox property and oxygen storage capacity of CeO_2 are crucial for the activity of the Au/CeO_2 catalysts [40, 49, 132]. In particular, it has been reported that the addition of rare earth additives affects redox properties and oxygen vacancies in ceria [82, 133], which can strongly impact catalyst activity [134-136]. However, there is still significant disagreement in the literature and very few systematic studies of such doped-CeO_2 catalysts for WGS are available due to difficulties in synthesizing well-controlled homogeneous mixed oxides, especially in the high doping range.

The reported solubility limit for La_2O_3-CeO_2 mixed oxides prepared by various methods, including co-precipitation [137], solid state reaction [138], evaporation from solution [139], hydrothermal [140] and sol-gel synthesis [141], is typically below 40%-70%, and even in cases where the synthesis of mixed La_2O_3-CeO_2 is successful, phase separation at elevated temperatures is commonly reported [142, 143]. This poses a significant limitation both with

regard to technical application of such mixed oxides as well as to developing a deeper understanding of the impact of the oxide composition on material properties.

Here, we synthesize nanostructured La_2O_3-CeO_2 mixed oxides via a straightforward reverse microemulsion-templated approach, and the systematic investigation of the La:Ce-ratio on their reducibility. Reverse microemulsion-templated syntheses offer exceptional control over synthesis conditions [144, 145]. Confining the materials synthesis into the nanosized micelles not only allows regulation of particle size, and hence yields high surface area materials, but it also exerts control over the hydrolysis rate of different precursors for mixed oxides and hence allows for finely controlled synthesis of highly homogeneous mixed oxides with excellent thermal stability [8, 146].

3.1 EXPERIMENTAL SECTION

3.1.1 Materials and syntheses

Chemical reagents including lanthanum isopropoxide (Alfa-aesar, La 40%), cerium isopropoxide (Alfa-aesar, Ce 37-45%), poly(ethylene glycol)-*block*-poly(propylene glycol)-*block*-poly (ethylene glycol) (PEPP, Aldrich, MW=2000), isooctane (Aldrich, 99.8%), 1-pentanol (Aldrich, 99+%), anhydrous 2-propanol (Aldrich, 99.5%) were used as received without further purification. Pure lanthanum oxide (La_2O_3), cerium oxide (CeO_2), and mixed lanthanum cerium oxides ($La_xCe_{1-x}O_y$) were all synthesized by a reverse microemulsion method, as adapted previously in our laboratory.[6, 7] For example, to prepare $La_{0.5}Ce_{0.5}O_{1.75}$, 10.97 g de-ionized water, 38.57 g isooctane, 12.85 g PEPP and 150 g 1-pentanol were used to obtain a reverse

microemulsion. 0.5 g lanthanum isopropoxide and 0.59 g cerium isopropoxide were dissolved in 108 ml anhydrous 2-propanol by stirring, and refluxed at 95 ℃ for 2 h. The solution was then introduced to the microemulsion at room temperature. After ageing for 72 h, the water and oil phases were separated by temperature-induced phase separation (TIPS). The product phase was washed several times with acetone, and remaining volatile residues were removed via freeze drying. Finally, the dried powder was calcined at 450 ℃ or 750 ℃ for 2 h in air.

$Au/La_xCe_{1-x}O_y$ samples were prepared by deposition–precipitation (DP) [131]. $HAuCl_4$ (99.9+%, Aldrich) solution was added drop-wise at room temperature into an aqueous slurry of the oxide, keeping the pH of slurry fixed via addition of 0.2 M $(NH_4)_2CO_3$ (93.5+%, J.T.Baker). The resulting precipitate was aged at room temperature for 1 h, filtered, washed, dried at 100 ℃, and then calcined at 400 ℃ for 2 h. The nominal Au loading for all catalysts was 5 wt%.

3.1.2 Characterization

The specific surface area was determined via nitrogen sorption in a Micromeritics ASAP 2020 gas adsorption analyzer using the BET method. Prior to the measurement, the samples were degassed for 2 h at 200 ^oC under high vacuum. The compositions of mixed oxides were determined by Energy-dispersive x-ray analysis (EDX) equipped on Philips XL-30 field emission scanning electron microscope (SEM). The actual Au content of each sample was analyzed by inductively coupled plasma mass spectrometry (ICP-MS, Perkin Elmer Elan DRC II). The X-ray diffraction (XRD) measurements were performed with a high-resolution powder X-ray diffractometer (Phillips PW1830) in line focus mode employing Cu-Kα radiation (λ = 1.5406 Å). Crystal phases were identified based on JCPDS cards. Particle sizes were calculated from the Debye-Scherrer equation. Sample morphology was determined by transmission

electron microscopy (JEOL-2000FX). Temperature-programmed reduction by hydrogen (H_2-TPR) was conducted using a Micromeritics Chemisorb 2750 system equipped with a thermal conductivity detector. During the TPR analysis, the samples were first oxidized in 5% O_2/He at 450 ^oC for 2 h, and then TPR was performed by heating the sample (100 mg) at 5 ℃/min to 900 ℃ in a 10% H_2/Ar flow (30 ml/min). A cold trap filled with acetone-dry ice mixture was placed between reactor and TCD to remove the water vapor.

X-ray photoelectron spectroscopy (XPS) spectra for samples containing different La concentrations were recorded in a Theta Probe system (Thermo Scientific) using a 400 μm diameter monochromatic Al-K_α excitation at 1486.6 eV with a Hemispherical Analyzer operated in the constant pass energy mode at 50 eV. To analyze the individual contributions of the Ce 3d and La 3d core levels, peak decomposition was carried out by using mixed Gaussian-Lorentzian peaks with a Shirley-type background.

3.1.3 Catalyst tests

WGS tests were carried out in a 5 mm ID quartz glass tube heated inserted into a high-temperature tube furnace at ambient pressure. The catalyst powder (50 mg) was supported within the tube on either end by quartz glass felt plugs. Water was injected via a syringe pump (Braintree Scientific, Inc.) and vaporized in a heated line before entering the reactor. The composition of the mixture after water addition was 10.8% H_2O, 2.1% CO, and 87.1% He. The total flow rate of gas was typically around 100 CCM resulting in space velocities of ~150,000 h^{-1}. The exit gas passed through a condenser to eliminate H_2O from the stream and then was analyzed by an Agilent 3000A Micro GC equipped with thermal conductivity detector (TCD). In order to assure reaching steady state after adjusting operating conditions (such as temperature

steps), CO conversion was measured repeatedly until the conversion varied less than 1% over a duration 5 minutes. No methane was detected at any conditions used in this work. The inert helium feed is used as an internal standard, and is used to calculate the total gas flow rate after water condensation and to back-calculate the concentration of water leaving the reactor.

3.2 RESULTS AND DISCUSSION

3.2.1 Structure of $La_xCe_{1-x}O_y$

Using the above described experimental approach, pure lanthanum and cerium oxides were first synthesized as reference points for the following synthesis and characterization of the mixed oxides. In particular for La_2O_3 reports of successful syntheses of high surface area materials are limited to-date [147, 148]. It seemed hence of interest in itself to investigate whether a carefully controlled microemulsion-based synthesis could result in increased surface areas.

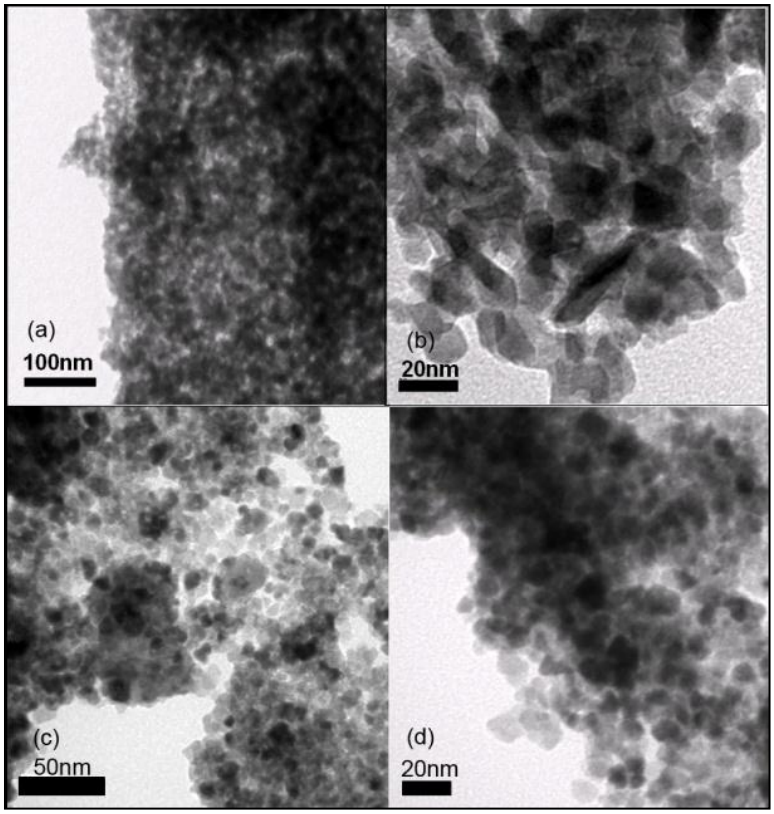

Figure 5. TEM image of crystallized La_2O_3 (a,b) and CeO_2 (c,d), after calcinations at 450 ^oC and 750 ^oC, respectively

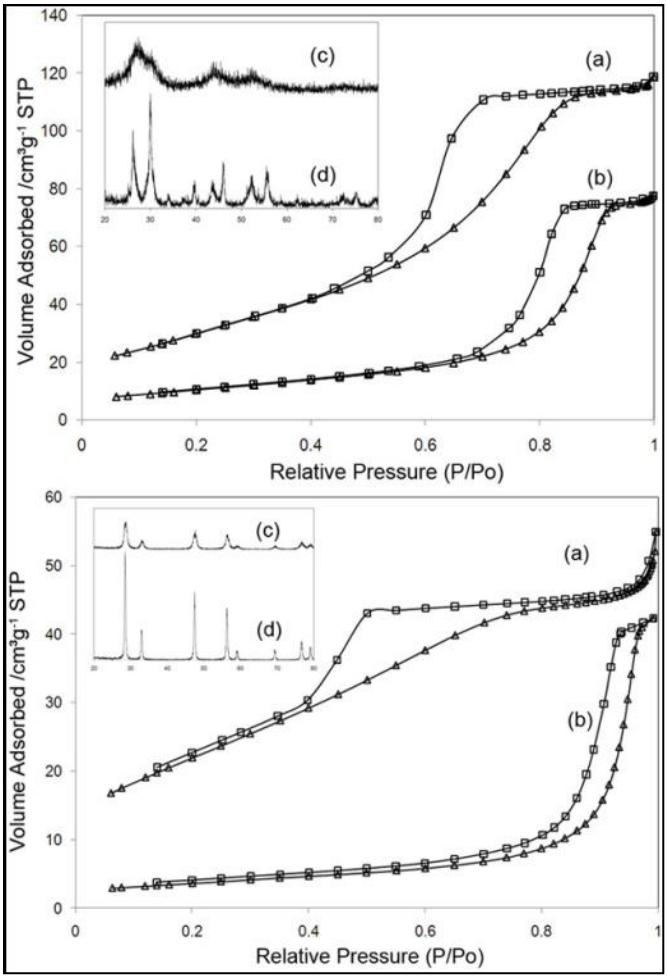

Figure 6. Nitrogen adsorption–desorption isotherms for La_2O_3 and CeO_2 after calcined at 450 ℃ (a) and 750 ℃ (b), and XRD diffractograms for La_2O_3 and CeO_2 after calcined at 450 ℃ (c) and 750 ℃ (d)

The morphology of pure La_2O_3 as synthesized in our microemulsion method is illustrated by the TEM images in Figure 5 (a and b). The images reveal a mesoporous structure of the oxide, created by the agglomeration of dense nanoparticles about 10-20 nm in size. The mesoporous character of the materials is confirmed by BET, as seen in the typical type IV isotherms with H2 hysteresis shown in Figure 6 (top, a and b). The surface area of the lanthana is close to 100 m^2/g after calcination at 450 ℃ (see Table 1), well in excess of previously reported surface areas of less than 30 m^2/g [149, 150]. XRD shows that the sample is largely amorphous after calcination

at 450 ℃ (Figure 6 top, c), in agreement with the known high crystallization temperature of La_2O_3 of ~700 ^oC [151-153].

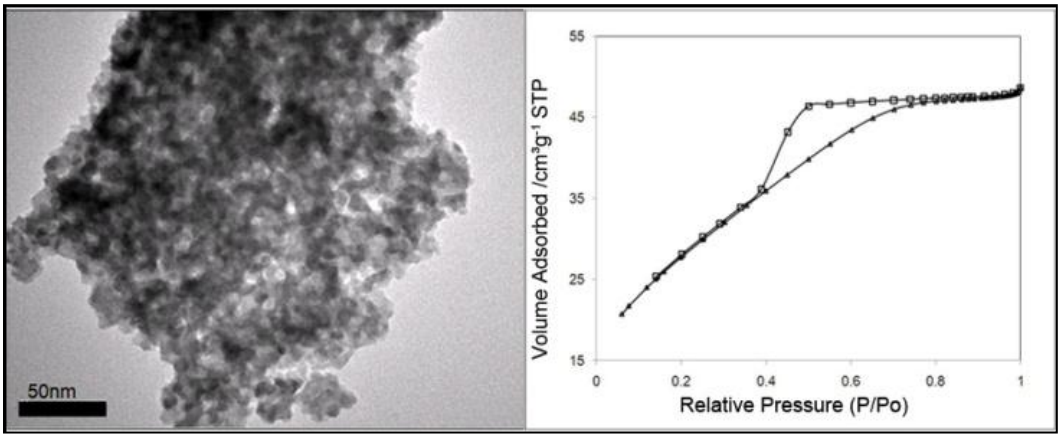

Figure 7. TEM image and Nitrogen adsorption–desorption isotherms for $La_{0.5}Ce_{0.5}O_{1.55}$ calcined at 450 ℃

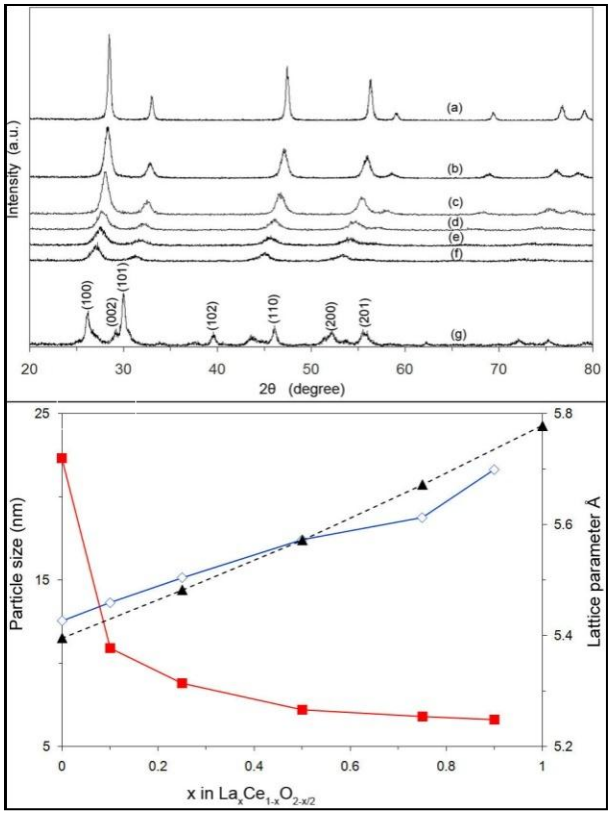

Figure 8. (A): XRD of pure and mixed $La_xCe_{1-x}O_y$ calcined at 750 ℃ with La content (a) =0%; (b) =0.1; (c) =0.2; (d) =0.25; (e) =0.5; (e) =0.75; (f) =0.9; (g) =1, (B): experimental lattice parameter (◇), calculated lattice parameter (▲), and particle size (■) of $La_xCe_{1-x}O_y$ with different La content after calcined at 750 ℃

Cerium oxide synthesized in the same way shows a similar morphology and structure (Figure 5 c and d, and Figure 6 bottom, a and b) and similarly high surface area of ~70 m^2/g (Table 1), which can be attributed to the small particle size templated by the micelles in the microemulsion. Unlike La_2O_3, however, CeO_2 is already highly crystalline after calcination at 450 ^oC, as confirmed by XRD (Figure 8). It is worthwhile to note that, compared to La_2O_3, the isotherm of CeO_2 calcined at 450 ^oC (Figure 6 bottom, a,) exhibits a different type H2 hysteresis loop with a linear adsorption isotherm, indicating a highly disordered mesoporous structure with a wide pore size distribution [154, 155]. After high-temperature calcination at 750 ^oC, the hysteresis loop changes to a type H1 hysteresis (Figure 6 bottom, b,) attributed to agglomerates of spheres with roughly uniform size, resulting in narrow pore size distributions [154].

Table 1. Surface area and particle size of La_2O_3 and CeO_2

	450 ℃		750 ℃	
	Surface area (m^2/g)	Particle Size (nm)	Surface area (m^2/g)	Particle Size (nm)
La_2O_3	95.5	N.A.*	26.5	45.9
CeO_2	69.5	10.3	12.8	22.3

* La_2O_3 calcined at 450 ℃ is amorphous and no particle size data can be acquired from XRD. TEM images in Fig. 1 allow estimate of particle size in the range of 10-20 nm.

This change in structure upon high-temperature calcination also results in a strong decrease in surface area. As shown in Table 1, both pure oxides lose more than 70% of their surface area after calcination at 750 ^oC due to rapid growth of the primary oxide particles. This strong sintering is not surprising for lanthana, which undergoes crystallization, resulting in large mass transport and hence restructuring of the material. However, a similarly large loss in surface area for ceria is less expected. It can most likely be attributed to the removal of residual surfactant that was capping the nanoparticles at lower temperature and is being burnt off in the temperature range between 450 and 500 ^oC [6]. These cappings help to stabilize the materials at lower temperature by forming a diffusion barrier around individual nanoparticles, essentially

"freezing" the materials in their disordered morphology resulting from the synthesis. After this barrier is burnt off at higher calcination temperatures, the particles start to sinter and rapid particle growth occurs (as confirmed by Debye-Scherrer analysis, see Table 1). This can also explain the transition in the nitrogen sorption hysteresis for ceria from an H2 to H1 hysteresis. However, despite this strong loss in surface area upon calcinations at 750 ^{o}C, the surface area of both pure oxides compares favorably with previous reports in the literature [30, 36].

Based on the same microemulsion-templated synthesis used for the pure oxides, mixed La/Ce-oxides were synthesized by using carefully adjusted mixtures of the respective precursors. The actual lanthanum and cerium content was determined via energy-dispersive x-ray analysis (EDX) and was found to be in close agreement with the nominal values from the synthesis (Table 2). For simplicity, we therefore use the nominal fractional La content 'x' to refer to the samples with different lanthanum content throughout the present report.

Table 2. Composition of mixed La/Ce-oxides

La nominal fraction 'x'	La actual at. % (from EDX)	Ce actual at. % (from EDX)
0.1	11.08	88.92
0.25	26.33	73.67
0.5	50.78	49.22
0.75	74.68	25.32
0.9	85.03	14.97

Figure 7 shows the TEM image along with the type IV isotherm with type H2 hysteresis loop for a mixed oxide with La:Ce = 1:1 after calcination at 450 ^{o}C. As expected, the mixed oxide shows no obvious difference in morphology and structure from either pure oxide.

Figure 8 (A) shows the XRD diffractograms for pure and mixed $La_xCe_{1-x}O_y$ with increasing La content from 0% (i.e. pure ceria, Figure 8 (A) (a)) to 100% (i.e. pure lanthana, Figure 8 (A) (g)) after calcinations at 750 ^{o}C. The pure oxides show cubic and hexagonal crystalline structures for ceria and lanthana, respectively, in agreement with the standard XRD

patterns of CeO_2 (*JCPDS* 34-0394) and La_2O_3 (*JCPDS* 05-0602). Surprisingly, however, all mixed oxides display only the (shifted) fluorite pattern of ceria (Figure 8 (A) (b)-(f)), even for La loadings as high as 90%. No second phases or additional reflections can be found for any mixed oxide, indicating the formation of a single, homogeneous mixed-oxide phase. With increasing La content, however, one observes an increasing shift in the diffraction pattern, corresponding to a continuous change in the lattice parameter, as well as a broadening of the $La_xCe_{1-x}O_y$ reflections, indicating a decrease in particle size.

These trends are quantified in Figure 8 (B), which shows the change of lattice constant and particle diameter as function of La content as calculated from the XRD patterns. One can see a continuous decrease in particle diameter with increasing La content, from ~22 nm for pure ceria to ~7 nm for 90% La content. This indicates that the addition of lanthanum suppresses the crystal growth of ceria, as previously observed by Wang *et al.* [156]

It should be noted here that both particle size and lattice strain can contribute to peak broadening in XRD, in particular for nanoparticles. Such lattice strain effects are accounted for by using a modified Scherrer equation (Eq. (5)) [157, 158]:

$$\beta\cos\theta = 0.89\lambda/D + \eta\sin\theta \qquad (5)$$

in which β is full-width at half-maximum of the XRD peak, $\lambda = 1.5406$ Å is the incident x-ray wavelength, θ is the diffraction angle, and D is the crystallite size. The latter can then be calculated by a linear fitting of $\beta\cos\theta$ versus $\sin\theta$. For our data, however, we found no dependence of $\beta\cos\theta$ on $\sin\theta$, with data scattering around a fixed value of $\beta\cos\theta$. We take this to indicate the absence of significant lattice strain in our samples, likely due to the high-temperature calcination at 750 ^{o}C. Therefore, average particle sizes were calculated directly from the simplified Debye Scherrer equation, i.e.: $D = 0.89\lambda/(\beta\cos\theta)$.

Figure 8 (B) furthermore shows that the lattice constant changes linearly from 5.41 Å for pure ceria to 5.70 Å for 90% La content, i.e. an overall increase of more than 5%. This linear increase in lattice constant is in agreement with previous calculations by Morris *et al*. [142] However, this is the first time that a verification of these calculations up to high La content is possible, since previous attempts using various different synthesis strategies failed to do so due to phase separation of a pure La_2O_3 phase at high La contents [137-142]. This highlights the exceptionally well-controlled nature of the reported microemulsion-templated synthesis, which allows formation of mixed oxides across the entire range of La:Ce ratios.

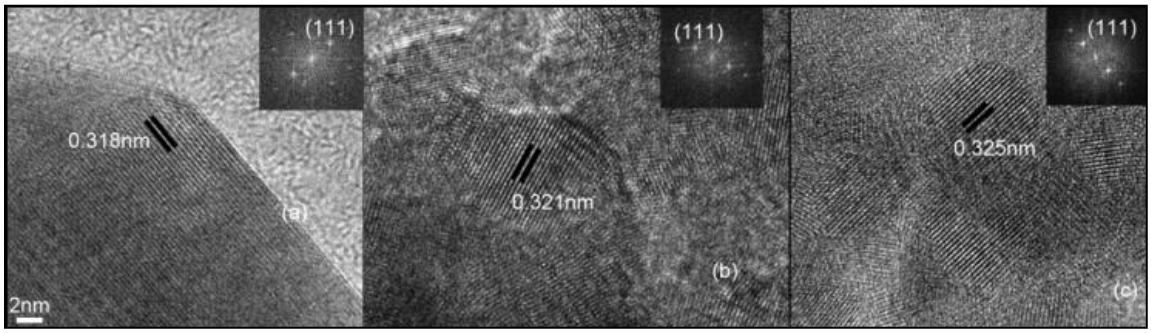

Figure 9. HR-TEM images of $La_xCe_{1-x}O_y$ with x = 0.5 (a); = 0.75 (b); = 0.9 (c). (Insets show the fast fourier transformation (FFT) patterns of the respective HR-TEM image)

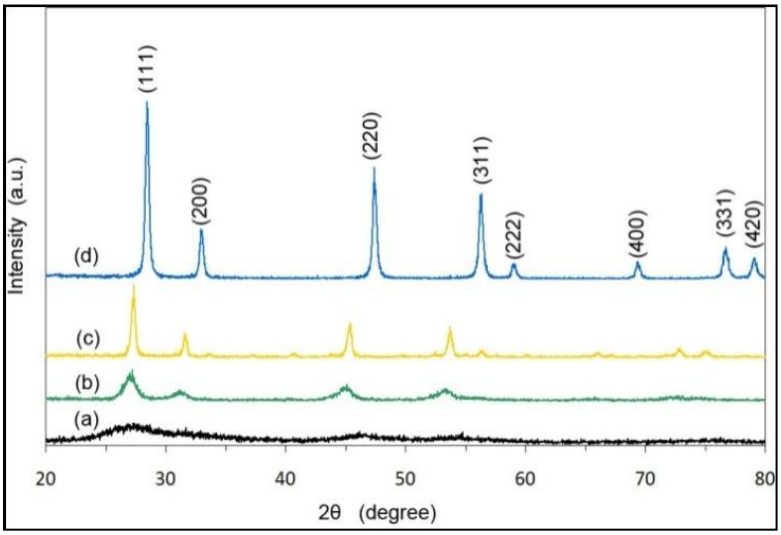

Figure 10. XRD of $La_{0.9}Ce_{0.1}O_{1.55}$ (a) calcined at 450 ℃; (b) 750 ℃; (c) 1050 ℃; (d) CeO_2 calcined at 750 ℃

The lattice expansion is further confirmed by HR-TEM (Figure 9). Fast Fourier transformation (FFT) analysis of the HR-TEM image was used to identify the (111) plane and measure the lattice parameter of the oxide particles. It shows the expansion of the (111) d-spacing for high La-content mixed oxides from 0.318 nm for 50% La to 0.325 nm for 90% La content. For comparison, the value for CeO_2 (*JCPDS* 34-0394) is 0.311 nm (a comparison to La_2O_3 is not possible due to the different crystal structure). This lattice expansion can be attributed to a combination of the effects of increasing number of oxygen vacancies due to La doping and the larger ionic radius of La^{3+} vs Ce^{4+}[142, 159]. The HR-TEM images thus confirm the highly homogeneous, crystalline structure of these mixed oxides.

In order to further probe the phase stability of the high La-content mixed oxides, the samples were calcined at increasingly high temperature and characterized by XRD. Fig. 6 shows the development of the XRD pattern for $La_{0.9}Ce_{0.1}O_{1.55}$ (i.e. 90% La) as a function of calcination temperature ((a) – (c)) in comparison to a pure ceria sample (d). One can see that the sample calcined at 450 ℃ shows only broad, weakly defined peaks at 28 °, 47 ° and 53 °, which indicates the presence of very small crystallites. With increasing calcination temperature, these peaks get increasingly sharper and well-defined, indicating particle growth as seen before for the pure oxides. However, all diffractograms are in perfect agreement with a shifted fluorite pattern for pure ceria Figure 10, d). Most significantly, no additional reflections, which would suggest the formation of a separate La_2O_3 phase, are observed even after calcination at temperatures as high as 1,050 ^{o}C. These results hence further confirm the formation of highly homogeneous mixed oxides, resulting in exceptional phase stability even at such extreme conditions. To our knowledge, this is the first report of such highly stable mixed oxides over a broad range of La contents as high as 90%.

The exceptional homogeneity and stability of the mixed oxide phase can be attributed to the controlled synthesis. Unlike co-precipitation or non-templated sol-gel methods, the rate of microemulsion-templated syntheses is determined by the diffusion of the precursors from the oil phase into the aqueous phase rather than by precipitation or hydrolysis which tend to be very rapid and hence poorly controlled. [146] The similar diffusivity of the two alkoxide precursors in the oil phase results in similar (effective) reaction rates and hence in well-ordered materials in which the composition on the atomic scale reflects the well-mixed composition of the precursor solution.

However, at this point, we do not have a clear explanation why the mixed oxide phases favor the fluorite crystal structure even for La contents as high as 90%. One possible explanation could be that the amorphous mixed oxide starts crystallizing in the fluorite-type structure during calcination at low temperatures, since the crystallization temperature of ceria (<450 ^{o}C) is much lower than that of lanthana (~700 ^{o}C), and, once formed, the above discussed homogeneity of the materials results in stabilization this structure. This is supported by the development of the XRD patterns during the crystal growth process of the mixed oxide (see Figure 10). However, more work is required to fully elucidate this point, and particularly computational materials modeling of these mixed oxides could shed further light on this surprising observation.

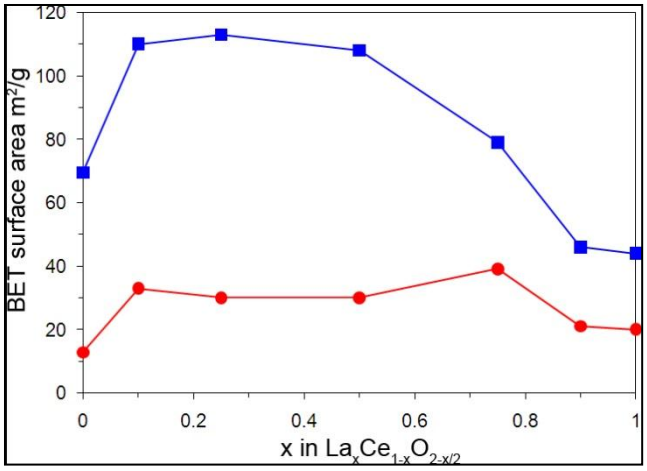

Figure 11. BET surface area of $La_xCe_{1-x}O_y$ with different lanthanum content, aged at 450 ℃ (■) or 750 ℃ (●)

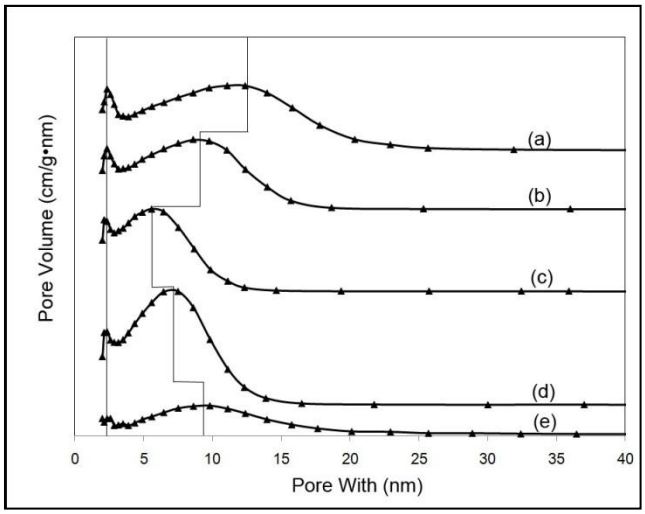

Figure 12. BJH pore size distributions obtained from the adsorption branches of the isotherms of $La_xCe_{1-x}O_y$ with varying La content after calcinations at 750 ℃ for 2 h in air: (a) =0.1; (b) =0.25; (c) =0.5; (d) =0.75; (e) =0.9

In addition to crystal structure, the surface area of the mixed oxides is also affected by the La content. Figure 11 shows the BET surface area of pure and mixed $La_xCe_{1-x}O_y$ oxides vs lanthanum content after calcinations at 450 ^oC and 750 ^oC. At both temperatures, the mixed oxides have significantly higher surface areas than either pure oxide. For example, after calcination at 450 ℃ the surface area of $La_{0.25}Ce_{0.75}O_{1.875}$ is 113 m^2/g, i.e. approximately twice the surface area of pure La_2O_3 or pure CeO_2. Furthermore, as expected from the results for the pure oxides, the surface area for all samples drops sharply after calcination at 750 ^oC for 2 h. For

example, the specific surface area of mixed oxides with a La content between 10% and 50% drops from ~110 m^2/g at 450 ^oC to ~30 m^2/g at 750 ^oC, i.e. the materials lose over 70% of their surface area. This is consistent with the results for the pure oxides and suggests again that the loss of the residual surfactant capping in this temperature range results in particle growth. However, the mixed oxides still remains roughly twice the surface area of either of the pure oxides. Finally, it is interesting to note that even relatively small La additions to ceria (see 10% La in Figure 11) result in a drastic increase in surface area, while the addition of small amounts of Ce to lanthana (90% La) has comparatively little impact on the surface area. Clearly, La plays a much more important role in stabilizing high surface areas than Ce.

Beyond surface area, the porosity has a decisive impact on the performance of materials in applications such as sorption, sensing, and catalysis. The pore size distributions of the mixed oxides were hence determined from nitrogen adsorption isotherms using the BJH method. It is worth noticing that the desorption branches of the isotherms of the mixed oxides show a lower closure point at p/p^0 = 0.4~0.45, in which case the pore size distribution obtained from the adsorption branch of the isotherm is considered more reliable and was hence used here.[154, 155] Figure 12 shows the results for mixed oxide samples with (a) 10%, (b) 25%, (c) 50%, (d) 75%, and (e) 90% La content. One can see an interesting development of a bimodal pore size distribution as function of La content: The 10% La sample (Fig, 10 (a)) shows a bimodal distribution with a weak peak at 2.3 nm ("peak I"), and a more pronounced, broader peak at 12 nm ("peak II"). Peak I maintains its position at 2.3 nm for all samples. However, upon increasing the La content to 25% and 50%, peak II shifts continuously towards lower pore diameters and sharpens noticeably, while at La loadings above 50%, it broadens again and shifts back towards larger pore diameters.

This observation seems to suggest that mixed $La_xCe_{1-x}O_y$ oxides contain two types of pores, both in the mesopore range. One type of pores has a diameter of 2.3 nm and appears unaffected by the La:Ce ratio, while the diameter of the second type of pores and its relative contribution to the total pore volume is strongly determined by the La content. Furthermore, the second type of pores dominates the pattern when the lanthana content is adjusted to either direction away from 50%. While it is tempting to interpret the occurrence of these two types of pores due to the formation of two different oxide phases, this is clearly contradicted by our results from XRD and TEM investigations, as described above. At this point, we do not have a consistent explanation of this phenomenon. Further investigations appear worthwhile, however, as this suggests a simple way to tailor the pore size for these mixed oxides without a strong impact on surface area (see Figure 11).

3.2.2 Effect of La content on the reducibility of oxide supports

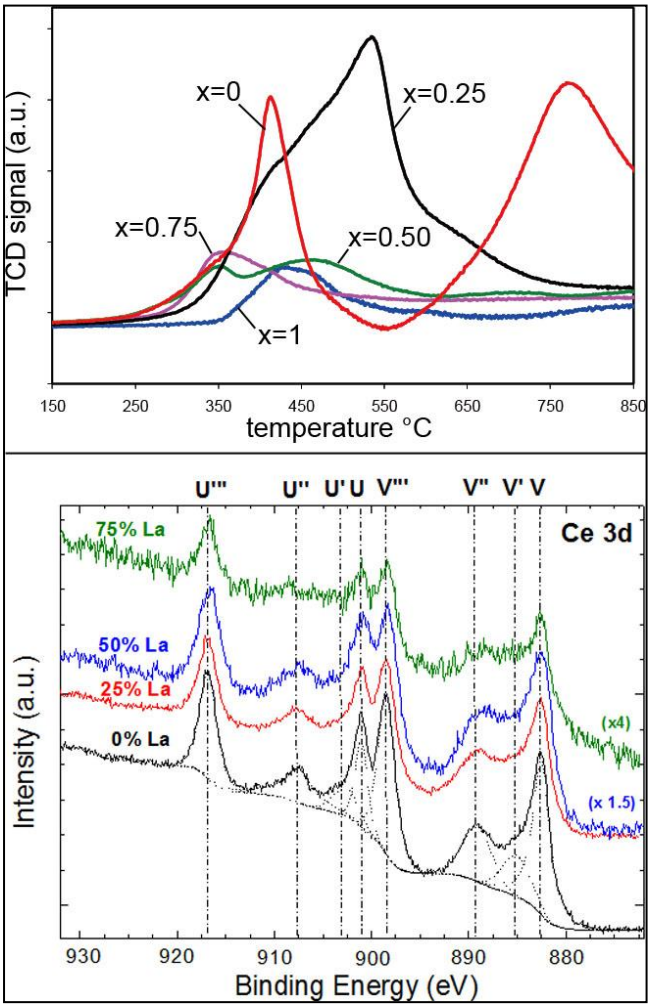

Figure 13. (A) H_2-TPR profiles of $La_xCe_{1-x}O_y$ with different lanthanum content (x), (B) the Ce 3d spectra for samples with different amounts of La content. Solid lines represent the experimental spectra and the dotted lines in the CeO_2 sample are the Shirley background and the results from peak fitting

Finally, the reducibility of the mixed oxides was investigated via H_2 temperature programmed reduction. Reducibility and oxygen storage capacity are key functional properties of oxide materials, particularly for ceria which is widely used as oxygen storage and "transfer" agent in catalysis and related applications.[160-162] As discussed before, it can be expected that the

reducibility of these mixed oxide samples is strongly affected by the La content due to the introduction of oxygen vacancies.

The TPR patterns are shown in Figure 13 (A), and Table 3 summarizes the respective peak positions, peak areas and H_2 consumptions for all samples after calcination at 750 ^{o}C. Pure ceria shows a low-temperature reduction peak at 420 ℃, which can be attributed to the reduction of surface oxygen, and a high temperature reduction peak above 700 ℃, which is due to the (less facile) bulk reduction. In contrast, the mixed oxide with 25% La content shows only one, broad, strongly enhanced reduction peak, indicating a strong increase in the number of available oxygen species and more easily accessible bulk oxygen. This is in good agreement with the expected effect of La addition, as discussed above. As the La content increases further, the reduction peak shifts towards lower temperature, indicating increasingly facile reduction of the sample. However, the H_2 consumption of the samples with 50% and 75% La content decreases dramatically (see Table 3), indicating a strong decrease in the number of reducible sites.

Table 3. Reduction temperature and hydrogen consumption

	peak position (℃)	peak area (a.u.)	H_2 consumption (μmol/g)
CeO_2	420	5.12	395.5
$La_{0.25}Ce_{0.75}O_{1.875}$	500	13.36	1022.0
$La_{0.5}Ce_{0.5}O_{1.55}$	350	1.71	135.6
$La_{0.75}Ce_{0.25}O_{1.625}$	350	1.70	135.5
La_2O_3	430	1.08	88.2

The impact of La on the reducibility of ceria was further investigated by X-ray photoelectron spectroscopy (XPS). Figure 13 (B) shows the Ce 3d spectra for four different oxide compositions (0%, 25%, 50%, and 75% La). There are 8 peak assignments in the spectra, which are labeled according to the convention established by Burroughs [163]. The peaks U, U'', U''' and V, V'', V''' refer to $3d_{3/2}$ and $3d_{5/2}$, respectively, and are characteristic of Ce^{4+} 3d states. The peaks U', V' refer to $3d_{3/2}$ and $3d_{5/2}$ respectively, and are characteristic of Ce^{3+} 3d

final [163]. The fitted peak contributions and background are indicated by dotted lines for the pure CeO_2 sample. The doublets V^0 and U^0, corresponding to the Ce^{3+} $3d^9$ $4f^1$ O $2p^6$ final state, typically located at 880.6 and 898.9 eV, do not appear in our samples, indicating that Ce is mostly present in the Ce^{4+} oxidation state [164].

The ratio between Ce^{4+} and Ce^{3+} was calculated from the contributions in the XPS spectra, based on the above described peak assignments and the following equations (Eq. (6) and (7)):

$$Ce^{4+} = (U + U'' + U''' + V + V'' + V''')/[\sum_{n'} (U^{n'} + V^{n'})] \quad (6)$$

$$Ce^{3+} = (U' + V')/[\sum_{n'} (U^{n'} + V^{n'})] \quad (7)$$

where n' is for all states [164]. Using this method, the fitted peak areas in the XPS spectra were used to estimate the contributions of Ce^{4+} and Ce^{3+} as well as sample composition (Table 4). The values obtained for sample composition are in reasonable agreement with the nominally expected values as well as values determined from EDX (cp. Table 2). The difference between the compositions as determined from XPS and the nominal compositions indicates that the surface of the mixed oxide particles are slightly enriched in lanthanum, in particular for low La contents [137].

Table 4. Atomic composition of samples and their Ce^{4+}/ Ce^{3+} ratio

La % (nominal)	Ce^{4+}/ Ce^{3+}	Composition by XPS	
		Ce at. %	La at. %
0	4.97	24.55	0.00
25	6.47	17.82	9.15
50	7.22	13.93	18.02
75	13.67	4.25	17.13

More importantly, one can see that the data shows a strong increase in Ce^{4+}/Ce^{3+} ratio with increasing La content, from 4.97 for pure CeO_2 to 13.67 at 75% La. This suggests that La^{3+} is substituting Ce^{3+} ions in the ceria lattice, hence resulting in an increase of the Ce^{4+}/Ce^{3+} ratio.

However, since the La amount in all samples exceeds the amount of reduced Ce^{3+} present in the undoped CeO_2 samples (which is ~17%, vs 25% La at the lowest La dopings, see Table 4), the La doping results in the formation of additional defects in the oxygen sublattice along with an increasing shift towards Ce^{4+} in the Ce content of the samples.

Based on these XPS observations, the TPR results can be understood based on two counter-acting trends with increasing La content: On one hand, the introduction of La increases the defect density in the oxygen sublattice, increasing oxygen mobility and hence the low-temperature reducibility of the mixed oxide. This is also in agreement with previous computational studies by Balducci et al., which show that ceria dopings can lower reduction energies and activation energies of oxygen migration [85, 88]. On the other hand, the increasing La content causes a decrease in the absolute number of reducible Ce^{4+} sites, which results in a decrease in hydrogen consumption in TPR. The interplay between these counter-acting phenomena results in a maximum in the H_2 consumption, reflecting an optimal composition for oxidation-reduction reactions, and hence indicates that a carefully controlled synthesis of mixed La/Ce oxides can result in promising materials for application in catalysis and related reactive applications.

3.2.1 Effect of La content on the structure of Au-based catalysts

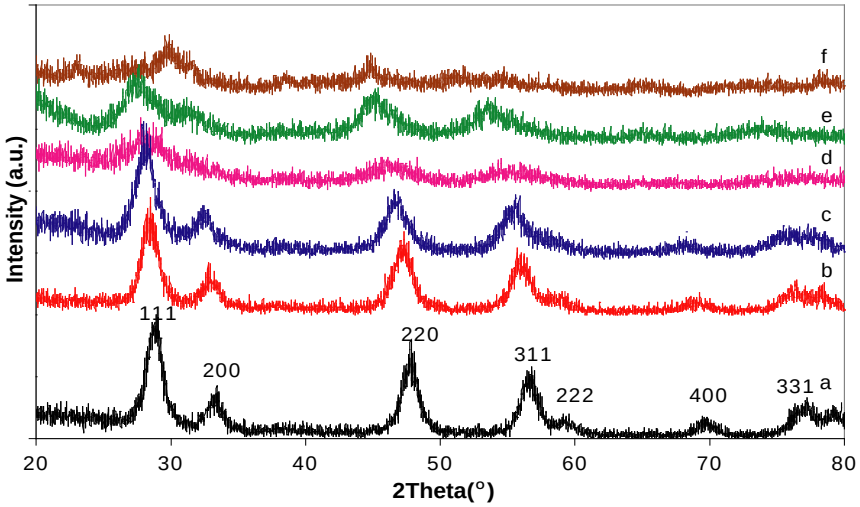

Figure 14. XRD patterns of select $Au/La_xCe_{1-x}O_y$ samples with varying La content (a: x=0, b: x=0.10, c: x=0.25, d: x=0.5, e=0.75, f: x=1)

In order to evaluate the effect of La content on the catalyst samples, the catalysts were first characterized via XRD (Figure 14). The diffractograms for all samples show the six dominant reflections of the cubic fluorite-structure of ceria, corresponding to the (111), (200), (220), (311), (222), and (400) planes of the *fcc* structure. In agreement with our previous study of mixed La/Ce-oxides, no reflections characteristic of La_2O_3 were observed, even at a La content as high as 75%. Only the pure La_2O_3 sample shows the expected *hcp* reflections (Figure 14, top curve "f"). This confirms the absence of any phase separation in these samples, i.e. the formation of a single, highly homogeneous mixed oxide phase.

Finally, no obvious Au peaks were detected, indicating that the Au particles are too small to be detected by XRD in all samples (< 3 nm).

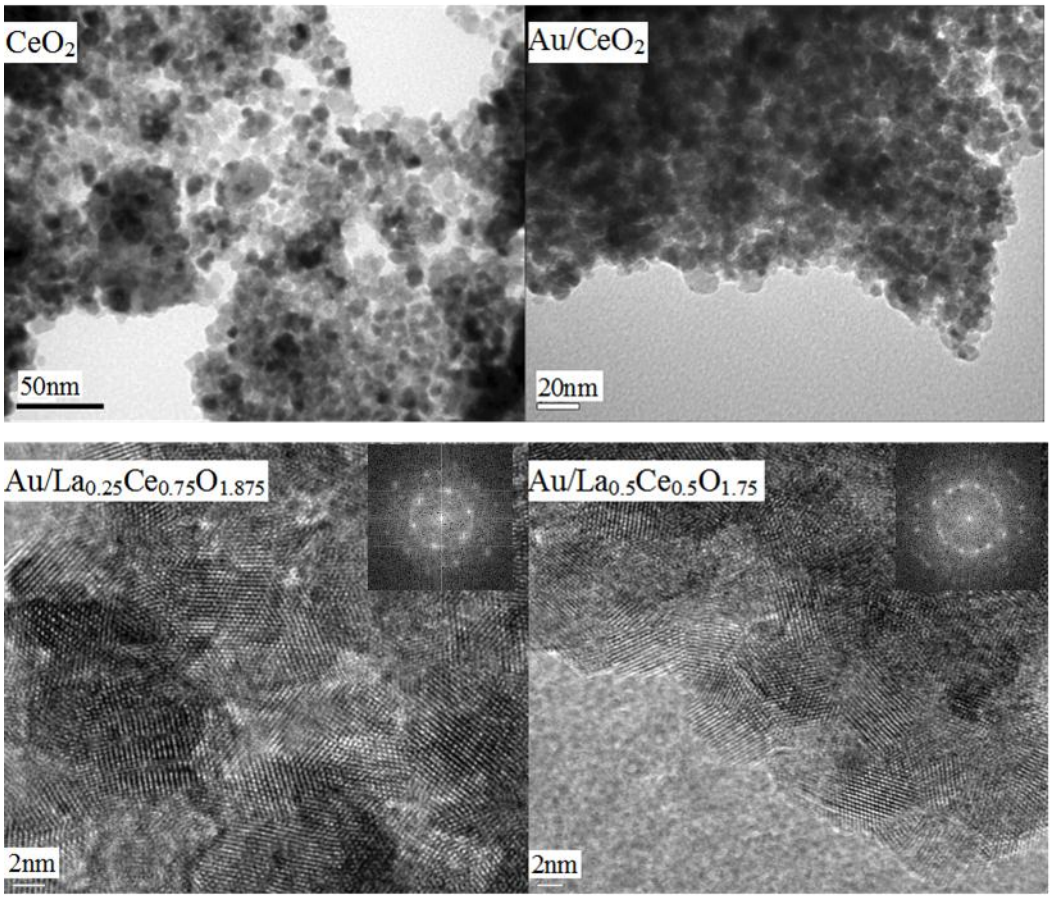

Figure 15. TEM images of CeO_2, Au/CeO_2 (top row), and HR-TEM images of $Au/La_{0.25}Ce_{0.75}O_{1.875}$ and $Au/La_{0.5}Ce_{0.5}O_{1.75}$ (bottom row).

Figure 15 shows the TEM images of pure CeO_2 (top left), Au/CeO_2 (top right), and two representative HRTEM images of $Au/La_xCe_{1-x}O_y$ mixed oxide catalysts (bottom left: x=0.25; bottom right: x=0.5). All samples consist of loosely agglomerated, roughly spherical nanoparticles. The addition of Au has no obvious effect on the morphology and the particle size of the supports. However, a slight decrease in particle size was found after La doping, from mean particle diameters of 7.6 nm for CeO_2 to 5.5 nm for $La_{0.5}Ce_{0.5}O_{1.75}$. This agrees qualitatively with previous results during Zr-doping of CeO_2 [165]. As mentioned before, the Au particles cannot be distinguished in the TEM micrographs since the oxides and Au nanoparticles have similar contrast.

For the Au/$La_xCe_{1-x}O_y$ mixed oxide catalysts, very uniform lattice fringes are observed in the HR-TEM images, indicating high crystallinity of the samples. Analysis of the lattice fringes reveals a cubic structure with mainly (111) surface exposed, in agreement with our XRD analysis. Pure La_2O_3 crystallizes at temperatures above 640 ℃ [152, 166]. However, all these catalysts were synthesized at room temperature and the supporting oxides were pre-calcined at 450 ℃. Clearly, the incorporation of La into CeO_2 did not result in high crystallization temperatures, even for very high La contents.

Table 5. Physical properties of $La_xCe_{1-x}O_y$ catalysts with and without Au

Sample	Surface area(m^2/g)		Pore volume(cm^3/g)		Particle size(nm)
	Support	With Au	Support	With Au	Support
CeO_2	103.7	87.3	0.10	0.10	7.6
$La_{0.1}Ce_{0.9}O_{1.95}$	112.7	99.3	0.15	0.14	n.d.
$La_{0.25}Ce_{0.75}O_{1.875}$	120.4	116.5	0.18	0.16	5.8
$La_{0.5}Ce_{0.5}O_{1.75}$	115.7	82.1	0.18	0.14	5.1
$La_{0.75}Ce_{0.25}O_{1.625}$	72.7	53.4	0.20	0.16	4.6
La_2O_3	52.9	24.0	0.18	0.11	8.5

BET surface area and pore volume of select samples as determined via BET and BJH analysis of nitrogen sorption, respectively, are shown in Table 5. One can see that addition of La initially results in an increase in total surface area, up to a maximum value of ~120 m^2/g for $La_{0.25}Ce_{0.75}O_{1.875}$, and a decreasing surface area for higher La contents. The pore volume follows similar trends, although the maximum is not as pronounced and appears slightly shifted towards higher La loadings.

Upon deposition of Au, the trends in surface area and pore volume remain unchanged, although absolute values for both decrease slightly by about 10%. This suggests that the Au nanoparticles are well dispersed on the supports and may result in some pore blockage.

3.2.2 Effect of La content on reducibility of Au-based catalysts

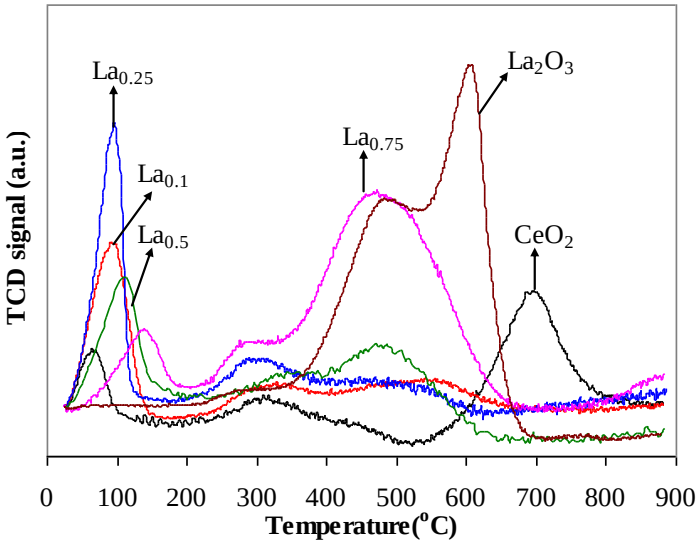

Figure 16. H_2-TPR of select Au/$La_xCe_{1-x}O_y$ samples.

As discussed in 3.2.2, the reducibility of $La_xO_{1-x}O_y$ is strongly affected by the La content. Here, for the Au/ $La_xO_{1-x}O_y$, the reducibility of these samples is strongly affected by Au deposition, as shown in Figure 16. The reduction temperatures for the surface oxide are lowered in comparison to the Au-free samples in Figure 13. For samples with less than 50% La, the surface reduction peak is shifted about 100 ℃ towards lower temperature, while it is shifted only 30~40 ℃ for those with higher La content. The reason for this might be that samples with lower La content have more surface oxygen, which is much more directly affected by the deposition of Au on the surface. Such a promotion of the surface reducibility in the presence of a noble metal has been reported before [131], and has been ascribed to a weakening of the surface oxygen bond in the presence of the noble metal, thereby improving the reducibility of the catalyst [167].

The high-temperature bulk reduction process, on the other hand, is controlled by the slow diffusion of the oxygen vacancies created at the oxide surface into the bulk. Therefore, Au deposition has only a very minor effect on the bulk reduction temperature.

Most significantly, however, a new reduction peak appears in the TPR profile of $Au/La_xCe_{1-x}O_y$ at much lower temperature than the surface reduction temperature. This peak is generally explained by the reduction of oxygen species on Au nanoparticles [77, 167-170] or the hydrogen spill-over from the metal to the support [171, 172]. Since the surface reduction peak area is strongly reduced upon Au-deposition (cf. Figure 16 and Figure 13), this indicates that much of the surface oxygen has already been reduced at the new low-temperature peak. It seems therefore more likely that hydrogen adsorption and dissociation on the Au nanoparticles, followed by H spill-over onto the oxide support, is responsible for the observed peak.

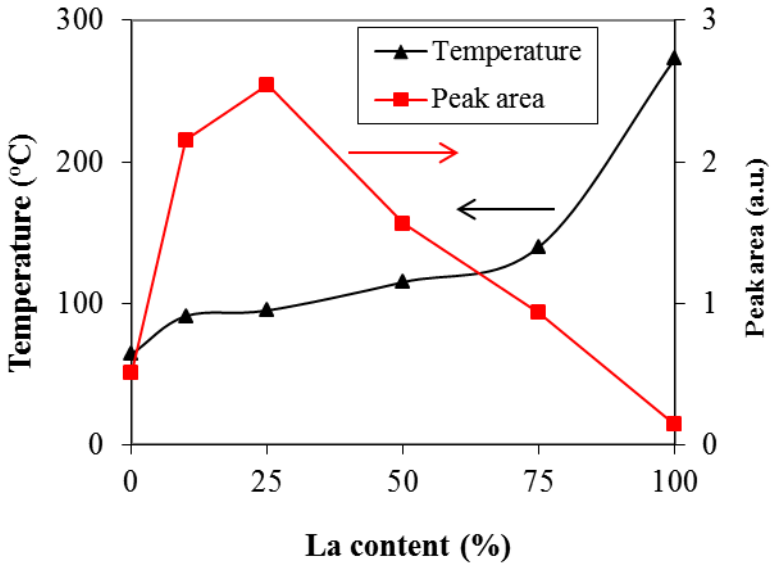

Figure 17. Temperature and peak area of reduction peak (< 200 ℃) vs. La content of select $Au/La_xCe_{1-x}O_y$ samples.

Figure 17 shows that this low-temperature reduction peak shifts continuously to higher temperature with increasing La content, while the peak area shows again the same trend as

observed in the absence of Au, i.e. it first increases to a maximum at ~25% La and then decreases strongly with further increase in La content.

Overall, we hence observe an improvement in the reducibility of the oxides upon La addition which can be ascribed to the formation of oxygen vacancies. These vacancies are known to play a key role in many oxidation reactions catalyzed by metal oxide catalysts via Mars-van Krevelen and related mechanisms [43, 136, 173-175]. The oxygen vacancies are formed upon La^{3+} insertion into the CeO_2 lattice due to different valences of the metals, and favor the mobility of lattice oxygen, resulting in lower reduction temperatures. However, on the other hand, more La^{3+} also causes the decrease of available lattice oxygen since oxygen is much more strongly bound to La than to Ce, resulting in a maximum in oxygen availability at moderate La loadings.

Addition of Au nanoparticles results in the increased surface reducibility due to La addition being superseded by a new low-temperature reduction facilitated by the presence of Au. However, the total availability of low-temperature reducible oxygen is still controlled by the amount of La addition, and one can hence expect that a moderate amount of La doping should result in the most active WGS catalyst.

3.2.3 Effect of La content on WGS activity

The effect of La doping on catalytic activity of $Au/La_xCe_{1-x}O_y$ in WGS was tested in fixed-bed reactor studies (see 3.1.3 for experimental details). Figure 18 summarizes the results for selected $Au/La_xCe_{1-x}O_y$ samples, ranging from pure CeO_2 to pure La_2O_3 supports, in terms of CO conversion as function of temperature.

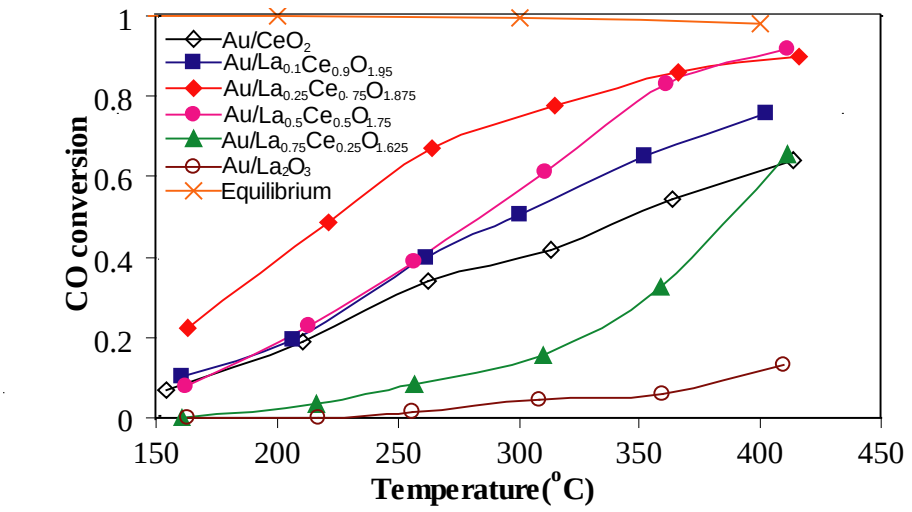

Figure 18. Catalytic activity of $Au/La_xCe_{1-x}O_y$ catalysts in WGS. CO conversion is shown as function of reaction temperature

As expected, Au/CeO_2 shows much higher activity than Au/La_2O_3, which can be ascribed to the reducibility of the supporting oxides. As shown above, CeO_2 is reducible in this temperature range, but La_2O_3 is non-reducible, and the importance of the reducibility of the support for WGS is well-established [170]. For the mixed oxides, the activity of the catalysts initially increases with La doping up to ~25% La, and then decreases again with further La addition. This trend can be more clearly seen in Figure 19, where CO conversion is shown as a function of La content for one fixed reaction temperature. Comparing the curve in Figure 19 to the reducibility trend in Figure 13, one can clearly see that both closely follow the same trends with La content, suggesting that it is indeed the reducibility of the oxide that has a determining effect on the activity of the catalysts.

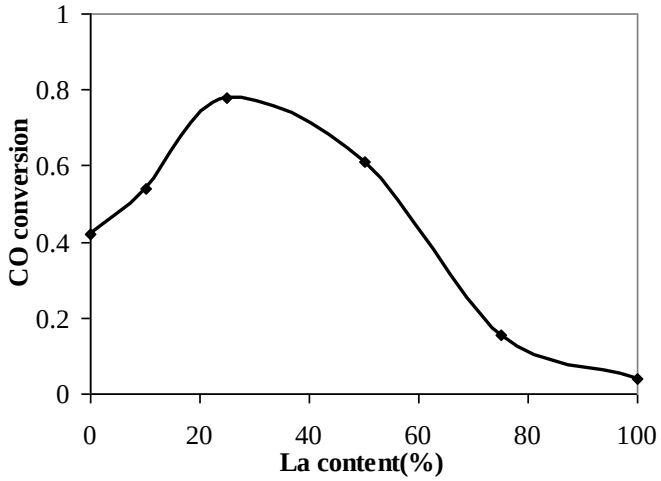

Figure 19. Catalytic activity of $Au/La_xCe_{1-x}O_y$ catalysts in WGS at 310 ℃

It should be mentioned that the oxidation state of Au is known to have a significant impact on the activity of Au in WGS [40]. From the present study it cannot be excluded that addition of La affects the catalytic activity by altering the oxidation state of Au at working conditions, although the direct comparison between the $Au/La_xCe_{1-x}O_y$ samples and the Au-free oxides suggests that the reducibility of the oxide is in fact the dominating factor.

3.3 SUMMARY

Pure and mixed cerium and lanthanum oxides are the focus of much interest due to their increasingly wide application in catalysis, absorption and related fields. Hence, there is a need to develop carefully controlled synthesis methods for such mixed oxides, and to establish clear correlations between structure, composition, and activity.

In the present study, we demonstrated the synthesis of mesoporous pure and mixed lanthanum and cerium oxides via a straightforward microemulsion-templated approach, resulting

in materials with well-defined nanostructure and surface areas as high as ~110 m^2/g at 450 ^oC. Most significantly, the carefully controlled microemulsion environment allowed the synthesis of highly homogeneous mixed La/Ce-oxides across the entire composition range. Interestingly, all $La_xCe_{1-x}O_y$ crystallize in the fluorite structure of ceria, even for La contents as high as 90%. In addition to structural properties such as lattice parameter and particle size, varying the La content also allows fine tailoring of the reducibility of the samples due to the formation of oxygen vacancies upon incorporation of La in the ceria lattice.

The controllable pore size distribution along with tunable reducibility provides a promising avenue for tailored materials for catalysis and separation technology. We are currently extending the described approach beyond tailoring reducibility or oxygen storage capacity towards the introduction of carefully controlled multifunctionality, such as combination of catalytic and adsorptive properties.

The present study also aimed to elucidate the impact of La addition on the reactivity of Au-based La/Ce-mixed oxides in WGS. Beyond the reducibility study of Au-free oxide supports, deposition of Au onto these oxides gives rise to an additional, low-temperature reduction peak, presumably due to hydrogen spill-over from the noble metal onto the oxide support. The WGS activity of $Au/La_xCe_{1-x}O_y$ catalysts demonstrates that appropriate La addition can result in strong increases in reactivity. Most significantly, the WGS activity of $Au/La_xCe_{1-x}O_y$ could be closely correlated with the reducibility of the oxide supports.

Overall, the study demonstrates that carefully controlled synthesis of nanostructured catalysts with uniform, tailored composition allows for fine control of reactive properties of these materials, and might ultimately open the way towards a more rational design of catalysts.

4.0 MORPHOLOGY TAILORING OF GOLD-BASED WGS CATALYSTS

Oxide-supported Au catalysts have been studied extensively since Haruta et al. discovered the exceptional activity of Au nanoparticles for low temperature CO oxidation [94, 176]. To improve the activity of ceria, several strategies have been widely pursued, such as compositional and structural tailoring. On one hand, doping of ceria has been shown to result in improved performance in WGS due to increased reducibility and oxygen storage capacity [78, 85, 177-182]. On the other hand, several research groups have recently shown that nanostructuring can also significantly affect the redox activity of pure ceria [71, 94, 95, 183, 184]. Especially CeO_2 nanrods show superior activity compared to (polyhedral) nanoparticles in CO oxidation and in WGS [94, 95, 185]. However, to-date, only very few studies have focused on doped ceria with well-defined nanostructures, i.e. on the combined effect of simultaneous structural and compositional tailoring [184, 186]. In particular, no reports exist to-date on mixed $La_xCe_{1-x}O_y$ nanorods as catalyst support for WGS, despite the above mentioned findings that both La-doping and nanostructuring into rod shapes results in significantly enhanced WGS activity.

The main target of the present study was therefore to develop a better understanding of the function of rare earth additives (here: La) in the redox properties and WGS activity of CeO_2 nanorods. Highly homogenous mixed $La_xCe_{1-x}O_y$ nanorods were synthesized over a broad range of La content (0-50%) via a carefully controlled hydrothermal synthesis. After depositing Au onto these nanorods—while carefully controlling for uniform metal loading, surface area and

particle aspect ratio—these catalyst were evaluated in WGS, and showed superior activity compared to analogous nanoparticle catalysts. However, unlike for nanoparticle catalysts, we find that La doping does not yield improved WGS activity for nanorod-based catalysts.

4.1 EXPERIMENTAL SECTION

4.1.1 Materials and syntheses

$Au/La_xCe_{1-x}O_y$ catalysts were prepared via a two-step synthesis. First, the oxide supports with controlled morphologies were synthesized via hydrothermal or micro-emulsion methods, followed by Au loading via deposition–precipitation (DP).

CeO_2 and $La_xCe_{1-x}O_y$ nanorods were prepared by hydrothermal synthesis. For example, to prepare $La_{0.5}Ce_{0.5}O_{1.75}$ nanorods, 0.376 g of $La(NO_3)_3\ 6H_2O$ (99+%, Sigma-Aldrich) and 0.376 g of $Ce(NO_3)_3\ 6H_2O$ (99+%, Sigma-Aldrich) were dissolved in 8 ml DI water. 30ml of NaOH (98+%, Sigma-Aldrich) solution (3.5 M) was rapidly added under vigorous stirring. After 30 min of stirring, the slurry was transferred into a 50 ml autoclave, heated to 100^oC under autogenous pressure for 72 h, and then allowed to cool to room temperature. The product was washed by DI water and collected via centrifugation to remove any ionic remnants until the pH of the solution was 7.0. After drying at 100 ^oC overnight and calcination at 450 ^oC for 4 h, the final product was obtained.

Pure CeO_2 nanoparticles were prepared through hydrolysis of cerium isopropoxide in a reverse (water-in-oil) microemulsion (see details in 3.1.1).

All $Au/La_xCe_{1-x}O_y$ catalysts were prepared from the respective oxide nanostructures via deposition–precipitation (DP) (see details in 3.1.3). The nominal Au loading for all catalysts was 5 wt%.

4.1.2 Characterization

The specific surface area was determined via nitrogen sorption in a Micromeritics ASAP 2020 gas adsorption analyzer using the BET method. Prior to the measurement, the samples were degassed for 2 h at 200 ^oC under high vacuum. Elemental analysis to determine Au loading and La/Ce ratio were performed using inductively coupled plasma optical emission spectroscopy (ICP-OES) on a Thermo iCAP 6500 spectrometer, and using energy-dispersive x-ray analysis (EDX) equipped on transmission electron microscopy (JEOL-2100F). The EDX analysis is based on the microdomains of nanorods under TEM. The X-ray diffraction (XRD) measurements were performed with a high-resolution powder X-ray diffractometer (Bruker AXS D8) in line focus mode employing Cu-Kα radiation (λ = 1.5406 Å). Crystal phases were identified based on JCPDS cards. Sample morphology was determined by transmission electron microscopy (JEOL-200CX, JEOL-2100F). Lattice spacings were calculated by fast Fourier transformation (FFT) analysis of the high resolution TEM images. Temperature-programmed reduction by hydrogen (H_2-TPR) was conducted using a Micromeritics Chemisorb 2750 system equipped with a thermal conductivity detector. During the TPR analysis, the samples were first oxidized in 5vol% O_2/He at 450 ^oC for 2 h, and then TPR was performed by heating the sample (100 mg) at 5 ℃/min to 900 ℃ in a 10 vol% H_2/Ar flow (30 ml/min). A cold trap filled with acetone-dry ice mixture was placed between reactor and TCD to remove water vapor.

4.1.3 Catalyst tests

Water-gas shift tests were carried out in a 5 mm ID quartz glass tube heated via insertion into a high-temperature tube furnace at ambient pressure. The catalyst powder (50 mg) was supported within the tube on either end by quartz glass felt plugs. Water was injected via a syringe pump and vaporized in a heated line before entering the reactor. The composition of the mixture after water addition was 10.8% H_2O, 2.1% CO, and 87.1% He. The total flow rate of gas was typically around 100 CCM resulting in space velocities of ~150,000 h^{-1}. The exit gas passed through a condenser to eliminate H_2O from the stream and then was analyzed by an Agilent 3000A MicroGC equipped with thermal conductivity detector (TCD). In order to assure reaching steady state after adjusting operating conditions (such as temperature steps), CO conversion was measured repeatedly until the conversion varied less than 1% over a duration of 5 minutes. No methane was detected at any conditions used in this work. The inert helium feed was used as internal standard to calculate the total gas flow rate after water condensation and the concentration of water leaving the reactor.

4.2 RESULTS AND DISCUSSION

4.2.1 Nanorod morphology

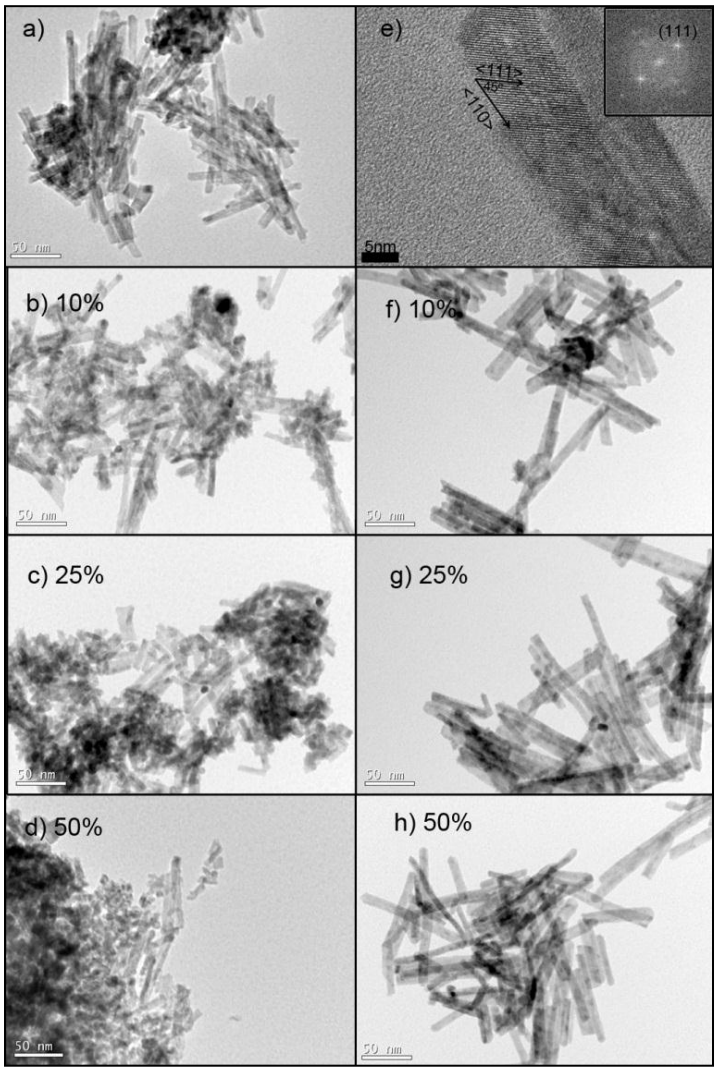

Figure 20. TEM (a) and HR-TEM (b) images of CeO_2 nanorods. TEM images of nanorods with different La contents (%) prepared by 24 hr hydrothermal synthesis (b-d); and by 72 hr hydrothermal synthesis (f-h), respectively.

As shown in Figure 20-a, pure CeO_2 samples prepared via hydrothermal synthesis (and after calcination at 450^{o}C) form nanorods. Previous studies have demonstrated superior catalytic

activity for such ceria nanorods and explained this due to preferential exposure of highly reactive crystal planes [95, 187-189]: CeO_2 nanoparticles with face-centered cubic crystal structure mostly expose {111} planes, which are thermodynamically most stable and least reducible [78, 95, 182]. In contrast to that, HR-TEM (Figure 20-b) shows that nanorods expose preferentially {110} orientations: Fast Fourier transformation (FFT) analysis of the two-dimensional crystal lattice image of a nanorod with a growth axis perpendicular to the electron beam yields a lattice parameter of 3.13948 Å, in close agreement with the {111} plane spacing (3.1250 Å) of cubic CeO_2 (*JCPDS* 34-0394). Based on the measured interplanar spacings and the plane-intersecting angle, we can hence identify {111} planes and the exposed active {110} side planes of the rod, confirming previous results [94, 95].

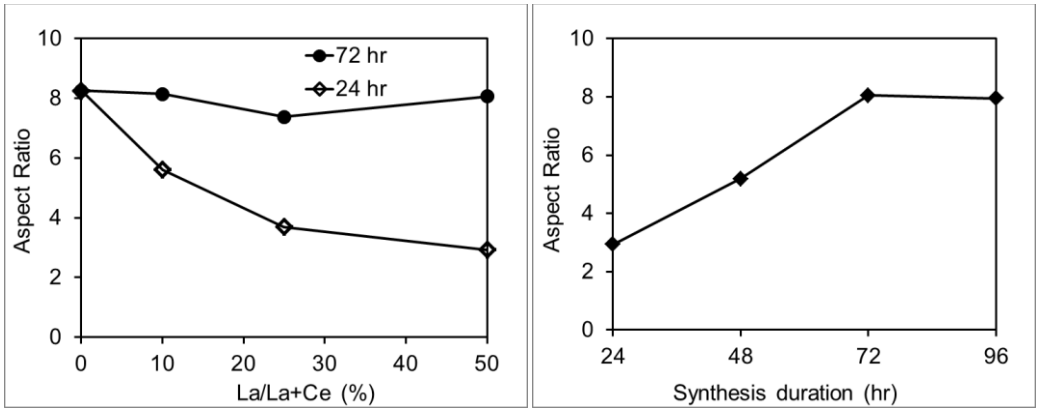

Figure 21. Left: Average aspect ratio of $La_{0.5}Ce_{0.5}O_{1.75}$ nanorods as function of synthesis duration (left). Right: Average aspect ratio of $La_xCe_{1-x}O_y$ as function of La content (0% - 50%) after 24 hr (open symbols) and 72 hr (filled symbols) synthesis time, respectively.

In order to take advantage of the superior activity of nanorods for mixed oxide materials, and to ascertain that any difference obtained in the present investigation can be correlated with composition rather than change in aspect ratio of the sample, it is necessary to control the synthesis of $La_xCe_{1-x}O_y$ to yield the same rod-shape morphology. However, as shown in Figure 20 b-d, the $La_xCe_{1-x}O_y$ samples obtained from 24 h hydrothermal synthesis (i.e. identical

conditions as for CeO_2 nanorod synthesis), contain incompletely formed nanorods and nanoparticles. Figure 21 (left) summarizes the results and shows that the aspect ratio of mixed-oxide nanorods drops from 8.3 to 2.9 with increasing La content from 0% to 50%, indicating that the La dopant inhibits the growth of ceria along the [110] direction.

In order to obtain well-defined nanorods with preferential exposure of {110} planes, the duration of the hydrothermal synthesis was extended to allow for complete formation of the final structure. Figure 21 (right) shows the aspect ratio of $La_{0.5}Ce_{0.5}O_{1.75}$ as a function of synthesis duration, illustrating the growth of mixed lanthana/ceria nanorods over a 72-hr period (3 days). After 72-hr hydrothermal reaction, the $La_xCe_{1-x}O_y$ exhibit uniform rod-shape structures (Figure 20 f-h) with similar average aspect ratios of 7.38-8.14 (Table 6), comparable to that of pure CeO_2 nanorods (8.3). Correspondingly, all nanorod materials also have similar surface areas of 84-99 m^2/g (Table 6). Thus, the controlled synthesis of the $La_xCe_{1-x}O_y$ nanorods allows de-coupling of structural and compositional effects on the activity of the catalysts, and the high aspect-ratio nanorods were consequently used in the reducibility and WGS activity tests.

Table 6. Theoretical and experimental value of the pure and mixed-oxide nanorods' lattice parameter, surface area and aspect ratio

	Lattice Parameter (Å)			BET surface area (m^2/g)	Average aspect ratio
	Theoretical	Experimental NR	Experimental NP		
CeO_2	5.3950	5.4239	5.4250	99.0	8.3
$La_{0.1}Ce_{0.9}O_{1.95}$	N.A.*	5.4484	5.4644	91.2	8.1
$La_{0.25}Ce_{0.75}O_{1.875}$	5.4820	5.4942	5.4966	84.6	7.4
$La_{0.5}Ce_{0.5}O_{1.75}$	5.5720	5.5832	5.5702	87.8	8.1

* The lattice parameter of $La_{0.1}Ce_{0.9}O_{1.95}$ was not reported in the reference [25].

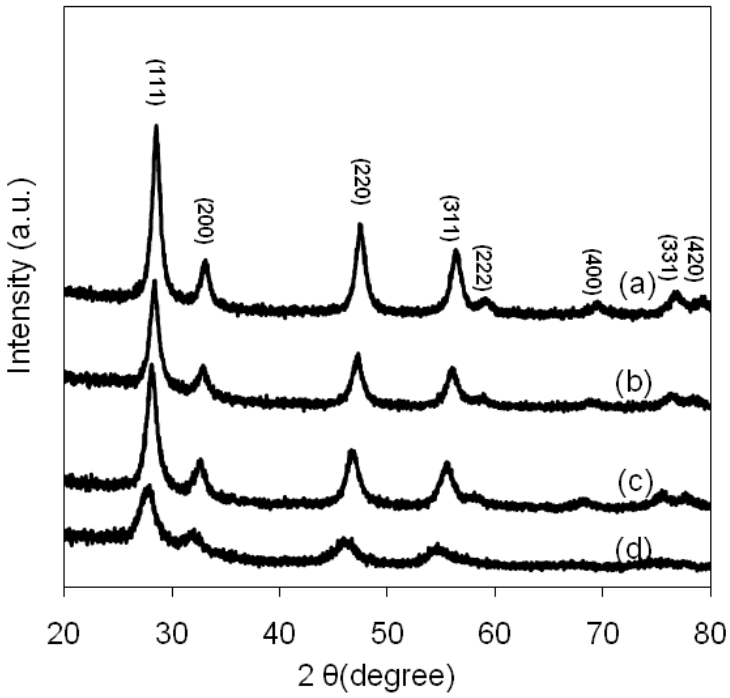

Figure 22. X-ray diffraction patterns of $La_xCe_{1-x}O_y$ nanorod materials with different lanthanum content: (a) 0%, (b) 10%, (c) 25%, (d) 50% (percent is mol% metal, i.e. La/(Ce+La)).

The compositional homogeneity of the mixed oxide nanorods was confirmed via XRD, high resolution TEM, and microdomain EDX. Figure 22 shows the XRD patterns of $La_xCe_{1-x}O_y$ nanorods prepared by hydrothermal synthesis after calcination at 450 ^oC. The sharp diffraction peaks in figure 3-a are in a good agreement with the CeO_2 standard (*JCPDS* 34-0394). The XRD diffractograms of all $La_xCe_{1-x}O_y$ exhibit a shifted fluoride crystal structure without the presence of second phase, such as La_2O_3, (Figure 22 b-d), indicating the formation of homogenous mixed oxides in which La^{3+} ions are embedded into the cubic crystal lattice of CeO_2. The lattice parameters of $La_xCe_{1-x}O_y$ nanorods calculated from these diffraction patterns are in a good agreement with theoretical values reported by Morris et al. [142] (see Table 6) as well as with our previously reported observations for $La_xCe_{1-x}O_y$ nanoparticles, despite the significant differences in the materials morphologies [182]. This is further confirmed via high resolution

TEM (Figure 23), where the lattice spacing of $La_xCe_{1-x}O_y$ was directly determined via FFT analysis of the images, as shown in fig. 4. As the La loading ("x") increases from 0 to 0.5, the lattice spacing of (111) expands from 3.13948 Å to 3.36638 Å. This lattice expansion can be attributed to a combination of the larger ionic radius of La^{3+} vs Ce^{4+} and the effect of the increasing number of oxygen vacancies due to La doping [142, 159]. Finally, EDX analysis of microdomains of the samples showed uniform La:Ce ratios in good agreement with the expected values from the synthesis (see Table 8).

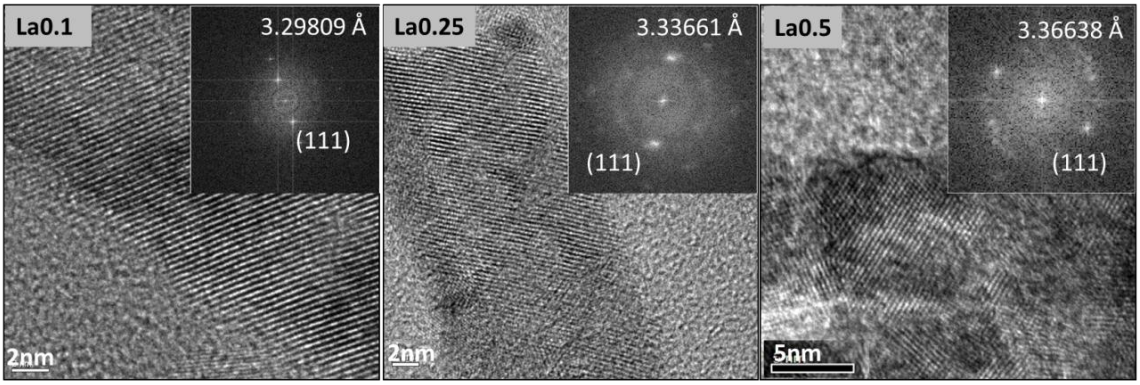

Figure 23. HR-TEM and FFT analysis (inserted) of $La_xCe_{1-x}O_y$ with x = 0.1, 0.25 and 0.5.

Table 7. Reduction Temperature and hydrogen consumption

	Reduction Temp. (°C)	H_2 consumption (μmol H_2/g oxide)
CeO_2 (NP)	420	396
CeO_2 (NR)	355	781
$La_{0.1}Ce_{0.9}O_{1.95}$	340	461
$La_{0.25}Ce_{0.75}O_{1.875}$	345	388
$La_{0.5}Ce_{0.5}O_{1.75}$	420	336

Table 8. Measured Au loading and La content of $Au/La_xCe_{1-x}O_y$

	Au wt. %	Average Particle Size of Au	La/(La+Ce) (*from EDX*)
Au/CeO_2 (NP)	3.8	<3 nm*	0
Au/CeO_2 (NR)	3.9	2.8	0
$Au/La_{0.1}Ce_{0.9}O_{1.95}$	4.1	2.5	0.11
$Au/La_{0.25}Ce_{0.75}O_{1.875}$	3.8	2.6	0.25
$Au/La_{0.5}Ce_{0.5}O_{1.75}$	4.1	2.6	0.49

***** As reported previously, the Au particle size on CeO_2 nanoparticles is <3 nm. However, it was not possible to determine the exact Au particle size on CeO_2 nanoparticle supports via TEM or chemisorptions due to their similar contrast and chemisorption properties.[78]

4.2.2 Reducibility of $La_xCe_{1-x}O_y$

In order to evaluate the redox properties of these materials, temperature-programmed reduction in hydrogen (H_2-TPR) has been used extensively in the literature [95]. Active metals, such as Au and Cu, show low activity for H_2O dissociation, which is the rate determining step for WGS [52, 53]. In comparison, ceria has no reported WGS activity but is active in water dissociation due to the presence of reduced Ce^{3+} sites [53]. Based on this mechanism, the reducibility of oxide supports can be expected to have a strong impact to the catalytic WGS activity of $Au/La_xCe_{1-x}O_y$ catalysts.

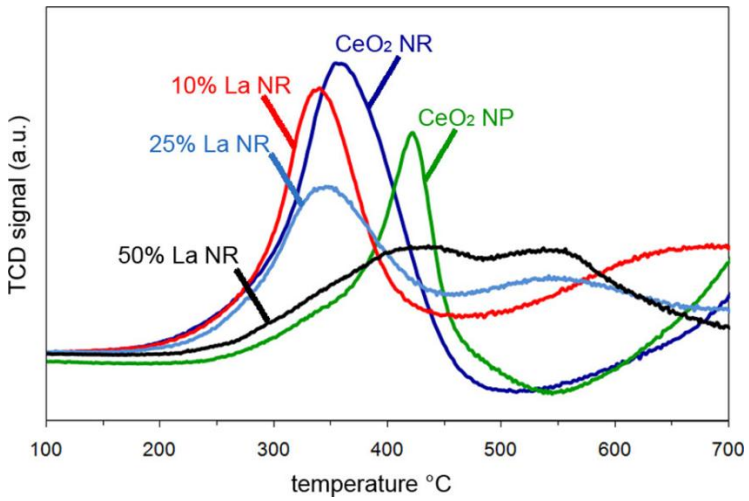

Figure 24. H_2-TPR profiles of $La_xCe_{1-x}O_y$ nanorods with different La content (10%-50%), ceria nanorods (NR) and nanoparticles (NP)

Figure 24 shows the TPR profile for pure and mixed oxide samples. For pure CeO_2 nanoparticles, two reduction peaks are visible, one at low temperature (~420 ^oC) and one at high temperature (>700^oC, not fully shown in the graph), which can be attributed to the reduction of surface and of bulk ceria, respectively [190, 191]. Only the low-temperature surface reduction is relevant in the present context, since it occurs in the temperature range of interest for WGS (T<500^oC). In comparison, CeO_2 nanorods have a lower reduction temperature (360 vs. 420 ^oC) and a much higher H_2 consumption (781.0 vs. 395.5 μmol/g; calculated from an integration of the area under the curves), indicating a much higher overall reducibility. This can be traced back to the preferential exposure of active {110} crystal planes as discussed in the previous section 4.2.1.

Remarkably, doping CeO_2 nanorods with La does not significantly improve the reducibility of the nanorods. As shown in figure 5, the onset temperature for the reduction of the three samples with 0%, 10% and 25% La doping is unchanged (~180 ^oC), and the peak reduction temperature shows only a minor shift by ~15 ^oC upon La doping. When the La content is increased to 50%, however, a strong increase in the onset temperature for reduction to 220 ^oC is

observed and a strongly increased reduction peak temperature of ~420 ^{o}C are observed, indicating that a higher La content is in fact detrimental to the reducibility of the mixed oxide nanorods.

Beyond the change in reduction temperatures, the area under the reduction peak, representing the total amount of reducible sites (quantified in the specific hydrogen consumption values in Table 7), shows a more obvious and pronounced trend towards lower values with increasing La content for all mixed-oxide nanorods. This decrease in H_2 consumption indicates a loss in reducible sites with increasing La doping which can be explained by the substitution of reducible Ce^{4+} by La^{3+}, which is non-reducible in this low-temperature range. Interestingly, this result differs from our previous investigation of mixed Ce/La-oxide nanoparticles where La dopings up to ~25% (i.e. up to $La_{0.25}Ce_{0.75}O_{1.875}$) resulted in a strong increase in reducible sites compared to pure CeO_2 nanoparticles [78, 182]. A possible explanation for this discrepancy can be found in the different reducibility of the terminal planes for the different nanostructures: For nanoparticles, which are terminated predominantly by {111} planes, the La doping facilitates the conversion of Ce^{4+}/Ce^{3+} in and near the {111} planes, thus creating defects in the oxygen sub-lattice, enhancing the oxygen mobility, and hence increasing the overall reducibility of the mixed oxide nanoparticles [182]. In contrast to that, the dopant cannot further "activate" the terminal {110} planes in the nanorods, which already have a much lower formation energy for defects than the {111} planes [95, 189]. Doping hence results only in the above described decrease in the number of reducible oxygen sites, and hence a decrease in reducibility.

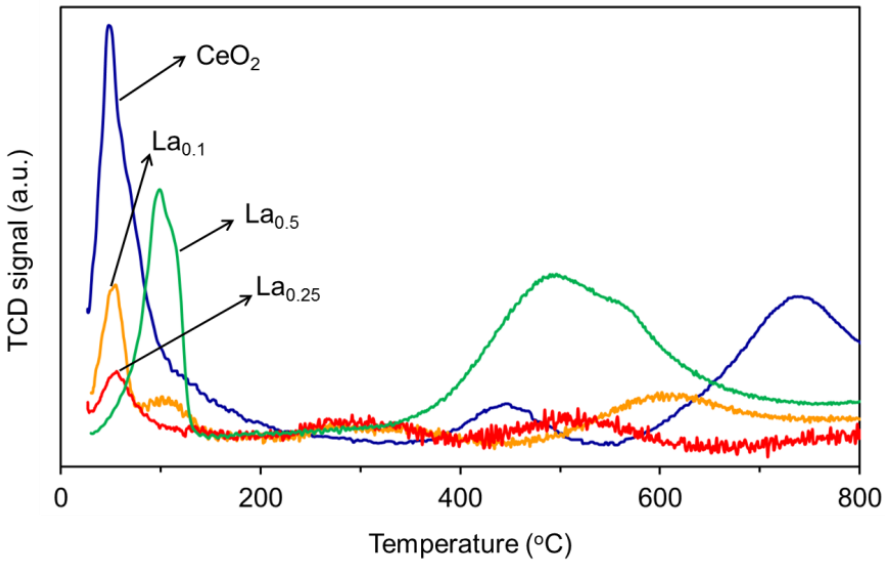

Figure 25. H_2-TPR profiles of $Au/La_xCe_{1-x}O_y$ nanorods with different La content (10%-50%)

The reducibility of $La_xCe_{1-x}O_y$ is strongly affected by the Au deposition, as shown in Figure 25. The most important change is that a new reduction peak at very low temperature (~100 ^oC) appears for $Au/La_xCe_{1-x}O_y$, which has been attributed to the reduction of oxidized Au species [77, 168-170] or to reduction of the oxide via hydrogen spill-over from the metal to the support [43, 171, 172]. Since the surface reduction peaks for all oxide supports are significantly decreased after Au deposition, it indicates that most available oxygen is reduced at this lower temperature, and thus suggests that H_2 dissociation on Au and spill-over onto the adjacent oxide surface are more likely to be responsible for the strong low-temperature reduction peak.

The trend in the reducibility of the Au-based catalysts is in close agreement with that of the oxide supports (Figure 24). $Au/La_xCe_{1-x}O_y$ nanorods have very similar reduction temperatures up to x = 0.5. Au/CeO_2 shows the highest reduction peak, indicating that lanthanum replaces reducible Ce^{4+}, and hence decreases the reducibility of these catalysts.

Overall, these results hence confirm our previous report that La doping results in two counter-acting effects [182]: On one hand, it increases the reducibility of the samples by

lowering the reduction energy and the activation energy for oxygen migration in CeO_2; on the other hand, it decreases the reducibility by reducing the absolute number of reducible Ce^{4+}. For 10% and 25% La, the balance of the two effects causes a slightly lower reduction peak with similar onset temperature and less reducible sites. However, when the La doping is increased to 50%, the second effect becomes dominant, resulting in a net loss of reducibility of the sample. (It should be noted here that the broad peaks at 500-600^oC for $La_{0.25}Ce_{0.75}O_{1.875}$ and $La_{0.5}Ce_{0.5}O_{1.75}$ in figure 5 are not due to sample reduction, but due to decomposition of surface carbonates. La_2O_3 is well known to form surface hydroxy-carbonates, $La_2(OH)_4(CO_3)$, when exposed to air, which decompose to $La_2O_2CO_3$ and further to La_2O_3 in this temperature range [153, 192].)

4.2.3 WGS activity

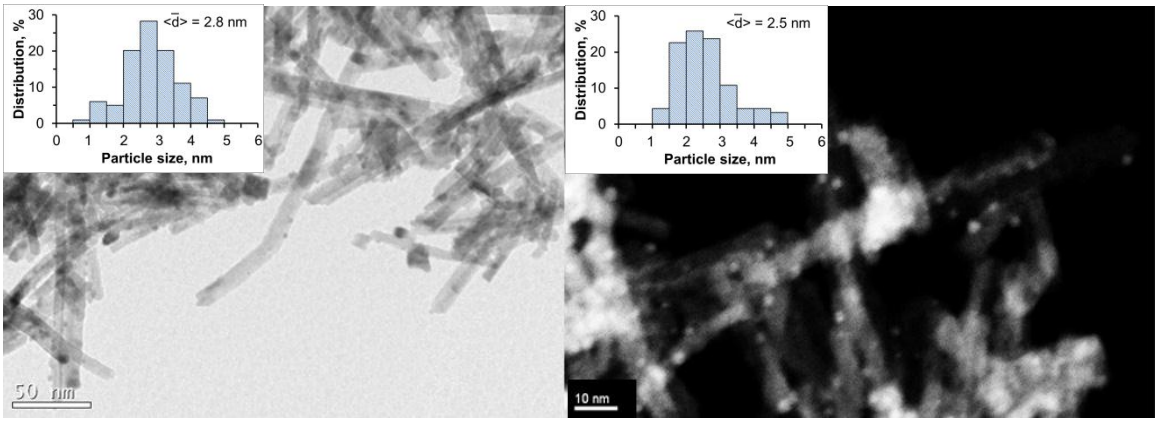

Figure 26. TEM of Au/CeO_2 (left) and HAADF-STEM of $Au/La_{0.25}Ce_{0.75}O_{1.875}$ (right). The insets show the Au nanoparticle distributions determined from respective TEM images.

In order to further identify composition-activity correlations, Au/mixed oxide WGS catalysts were prepared via deposition-precipitation of Au onto $La_xCe_{1-x}O_y$ nanorods with near-identical aspect ratios. Elemental analysis after deposition-precipitation (DP) of Au (Table 8) confirms Au loadings of ~4 wt% for all samples, and La contents in close agreement with the expected values.

As shown in the TEM and HAADF-STEM images in Figure 26, $La_xCe_{1-x}O_y$ nanorods maintained their morphology and dimensions during the DP process. Particle sizes and size distributions determined from bright-field and dark-field images show good agreement with average Au particle sizes of ~2.6-2.8 nm and fairly narrow particle size distributions (see inserted bar graphs in Figure 26). While there is an on-going debate in the literature over the oxidation state [40, 45] and size [38, 39] of the active Au species in WGS catalysis, the present investigation did not aim to contribute to this discussion, but rather focus solely on the role of the oxide support. However, by following identical and carefully controlled deposition-precipitation and pretreatment methods, and assuring identical Au loadings, particle sizes, and distribution on the different catalysts, all catalysts should have the same number and type of active Au sites, and hence the difference in performance of the $Au/La_xCe_{1-x}O_y$ catalysts can be expected to be entirely due to the difference in the oxide supports.

The WGS activity of $Au/La_xCe_{1-x}O_y$ was tested in fixed-bed reactor studies feeding a mix of 10.8% H_2O and 2.1% CO in He into a 5mm ID quartz-glass tube at a space velocity of ~150,000 h^{-1} (see experimental section for details). Figure 27 summarizes the results for $Au/La_xCe_{1-x}O_y$ samples, ranging from pure CeO_2 to 50% La-content nanorod supports, in terms of CO conversion as function of temperature. For comparison, Au/CeO_2 nanoparticle catalysts (prepared via a microemulsion-templated synthesis) and a commercial Cu-based WGS catalyst (HiFUEL W220, Alfa Aesar) were included in the tests.

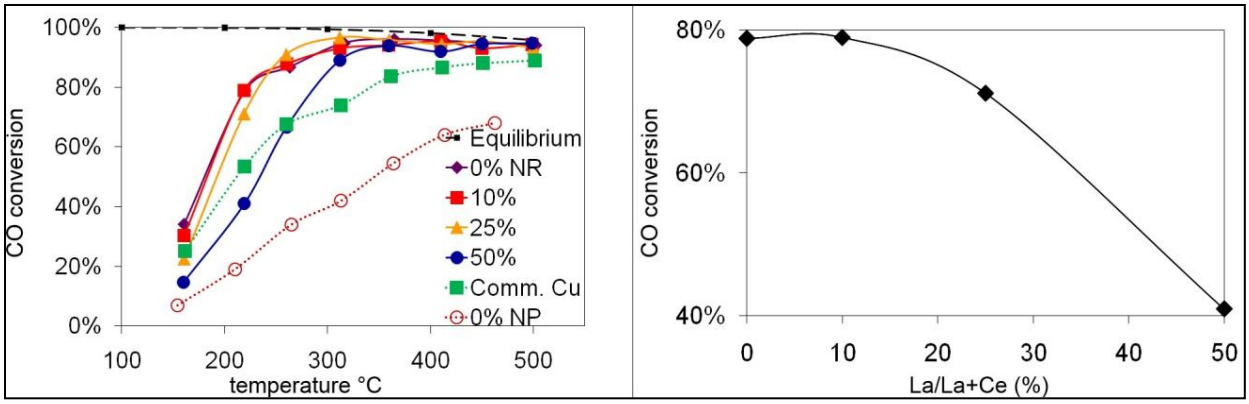

Figure 27. Left graph: CO conversion vs temperature in WGS for $Au/La_xCe_{1-x}O_y$ nanorods (NR) with different La content (0%-50%), Au/CeO_2 (0% NP) and commercial Cu-based WGS catalyst ("Comm. Cu"). Right graph: CO conversion (as measure of catalytic WGS activity) of $Au/La_xCe_{1-x}O_y$ NR as function of La content at a fixed temperature of 220 ℃.

The most striking feature in the figure is the much higher activity of the nanorod-based catalysts in comparison to the Au/CeO_2 nanoparticle catalyst, with the best nanorod-based catalysts reaching equilibrium conversions at experimental conditions at temperatures as low as ~270 ^oC. This high activity of the nanorod catalysts correlates well with the reducibility data, i.e. the lower reduction temperature and larger number of reducible sites discussed above, and is in agreement with previous reports [94, 188]. It is worthwhile to notice the Au/CeO_2 nanorod catalysts show excellent low-temperature WGS activity even compared to the commercial Cu-based catalyst.

La doping has very little impact on this high WGS activity up to a La content of 25%, while a further increase to 50% La results in a significant drop in activity, in particular in the temperature range below ~350 ^oC. This again closely mirrors the trends seen in the reducibility of the samples, where an increase of La content from 25% to 50% results in a strong loss of reducibility below ~350 ^oC (see Figure 24). This can be more clearly seen in the right-hand plot in Figure 27, where CO conversion is shown as a function of La content for one fixed reaction temperature (T= 220^oC). Comparing the CO conversion curves (Figure 27) with the reducibility

trend (Figure 24, Figure 25 and Table 7), it is apparent that both activity and reducibility closely follow the same trend with La content of the Au/$La_xCe_{1-x}O_y$ nanorods.

Finally, the impact of aspect ratio on reducibility and WGS activity was studied separately by comparing $La_{0.25}Ce_{0.75}O_{1.875}$ nanorods obtained at different synthesis durations (24 hr and 72 hr). As discussed before, the aspect ratio of $La_xCe_{1-x}O_y$, which determines the preferential exposure of the active {110} crystal plane, increases as the hydrothermal synthesis is extended up to 72 hrs.

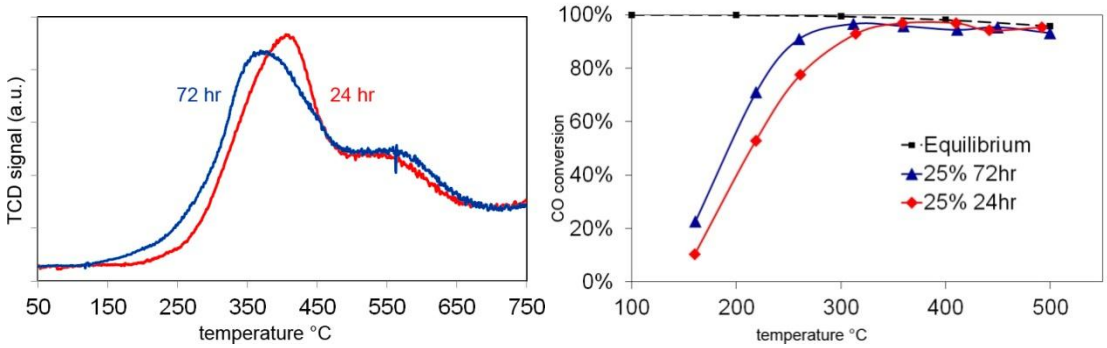

Figure 28. Left: H_2-TPR profiles of $La_{0.25}Ce_{0.75}O_{1.875}$ nanorods. Right: CO conversion vs temperature in WGS for Au/$La_{0.25}Ce_{0.75}O_{1.825}$ nanorods synthesized with different hydrothermal durations

As expected from the increased exposure of {110} planes, the high aspect-ratio nanorods (i.e. after 72 hr synthesis time) show slightly improved reducibility, especially in the low temperature range <400 ^oC, with reduction starting at 110 ^oC, i.e. ~70 ^oC lower than for the low aspect-ratio sample (Figure 28, left graph). Furthermore, the WGS activity of the catalysts shows excellent agreement with this difference in reducibility between the nanorods: As shown in Figure 28 (right), the high aspect-ratio Au/$La_{0.25}Ce_{0.75}O_{1.875}$ (i.e. after Au loading) shows 10~20% higher CO conversion at low temperature (<350 ^oC) than the low aspect-ratio sample. These differences thus demonstrate again the significance of establishing firm morphological control for these catalysts, and confirm the strong and direct correlation between reducibility and activity of Au/ceria-based WGS catalysts.

4.3 SUMMARY

We demonstrated the synthesis of CeO_2 and, for the first time, mixed $La_xCe_{1-x}O_y$ nanorods via a simple hydrothermal reaction at high concentration of NaOH and without surfactant. The La doping was found to act as an inhibiter for the growth of $La_xCe_{1-x}O_y$ nanorods along the [110] direction. However, by controlling the hydrothermal duration, $La_xCe_{1-x}O_y$ nanorods with high aspect ratio and surface area could be synthesized with aspect ratio comparable to those previously reported pure CeO_2 nanorods. The use of these carefully controlled pure and mixed nanorods as supports for (equally uniform) Au nanoparticles allowed study of whether previous correlations between reducibility and activity for nanoparticle-based Au/mixed oxide catalysts are transferrable to nanorod catalysts.

In agreement with earlier reports, we found that the difference in reducibility between nanoparticles and nanorods can be attributed to preferential exposure of different terminal crystal planes. The preferential exposure of {110} crystal planes for CeO_2 nanorods results in lower reduction temperature and an increased number of reducible sites in the temperature range of WGS, resulting in strongly increased WGS activity compared to nanoparticle-based Au/ceria catalysts. However, unlike for nanoparticle-based catalysts, the reducibility of CeO_2 nanorods cannot be enhanced significantly by La doping, suggesting that the already low reduction energy of Ce^{4+} along the {110} planes cannot be further decreased by La. As a result, the WGS activity of pure Au/CeO_2 and $Au/La_xCe_{1-x}O_y$ with $x \leq 25\%$ is essentially unchanged, with conversions significantly above those both for Au/ceria nanoparticle catalysts and a commercial Cu-based catalyst. Further increase in La content results in decreased activity due to the decrease in reducible oxygen sites.

The present study hence confirms that the strong relationship between catalyst reducibility and WGS catalytic activity holds independent of the morphology of the oxide support, i.e. it is applicable both to CeO_2 nanoparticle and nanorod-based catalysts.

5.0 MULTIFUNCTIONAL SULFUR RESISTANT LA_2O_3/M/CEO_2 (M=AU,PT) CATALYST FOR WATER-GAS SHIFT REACTION

Sulfur contaminants in fuel stream is one of most sever issues leading to catalyst deactivation in water-gas shift reaction [21, 116, 119]. Sulfur poisoning can eventually shut down the Low-temperature Shift (LTS) reactor, since Cu-based catalysts can be irreversibly poisoned by sulfur with low concentration at the reaction temperature [116, 117]. As a result, it is necessary to protect the catalyst with separated desulfurization units. Even though the "sour WGS catalyst", such as MoS_2, has been developed, since it requirements a minimum sulfur concentration in the fuel stream, these catalysts have limited applications in production of syngas from coal and heavy oil gasification [118].

Recently, noble metal (Au, Pt) on reducible oxide (CeO_2, TiO_2, ZrO_2) support catalysts have been widely studied due to their high activity and wide operational temperature range [21, 193]. Unfortunately, similar to Cu-based LTS catalysts, they are extremely sensitive to sulfur, and can be deactivated due to the formation of metal sulfide or organic sulfide/sulfate covered metals [120]. Although the there are several approaches against S-poisoning have been reported, most of these efforts were aiming at increase the sulfur tolerance of catalysts by introducing sacrificial metals, which will be consumed [124, 125].

In addition, the noble metals, especially Au, are well-known for their instability in WGS. The major reasons include the sintering of the particle under reducing atmosphere and the

wetting of metal-metal oxide interface, leading to the agglomeration of metal nanoparticles [193]. In order to stabilize the noble metal and maintain the high activity, the decoration of thin layer oxide has been reported recently [110, 194-197]. However, such strategy adopted SiO_2 as the decorating materials with the only function to regulate the particle's mobility.

Herein, we present a novel strategy of preparation of highly stable S-resistant WGS catalyst, which simultaneously remove the sulfur contaminants from the stream. This catalyst design, as shown in Figure 29, includes the catalytic component - M/CeO_2 (M = Pt, Au) with high WGS activity [78] and S-capturing component-La_2O_3, which has been reported as a regenerative H_2S adsorption and removal material [151, 156]. The La_2O_3 was incorporated in the catalytic system by post-decoration method, which is based on the synthesis technique for Au catalyst stabilized by SiO_2 [114, 194]. In addition to the stabilization function, unlike SiO_2, the La_2O_3 in this study actively capture H_2S in reaction, leading to a novel type of multifunctional periodic sulfur resistant catalyst.

5.1 EXPERIMENTAL SECTION

5.1.1 Catalyst preparation

Firstly, CeO_2 supports were prepared via hydrothermal and microemulsion synthesis, as discussed in 4.1.1. Au/CeO_2 catalysts were prepared via deposition–precipitation (DP) [78, 131], as discussed in 3.1.3.

Pt/CeO_2 were prepared by wet-impregnation using $Pt(NH_3)_4(NO_3)_2$. 0.008 g of $Pt(NH_3)_4(NO_3)_2$ was firstly dissolved in 0.4 g of DI water. 0.258 g of CeO_2 (prepared by

hydrothermal method, as described above) was then added into the solution. The slurry was aged overnight, dried at 100 ^{o}C, and then calcined at 400 ^{o}C for 2 h. Pt/Al_2O_3 were prepared by same method using commercial γ-Al_2O_3 (99.97%, Alfa Aesar) as support.

La_2O_3/M/CeO_2 (M=Au, Pt) were prepared by surface decoration using lanthanum isopropoxide (Alfa Aesar, La 40%) and previously prepared M/CeO_2. For example, 0.67 g lanthanum isopropoxide was dissolved in 100 ml anhydrous 2-propanol (Aldrich, 99.5%) by stirring, refluxed at 95 ^{o}C for 2 hr, and then cooled to room temperature. 0.2 g of Au/CeO_2 was rapidly added under vigorous stirring. After aging with vigorous stirring overnight, the product was collected via centrifuge, dried at 100 ^{o}C for 8 h and calcined at 400 ^{o}C for 2 h.

5.1.2 Characterization

The specific surface area was determined via nitrogen sorption in a Micromeritics ASAP 2020 gas adsorption analyzer using the BET method. Prior to the measurement, the samples were degassed for 2 hr at 200 ^{o}C under high vacuum. The X-ray diffraction (XRD) measurements were performed with a high-resolution powder X-ray diffractometer (Phillips PW1830) in line focus mode employing Cu-Kα radiation (λ = 1.5406 Å). Crystal phases were identified based on JCPDS cards. The sample obtained was dispersed in ethanol by using an ultrasonic bath and deposited on carbon-coated grids for TEM studies. Sample morphology and lattice fringe images were obtained by transmission electron microscopy (JEOL-2000FX) operated at 200 kV.

5.1.3 Catalyst tests

Water-gas shift tests were carried out in a 5 mm ID quartz glass tube heated inserted into a high-temperature tube furnace at ambient pressure. The catalyst powder (50 mg) was supported within the tube on either end by quartz glass felt plugs. Water was injected via a syringe pump (Braintree Scientific, Inc.) and vaporized in a heated line before entering the reactor. The total flow rate of gas was typically around 100 CCM resulting in space velocities of ~150,000 h^{-1}.

For the stability test, the exit gas passed through a condenser to eliminate H_2O from the stream and then was analyzed by an Agilent 3000A Micro GC equipped with thermal conductivity detector (TCD). In order to assure reaching steady state after adjusting operating conditions (such as temperature steps), CO conversion was measured repeatedly until the conversion varied less than 1% over a duration 5 minutes. No methane was detected at any conditions used in this work. The inert helium feed is used as an internal standard, and is used to calculate the total gas flow rate after water condensation and to back-calculate the concentration of water leaving the reactor.

For sour WGS, the exit gas passed through a condenser to eliminate H_2O from the stream and then was continuously analyzed by a mass spectroscopy, Pfeiffer Omnistar equipped with secondary electron multiplier. No methane was detected at any conditions used in this work. The composition of the mixture: WGS without H_2S 10% H_2O, 2% CO, and 88% Ar; WGS with H_2S, 150 ppm H_2S, 10% H_2O, 2% CO, and 87% Ar; regeneration, 25% H_2, 10% H_2O, 65% Ar.

5.2 RESULTS AND DISCUSSION

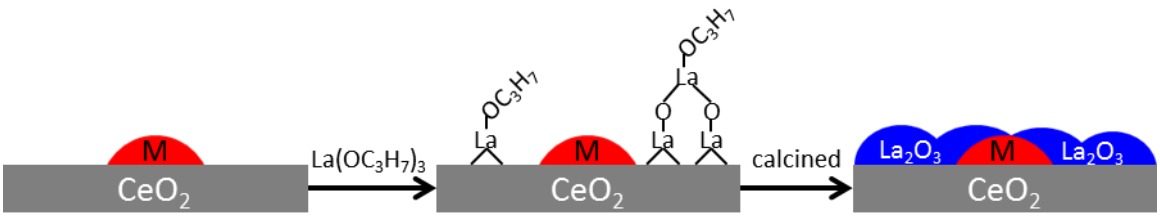

Figure 29. Scheme for the synthesis of $La_2O_3/M/CeO_2$: Pre-formed M/CeO2 was treated in lanthanum isopropoxide ($La(OC_3H_7)_3$) solution, followed by calcination.

Table 9. BET surface area (measured by N_2 sorption) of catalysts

	Surface area
Au/CeO_2	97.93
Pt/CeO_2	95.03
$La_2O_3/Au/CeO_2$	70.36
$La_2O_3/Pt/CeO_2$	54.83

The surface areas of all catalysts samples are summerized in Table 9. Before the decoration, Au/ and Pt/CeO_2 catalysts show very similar surface area of ~95 m^2/g. After decoration, the surface areas of both catalsyts dramatically decrease by 30-40% due to the agglomeration induced by the hydrolysis of lanthanum precursor among the nanorods (as shown by TEM images in Figure 30). The XRD only detects the diffraction of crystallized CeO_2, and hence indicates the La_2O_3 in post-decoration catalyst is amorphous (Figure 31). The high resolution TEM images (Figure 30 c and d) reveal the detailed structure of the amorphous La_2O_3 decoration layer (pointed by arrows), which encapsulated the Au/CeO_2. The measurement of lattice fringe identifies the Au species (measured value = 0.20 nm, theoretical value of (111) = 0.22nm), and hence confirms the structure of this catalyst as we expected (Figure 29): amorphous La_2O_3 forms a coating over the

Au/CeO_2 catalyst. This post-decoration design enables the contact of H_2S with La_2O_3 prior to the metal nanoparticles, leading to a sulfur-resistant catalyst until the decoration layer is saturated.

In order to evaluate the stability in WGS, the catalyst was firstly tested in cyclic WGS reaction without H_2S. As shown in Figure 32, Au/CeO_2 with La_2O_3 decoration dramatically loses the activity after the first cycle, indicating strong deactivation. After surface decoration, as we expected, the initial low-temperature activity is decreased due to the loss of active sites covered by La_2O_3 layer. However, more importantly, $La_2O_3/Au/CeO_2$ catalyst shows stable overall activity during all three cycles, indicating the stabilization effect of the La_2O_3 layer over Au nanoparticles. It is noticed that the catalyst after the decoration shows slightly higher CO conversion at high temperature (350-450 ^oC). This observation can be explained by the formation of La_2O_3-CeO_2 oxide mixture at the interface, which has higher WGS activity than pure CeO_2 [78, 182].

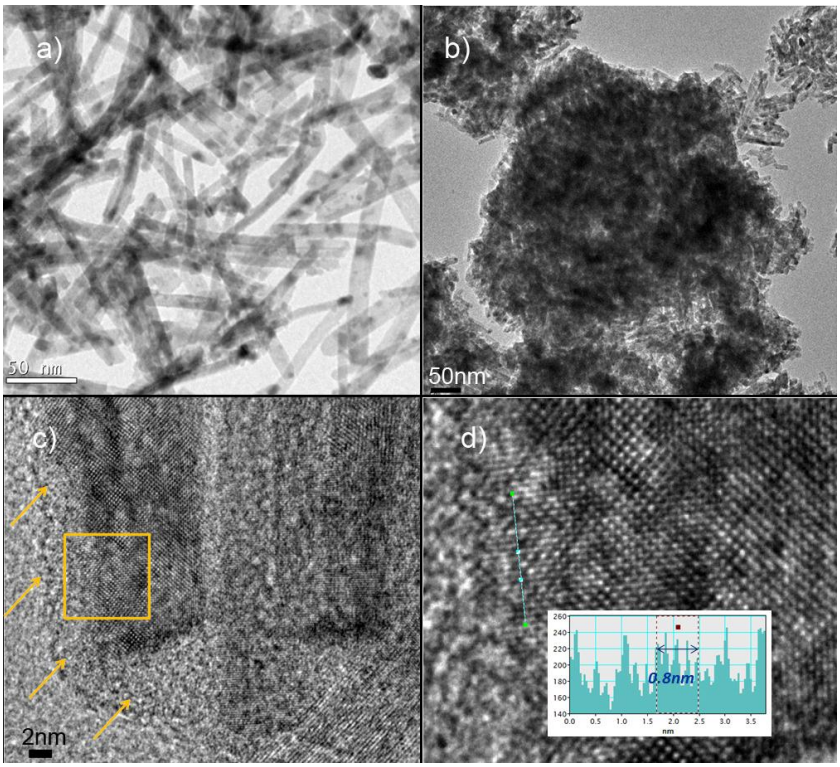

Figure 30. TEM images of Au/CeO_2 nanorods (a) and La_2O_3-deocrated Au/CeO_2 (b-d).

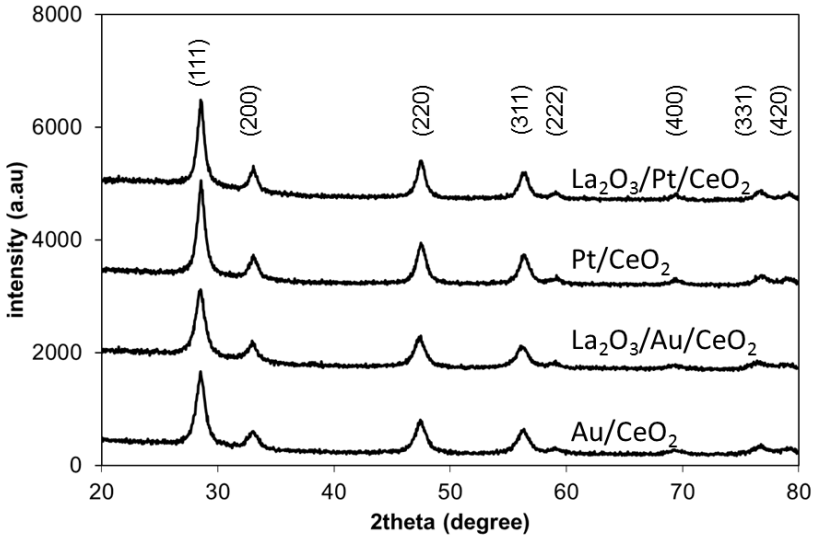

Figure 31. XRD patterns of catalysts after 400 ^{o}C calcination.

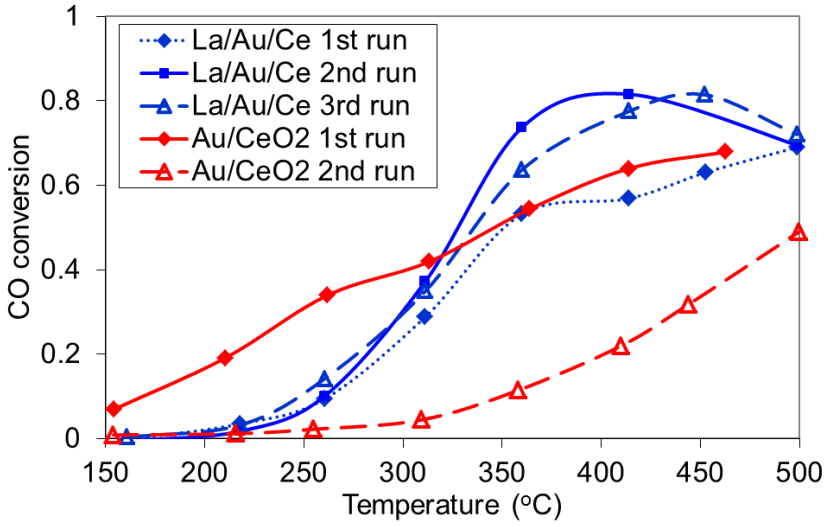

Figure 32. CO conversion of Au/CeO_2 and La_2O_3-deocrated Au/CeO_2 nanoparticles for WGS cycles.

Beyond the stabilization effect, La_2O_3 shows sulfur capturing function in sour WGS (150 ppm H_2S). As shown in Figure 33 (left), Au/CeO_2 suffers from strong deactivation as soon as H_2S is introduced at t = 5 min. In comparison, $La_2O_3/Au/CeO_2$ catalyst shows stable CO conversion in the first ~3 minutes after the H_2S is introduced, as a result of the preferential sulfur capturing of La_2O_3 protective layer. However, after this period of time, the CO conversion starts to decrease, indicating the La_2O_3 is saturated by sulfur and catalyst is deactivated. In addition, it

is observed the deactivation rate of $La_2O_3/Au/CeO_2$ is faster than Au/CeO_2, since the S-saturated La_2O_3 (lanthanum oxysulfide, La_2O_2S) provides S-enriched environment for the encapsulated Au. However, more importantly, gas phase H_2S concentration is suppressed by. For Au/CeO_2, sulfur concentration in gas-phase product increases as soon as H_2S is introduced. In comparison, H_2S concentration remains <10 ppm level (detection limit of mass spectroscopy) for $La_2O_3/Au/CeO_2$ during the first ~8 minutes. The delay of breakthrough illustrates the La_2O_3 effectively captures the H_2S and reduced its concentration from 150 ppm in the feed stream to <10 ppm in the product. It is noticed that the catalyst can suppress the H_2S concentration even after the S-poisoning starts (t = 4-8 min), since the S-poisoning of Au starts before La_2O_3 is completely saturated.

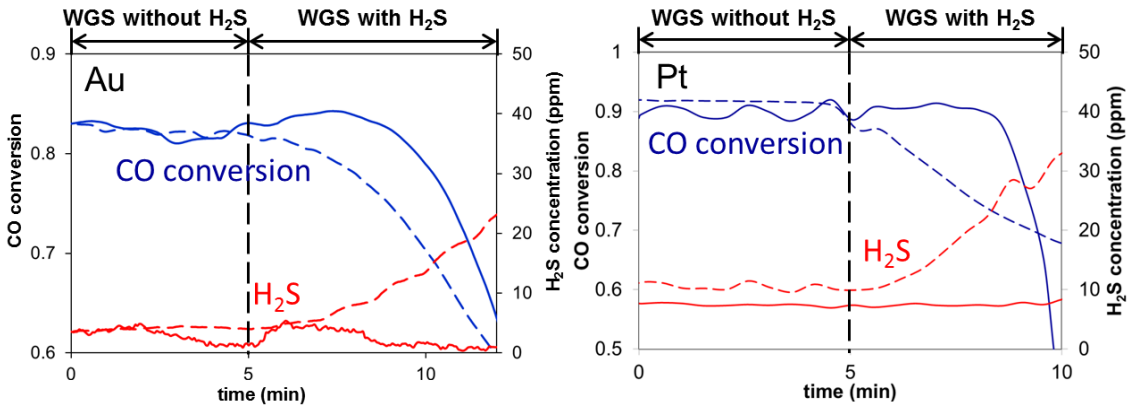

Figure 33. CO conversion of M/CeO_2 (dash), La_2O_3-deocrated M/CeO_2 nanorods (solid) for WGS reaction doped with 150 ppm H_2S. The corresponding H_2S concentration in product is monitored by mass spectroscopy. M = Au (left) and Pt (right)

In addition to Au, Pt-based catalyst were prepared and tested (Figure 33 right). The post-decoration principle shows very similar results: after the La_2O_3 is decorated, the catalysts maintain high activity and reduce the H_2S concentration simultaneously. $La_2O_3/Pt/CeO_2$ also experiences faster deactivation than Pt/CeO_2 after the La_2O_3 decoration is saturated, since the S-capturing by La_2O_3 leads to the formation of S-enriched environment in the vicinity of Pt.

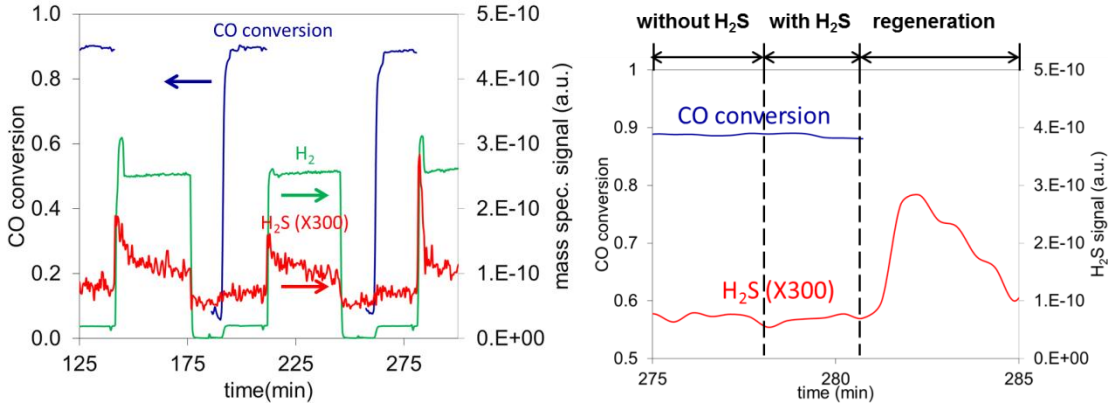

Figure 34. Left: Three-cycle of sour WGS and regeneration of La_2O_3/Pt/CeO_2. The CO conversion, H_2 concentration and H_2S concentration are monitored by mass spectroscopy. Right: The last cycle WGS without H_2S - WGS with H_2S - regeneration. The CO conversion (blue) and H_2S concentration (red) is monitored by mass spectroscopy

Beyond the protective function in single cycle, La_2O_3 can be regenerated and reused in the cyclic sour WGS. As shown in Figure 34, the catalyst is tested in three sour WGS cycles. In one single cycle (fig.5b), La_2O_3/Pt/CeO_2 catalyst firstly shows CO conversion as high as 90% in WGS without H_2S. After the H_2S is introduced, the catalyst maintains the high CO conversion for ~3min, since the decoration layer capture the H_2S and protect the metal nanoparticles. During this period, H_2S concentration in the product is suppressed under the detection limit of mass spectroscopy. Before the catalyst starts deactivation, feed gas is switched from sour WGS feedstocks to H_2 for regeneration. During 30 minutes regeneration, we observed a strong peak of H_2S in gas phase, indicating the sulfur is being released from La_2O_3. After regeneration, the activity of La_2O_3/Pt/CeO_2 was fully recovered, as the CO conversion reaches 90%. As shown in the overview of three cycles, the catalyst maintains its full activity at the end of the evaluation without any deactivation. Therefore, the La_2O_3 does not only capture the sulfur, protect the active metals, but also regenerate in reducing atmosphere.

5.3 SUMMARY

In this work, we have demonstrated a principle to multi-functionalize the conventional M/CeO_2 (M=Au, Pt) catalysts via post-decoration of functional oxide layer. In addition to the stabilization effect to Au nanoparticles, La_2O_3 overlayer shows strong and effective S-capturing ability in sour WGS, resulting in the dramatic decreases of H_2S concentration (150 ppm to <10 ppm). With the protection of La_2O_3, Au and Pt catalysts maintains the high activity in sour WGS. However, after the overlayer is partially saturated by H_2S, the active metals suffer from even faster deactivation due to the S-enriched environment. More importantly, La_2O_3 can be regenerated to restore the S-capturing capacity, which enables the recycling of such multifunctional catalyst. In additional to sulfur capturing, this rational design has a promising potential to incorporate the adsorption of other contaminants or even the undesired product, and hence to improve the conversion or selectivity by tuning the reaction equilibrium.

6.0 DEACTIVATION AND REGENERATION OF PT-BASED CATALYST IN SOUR WATER-GAS SHIFT REACTION

Sulfur poisoning is a major reason to deactivate metal catalysts and to shut down WGS reaction. More importantly, the poisoning of the noble metals can only be partially recovered at mild conditions, such as the temperature of WGS [198] or consequential oxidation-reduction at mild temperature, since the weakly bond between sulfate and catalyst surface [199]. For Pt, which is one of the most studied WGS catalysts, the complete regeneration of S-poisoned Pt is difficult at temperature of 400 ^{o}C [200]. In addition, the effect of oxide supports has been investigated recently in terms of the S-resistance and regeneration. For example, fully recovery of Pt/ZrO_2 has been demonstrated after removal of H_2S from WGS [126]. Very recently, Liu et al. [128] reported that Pt/CeO_2 provides stable high CO conversion closed to equilibrium conversion in sour WGS. They also proposed that the spill-over of the hydrogen on Pt mitigates the destructive effect of sulfur on oxide supports. However, since their reactive gases include relatively low concentration of H_2S (20 ppm) and high concentration of H_2 (45 vol%), the deactivation was not obvious due to the simultaneous S-poisoning and regeneration. Although the S-poisoning and regeneration of Pt-based catalysts have been widely acknowledged, the mechanism of the regeneration has not been clearly demonstrated due to the simultaneous S-poisoning and regeneration under reaction condition.

In our current study, we are aiming at a better understanding of Pt-based catalysts' performance in sour WGS and regeneration. Pt/Al_2O_3 and Pt/CeO_2 with different morphologies (particles and rods) were prepared, characterized, and tested in sour WGS. The impact of oxide supports to the regeneration is investigated by hydrogen-temperature program reduction.

6.1 EXPERIMENTAL SECTION

6.1.1 Catalyst preparation

The Pt/CeO_2 catalysts were prepared via a two-step synthesis. The CeO_2 nanoparticles and nanorods were firstly prepared via urea precipitation and hydrothermal, followed by Pt loading via wet-impregnation.

CeO_2 nanoparticles were prepared based on previous reported urea precipitation method [201]. 3.45 g ammonium cerium (IV) nitrate (98.5+%, Sigma-Aldrich) was added and dissolved in 50 ml DI water. 6 g of urea (99.1%, J.T.Baker) was added to the solution, which was then kept boiling until yellow precipitate formed. After the precipitate was observed, additional 100 ml DI water was added. The solution was kept boiling for another 4 h. The precipitate was then filtered, washed with DI water, dried in vacuum over at 80 ^oC overnight. After calcination at 450 ^oC for 4 h, the CeO2 nanoparticle was obtained.

CeO_2 nanorods were prepared based on previous hydrothermal synthesis (as discussed in 4.1.1). Pt/CeO_2 were prepared by wet-impregnation using $Pt(NH_3)_4(NO_3)_2$ (as discussed in 5.1.1).

6.1.2 Characterization

The specific surface area was determined via nitrogen sorption in a Micromeritics ASAP 2020 gas adsorption analyzer using the BET method. Prior to the measurement, the samples were degassed for 2 h at 200 ^{o}C under high vacuum. The X-ray diffraction (XRD) measurements were performed with a high-resolution powder X-ray diffractometer (Phillips PW1830) in line focus mode employing Cu-Kα radiation (λ = 1.5406 Å). Crystal phases were identified based on JCPDS cards. Particle sizes were calculated from the Debye-Scherrer equation. Sample morphology was determined by high resolution transmission electron microscopy (JEOL-2100FX).

6.1.3 Catalyst tests

Water-gas shift tests were carried out in a 5 mm ID quartz glass tube heated inserted into a high-temperature tube furnace at ambient pressure. The catalyst powder (50 mg) was supported within the tube on either end by quartz glass felt plugs. Water was injected via a syringe pump (Braintree Scientific, Inc.) and vaporized in a heated line before entering the reactor. The total flow rate of gas was typically around 100 CCM resulting in space velocities of ~150,000 h^{-1}.

For water-gas shift with H_2S, the exit gas passed through a condenser to eliminate H_2O from the stream and then was continuously analyzed by a mass spectroscopy, Pfeiffer Omnistar equipped with secondary electron multiplier. No methane was detected at any conditions used in this work. The composition of the mixture: WGS without H_2S 10% H_2O, 2% CO, and 88% Ar; WGS with H_2S, 150 ppm H_2S, 10% H_2O, 2 % CO, and 88% Ar; regeneration, 25% H_2, 10% H_2O, 65% Ar.

Temperature-programmed reduction by hydrogen (H_2-TPR) was conducted in the fixed-bed reactor immediately after sour WGS. Sample was cooled down to room temperature under Ar flow, and then heated at a rate of 10 ℃/min from room temperature to 450 ℃ in 1% H_2/Ar. The exit gas during the whole procedure was monitored using mass spectrometry (Balzers Quadstar GSD 300) for time resolved, quantitative measurement of gas composition.

6.2 RESULTS AND DISCUSSION

6.2.1 Characterization

Table 10. BET surface area (measured by N_2 sorption) of oxides and Pt-based catalysts

	oxides	Pt-based catalysts
CeO_2 (NP)	119.5	108.6
CeO_2 (NR)	99.0	97.4
γ-Al_2O_3	77.8	59.8

The BET surface areas of all oxides and catalysts are summarized in Table 10. The commercial γ-Al_2O_3 shows the lowest surface area of 77.8 m^2/g, whereas the CeO_2 nanoparticle prepared by urea-precipitation has the highest surface area of 119.5 m^2/g. Upon deposition of Pt, the trend in surface area remains unchanged, although absolute values for all three decrease slightly. Especially for γ-Al_2O_3, the surface area of which decreases the most (>20%) among three catalysts, indicating that the Pt nanoparticles are well dispersed on the supports but may result in some pore blockage.

The XRD spectra of all catalyst samples only reflect the metal-free oxide supports' diffraction patters – CeO_2 and Al_2O_3 (Figure 35). However, no obvious Pt peaks were detected, indicating that the Pt particles are too small to be detected by XRD in all samples (< 3 nm). The

high-resolution TEM (HRTEM) further confirmed the small particle size of Pt-Al_2O_3 of 1.4 nm, as shown in Figure 36-b (inserted). However, for Pt/CeO_2, depicting of Pt particles was widely hindered by the strong contrast of CeO_2 lattice under HRTEM. After careful examination, we could not find any particle form of Pt on CeO_2 nanoparticles or nanorods. More interestingly, fast Fourier transform (FFT) analysis of HRTEM (Figure 36-c inserted) can only identify CeO_2 lattice: (111), (200), (220) and (311) without any indication of Pt lattice. In addition, the elemental analysis (EDX) was carried out in this selected sample area (50 by 50 nm), and characterized the Pt content of 0.82 wt%. Based on the observations of XRD and HRTEM with FFT, Pt on CeO_2 forms well-dispersed sub-nanometer clusters, which are much smaller than the nanoparticles on γ-Al_2O_3. Such observations are also in agreement with previous results by Nagai et al., which demonstrated Pt/CeO_2 is more sintering resistant than Pt/Al_2O_3, since Pt-O-Ce performs as the anchor site and stabilizes the Pt [202].

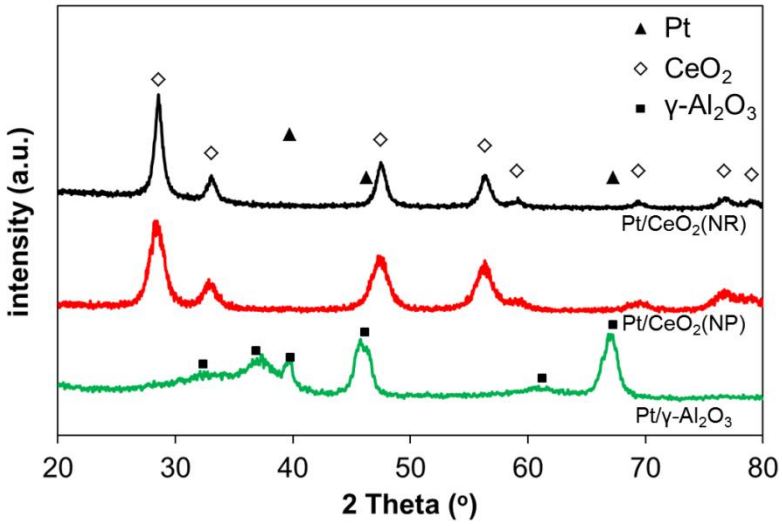

Figure 35. XRD of Pt/Al_2O_3, Pt/CeO_2 (nanorods), Pt/CeO_2 (nanoparticles) after calcination at 400 ^oC

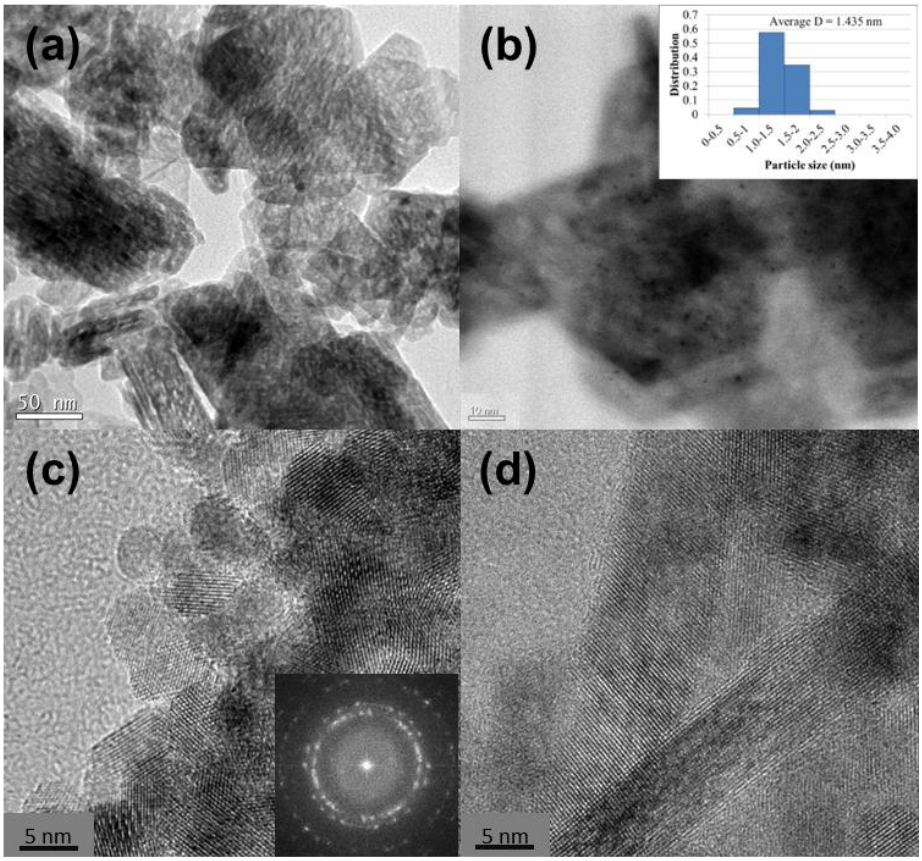

Figure 36. TEM of (a) Al_2O_3 (b) Pt/Al_2O_3 (c) Pt/CeO_2 nanoparticles (d) Pt/CeO_2 nanorods

6.2.2 Sour WGS and regeneration

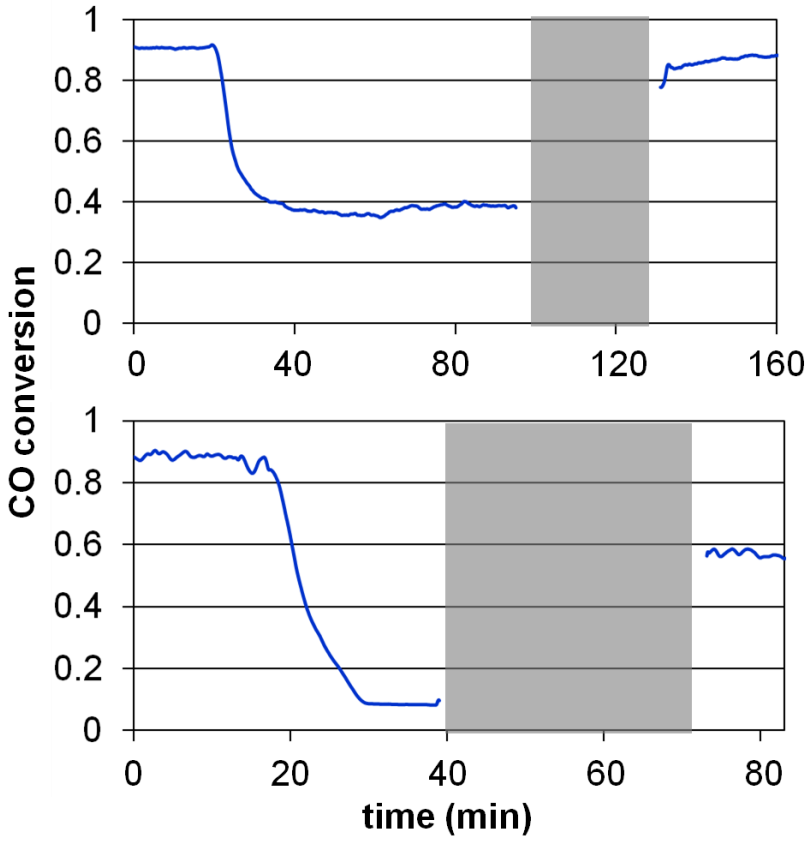

Figure 37. CO conversion profiles of Pt/CeO_2 (top), Pt/Al_2O_3 (bottom) during WGS, sour WGS with 150 ppm H_2S and after 30-min H_2 regeneration (grey bar) at 450 ^oC.

Figure 37 shows the CO conversions of Pt/CeO_2 (nanorods) and Pt/Al_2O_3 in WGS at temperature of 450 ^oC. In WGS without H_2S during the first 20 minutes, both catalysts show similar initial activity (~90% conversion). Subsequently, in presence of 150 ppm of H_2S, the catalysts immediately start deactivation due to sulfur poisoning. However, the final sour WGS conversions are different: the CO conversion of Pt/Al_2O_3 decreases to 10% during sour WGS, whereas Pt/CeO_2 maintains 40% of its initial activity, indicating a dynamic equilibrium between S-poisoning and regeneration in WGS condition at 450 ^oC. It is also noticed that the deactivation of Pt/Al_2O_3 completes much faster than Pt/CeO_2 (10 vs. 30 min), indicating the simultaneous

regeneration of Pt/CeO_2 is more effective than Pt/Al_2O_3. After 30 minutes regeneration with H_2 at 450 ^oC (grey bar), WGS without H_2S was carried out again. The CO conversions of both catalysts rapidly increase to their steady levels: ~90% for Pt/CeO_2 and 60% for Pt/Al_2O_3, indicating the different regeneration abilities under reducing atmosphere. The overall test demonstrates although the high temperature WGS activities (no S) of Pt/Al_2O_3 and Pt/CeO_2 are very similar, their performances in sour WGS are dramatically different due to the regeneration abilities.

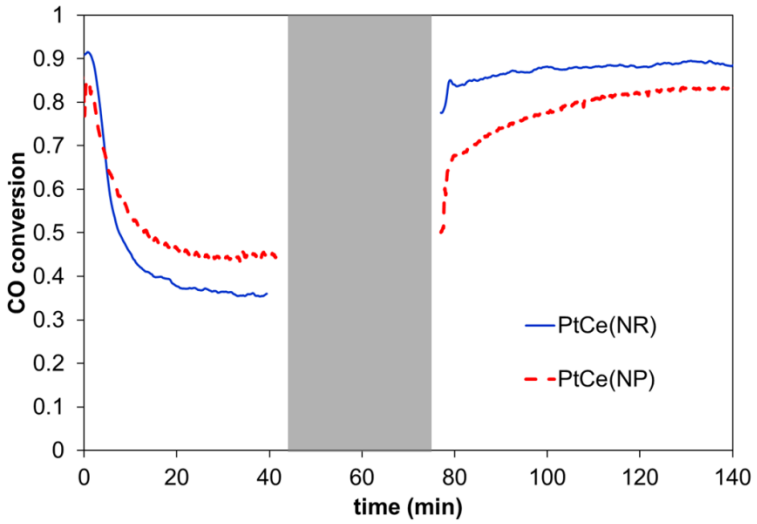

Figure 38. CO conversion profiles of Pt/CeO_2 nanorods (NR, solid), Pt/CeO_2 nanoparticles (NP, dashed).

As discussed in chapter 4.0 , the shape of ceria strongly determines the WGS activity due to the reducibilities of different exposed surfaces. In order to understand the shape effect to the S-poisoning and regeneration, we carried out the sour WGS-regeneration test of Pt/CeO_2 nanorods and nanoparticles. The CO conversion profiles are summarized in Figure 38. Firstly, it is noticed that the initial activity of Pt/CeO_2 nanorods is slightly higher than the nanoparticles. However, when the H_2S is introduced to the reaction, Pt/CeO_2 nanoparticles reach a higher dynamic equilibrium CO conversion of 45%, which is ~10% higher than the nanorods catalyst. In addition, after H_2 regeneration (grey bar), Pt/CeO_2 nanoparticles with higher sour WGS

activity show slow recovery of the activity: the CO conversion after regeneration is only 70% compared with 85% of Pt/CeO_2 nanorods. Subsequently, the CO conversion of Pt/CeO_2 nanoparticles gradually increases from 70% to 85% in the following hour, indicating the regeneration under reaction condition. In contrast, Pt/CeO_2 nanorods show higher CO conversion after regeneration and smaller increase of CO conversion (<5%). The re-increase of CO conversion in the following WGS indicates Pt/CeO_2 nanoparticles are less regenerated than Pt/CeO_2 nanorods during the regeneration.

6.2.3 H_2-TPR after WGS

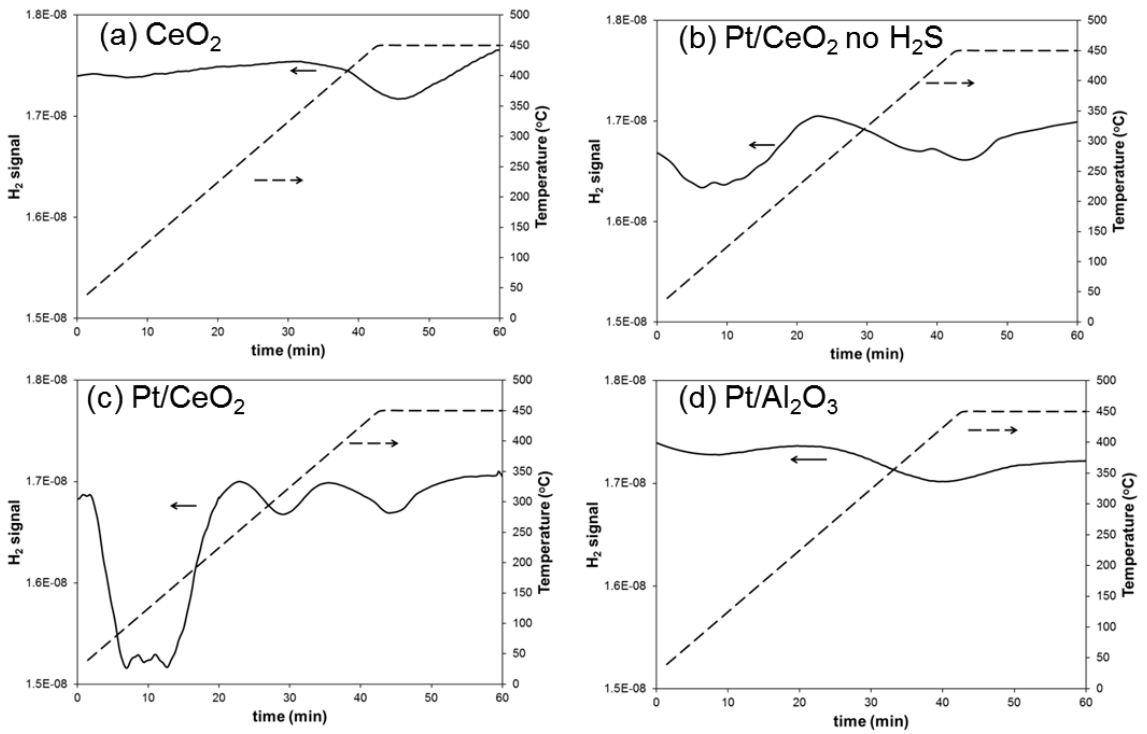

Figure 39. H_2 signal (solid) and temperature profile (dashed) of H_2-TPR: (a) CeO_2 after sour WGS, (b) Pt/CeO_2 (nanorods) after WGS, (c) Pt/CeO2 (nanorods) after WGS without H_2S, (d) Pt/Al_2O_3 after sour WGS.

In order to understand the regeneration mechanism, hydrogen temperature program reduction (H_2-TPR) was carried out immediately after the sour WGS or WGS without H_2S. It is worth to

notice that although the catalysts were partially reduced in WGS, the H_2 treatment includes two simultaneous reactions: the reduction (H_2 (g) + O (s) = H_2O (g)) and the regeneration of catalyst (H_2 (g) + S (s) = H_2S (g)). As shown in Figure 39-a, CeO_2 after sour WGS shows only one H_2 consumption peak at 450 ^oC. In contrast, the reduction/regeneration of Pt/CeO_2 after sour WGS occurs at much lower temperature (~50 ^oC) with a large peak area, indicating the hydrogen consumption of 340.1 μmol/g·cat (Figure 39-c). To differentiate the reduction and regeneration, Pt/CeO_2 was tested in H_2-TPR after the WGS without H_2S, which only reflects the reduction of catalyst. As show in Figure 39-c, the reduction of Pt/CeO_2 starts as low as 30 ^oC with a H_2 consumption of 107.7 μmol/g·cat. The difference between H_2 consumptions of Figure 39 c and d can be exclusively attributed to the removal of sulfur (regeneration). As a result, such difference (340.1 μmol/g·cat vs. 107.7 μmol/g·cat) indicates the cerium oxysulfide (CeOS) or cerium sulfide (CeS_2) is more reducible than the CeO_2 by hydrogen.

The difference in onset temperatures (50 ^oC vs. 30 ^oC) between Figure 39 c and d demonstrates the reduction/regeneration requires higher energy to overcome the barrier after sour WGS. It is also noticed that the H_2 consumptions of Pt/CeO_2 after WGS or sour WGS are both higher than the reduction/regeneration of Pt (102.52 μmol/g·cat), indicating the H_2 is consumed through the spill-over of molecular hydrogen on Pt and the regeneration of cerium sulfide or oxysulfide.

In addition to the major reduction peak at low temperature, Pt/CeO_2 has two other peaks at 320 ^oC and 450 ^oC. However, only the 450 ^oC peak can be found on pure CeO_2 and Pt/CeO_2 without H_2S, which is attributed to the reduction of the supports (CeO_2 to Ce_2O_3). In contrast, since the peak at 320 ^oC cannot be found in either sulfated CeO_2 or unsulfated Pt/CeO_2, it can be explained by the removal of sulfur in the area that is too far from Pt sites and can only be

regenerated by gas phase H_2. It is observed that the hydrogen consumption for this peak is only 33.7 μmol/g·cat, which is less than 10% of the major peak at low temperature (340.1 μmol/g·cat). We believe the high Pt dispersion plays a significant role, which enables the molecular hydrogen from spill-over to reach most surface area and to remove the sulfur species.

In contrast, as shown in Figure 39-d, sulfurized Pt/Al_2O_3 shows two broad and weak H_2 consumption peaks at ~100 ^oC and ~400 ^oC. The low temperature peak can be attributed to the regeneration of Pt as found in Pt/CeO_2, although the peak area (consumption) is much lower than sulfated. The removal of surface sulfur on Al_2O_3 occurs at a higher temperature of 400 ^oC, which is in agreement with previous reports by Apesteguia et al.[203, 204]. This reduction peak can be explained as the result of sulfur-aided strong metal-support interaction (SMSI), since the sulfated Al_2O_3 can only be regenerated at 650–680 ℃ [203]. By comparing the Figure 39 c and d, it is clear to see the SMSI plays a significant role in the regeneration of Pt-based catalyst. The Pt-O-Ce bond has been reported as a very strong interaction and as the active site for the WGS. During the regeneration of sulfated Pt-based catalyst, Pt/CeO_2 with such bond requires low energy to overcome the barrier and release the sulfur. In contrast, the Pt/Al_2O_3 with relatively weak interaction is regenerated at higher temperature. In addition, the high metal dispersion is another result of SMSI, since the interaction can stabilize the metal during high temperature reaction.

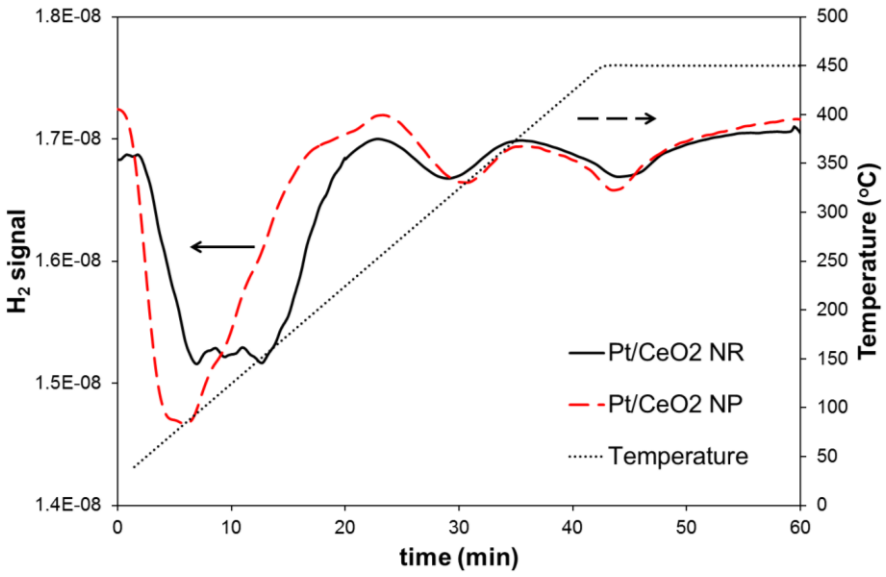

Figure 40. H_2 signal (solid and dashed) and temperature profile (dotted) of H_2-TPR after sour WGS: Pt/CeO_2 nanorods (NR, solid) and Pt/CeO_2 nanoparticles (NP, dashed).

As discussed in 6.2.2, Pt/CeO_2 nanorods and nanoparticles shows different sour WGS activity and regeneration rate. To further investigate the shape effect, the H_2-TPR of sulfurized Pt/CeO_2 nanorods and nanoparticles were carried out and shown in Figure 40. Compared with the nanorods, Pt/CeO_2 nanoparticles have similar onset temperature but higher H_2 consumption (396.3 μmol/g·cat vs. 340.1 μmol/g·cat). It is worth to mention that the surface area can affect the H_2 consumption. The Pt/CeO_2 nanoparticles with higher surface area than nanorods (108.6 m^2/g vs. 97.4 m^2/g) can capture more sulfur and consume more H_2 during the TPR. The high temperature reduction peaks also show slight difference in regeneration temperature. However, the nanorods show lower peak position at 300 ^oC, compared with 325 ^oC for nanoparticles. Since the weight loadings of Pt on both supports are the same, such difference can be attributed to the difference in the number of cluster per surface area or the size of cluster. If the Pt has different number of clusters per surface area, the value is higher on nanorods due to the lower surface area. As a result, the Pt/CeO_2 nanorods should exhibit higher reactivity, which is not the case here. In contrast, the size of cluster can explain the results consistently. Since the nanorods have

low surface area, the average size of Pt clusters on nanorods is larger than that on nanoparticles. The large size of Pt leads to the low reactivity and efficiency in the regeneration, which is in consistent with the current observations (Figure 40). However, since the speculation is only based on H_2-TPR, further investigation is necessary to provide more information such as Pt cluster size.

6.3 SUMMARY

The present study aims to elucidate the impact of oxide supports on the sour WGS activity and regeneration ability of Pt-based catalysts. By utilizing XRD and TEM with FFT, we are able identify different Pt dispersions on Al_2O_3 and CeO_2, which plays an important role not only in the WGS reaction but also in the regeneration of sulfated catalysts. The sour WGS and regeneration tests demonstrate the Pt/CeO_2 is more sulfur-resistant and regenerative after sour WGS than Pt/Al_2O_3.

The investigation of H_2-TPR reveals even after sulfur-poisoning, Pt can be desulfurized at a temperature lower than 100 ^oC, and consequently perform as the active site for H_2 spill-over, which produce atomic hydrogen that efficiently removes sulfur from the support. The oxygen mobility of CeO_2 nanorods and nanoparticles is proposed as the main reason for the different regeneration abilities.

Overall, the study demonstrates that the oxide supports have strong impact on the Pt-based catalyst's sour WGS activity, and determines the regeneration ability of sulfur-poisoned catalysts. The high metal dispersion and strong metal-support interaction, which allow the Pt/CeO_2 maintains partial activity in sour WGS and recovers full initial activity after

regeneration, might ultimately open the way towards a more rational design of sour WGS catalysts.

7.0 OUTLOOK

7.1 HIGHLY ACTIVE WGS CATALYST

Despite lingering controversies regarding reaction mechanisms and active sites for different WGS catalyst systems, as discussed in introduction, a rather consistent picture emerges from the current state of the knowledge on this reaction system: Improved WGS activity of nanocatalyst with increasing metal/support interface was reported in many studies [50, 51, 68, 69, 97, 98, 188, 205, 206], suggesting that for most WGS catalysts this interface houses the active site for the rate limiting step and thus leading to a clearly defined, rational design strategy for WGS catalysts. For example, decreasing the size of the active metals (through the addition of promoters or similar measures) increases metal dispersion and hence the number of active sites located at the interface. However, increasing metal dispersion also results in decreased thermal stability, and hence requires structuring of the metal/oxide interface in order to stabilize the metal nanoparticles. As discussed in 1.5.1, encapsulating metal nanoparticles in oxide shells is an efficient way to achieve this, yielding not only good stability but also improved activity due to the increased interfaces in comparison to conventional supported catalyst [96, 97, 100, 101]. However, it should be pointed out that the porosity of the encapsulation layer or shell is critical to leave the metal particle accessible and minimize mass transport limitations. Given the fast kinetics of WGS on highly active catalysts, such as Au- or Pt-based catalyst systems, careful

design of such encapsulated catalysts is required to balance minimization of mass transport limitations with maximizing the metal-support interface.

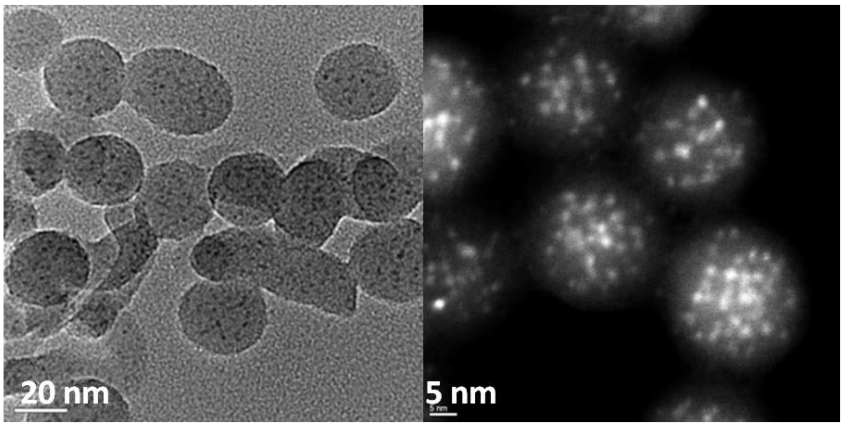

Figure 41. Ni@SiO_2 core-shell catalysts with 1.2 nm Ni cluster (left: bright-field TEM, right: dark-field TEM)

Recently, our group has prepared core-shell catalysts with different active metals, such as Ni (Figure 41), Cu and Pd. Although the shell is SiO_2, which is not an active support for WGS catalyst, recent advances in the synthesis of nanomaterials provide several promising approaches to prepare shell with other active metal oxides such as CeO_2, ZrO_2 and TiO_2 [97, 101, 207]. The major challenge is the much less well-developed understanding and hence difficult control of the hydrolysis of the respective precursors. In addition, it is worth to notice that although several recent studies reported the synthesis of nanocatalysts with metal particles encapsulated by active oxides, the structures of these materials often lacked thorough characterization or, where characterized, did not show the desired uniform morphology due to poor control over the encapsulation step. Moving beyond the reporting of individual nanostructures to the derivation of robust and transferrable synthesis protocols would be a major step towards an accelerated, rational development of nanocatalysts.

7.2 MUTIFUNCTIONAL WGS CATALYST

In addition to the high activity, another key consideration of current WGS catalyst design is the stability and robustness with cyclic operation and sulfur contaminant due to the promising application of WGS in fuel cells [208, 209]. As discussed in 5.2, we have demonstrated a principle of multifunctional S-capturing WGS catalyst, which maintains the high activity during cyclic sour WGS. However, this catalyst could not meet the technical requirements, since the time of sour WGS period is very short compared with the regeneration period. The ratio is ~1: 10, which indicate an insufficient protection against H_2S. We have attributed the main reason to the La_2O_3 overlayer, which randomly deposits on the catalyst surface. Consequently, the performance of such layered catalyst can be dramatically improved via the tailoring of thickness of protective La_2O_3 and the improving of the encapsulation morphology.

The synthesis technique we currently use is the hydrolysis of lanthanum isopropoxide, an air-sensitive and expensive precursor. The hydrolysis occurs preferentially on the surface of M/CeO_2 due to the surface OH^- groups. However, as discussed in 5.2, the large La_2O_3 cluster/particles and thin layer (<5 nm) were both formed during the hydrolysis synthesis, indicating a less well-controlled process. Although previous reports have shown available techniques such as atomic layer deposition (ALD) [114, 210], they usually require unique devices such as ultra-high vacuum (UHV) chamber and repeated time-consuming steps to achieve desired coating thickness. To the best of our knowledge, the lack of broadly applicable, well-understood, and well-established synthesis strategies is currently a limiting factor.

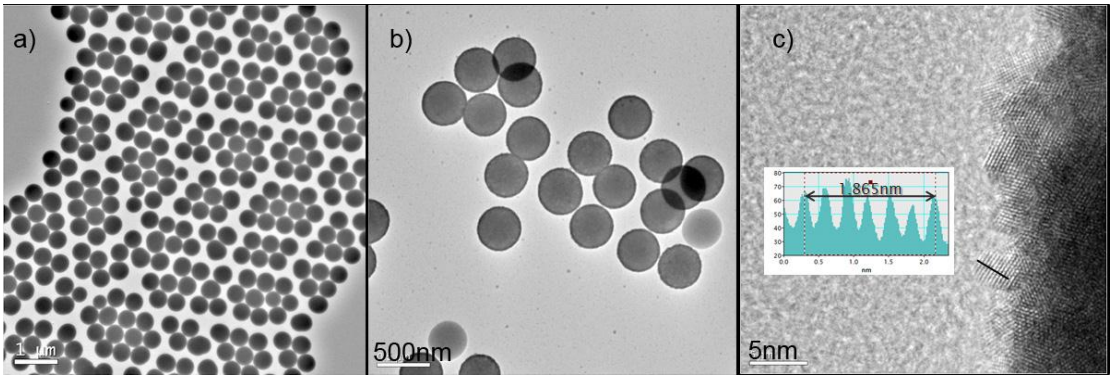

Figure 42. TEM images of a) SiO_2 sphere, b) SiO_2@CeO_2 and c) high resolution TEM image of CeO_2 shell.

Recently, we have tried a relatively simple but promising synthesis route reported by Strandwitz et al. [207] to deposit rare oxide on the surface of another oxide. In the first attempt, CeO_2 coated SiO_2 sphere (SiO_2@CeO_2) was successfully synthesized via a relatively straightforward hydrothermal method. Figure 42-a shows the SiO_2 with uniform diameter of ~200 nm from Stöber method. The silanol groups on the SiO_2 sphere surface act as anchor sites for the hydrolysis of cerium oxides in the following hydrothermal synthesis. It is worth to notice that the concentration of the silanol group is a key factor to control the uniform coating of CeO_2. Proper thermal treatment is necessary to tailor this concentration by inducing condensation reaction between two silanol groups forming a siloxane. As a result of this tailoring process, CeO_2 nanoparticles form 20 nm-thick layer on the surface of SiO_2 (Figure 42-b). The intensity scan (inserted in Figure 42-c) over the line shown in black yields a spacing between peaks of 18.6 / 7= 3.1Å corresponding to the (111) plane spacing (3.1Å) of CeO_2. Although the materials are CeO_2 on SiO_2 in our current attempt, the synthesis of La_2O_3 on CeO_2 could be prepared with similar method with modifications, and show high stability and robustness against sulfur contaminant.

7.3 TAILORING OF SUPPORTED CATALYST

Although the current research mainly focused on WGS reaction, the fundamental methodologies and techniques can be applied to supported catalysts designed for other reactions. Since the catalyst supports can be involved directly in reaction, the tailoring of support's properties is an effective way to improve the catalyst performance.

An effective synthesis of homogenous mixture is an essential requirement for the tailoring of catalyst composition. Based on our current research, the microemulsion synthesis has been demonstrated as an outstanding method to prepare high surface area mixed oxide supports, such as barium-hexaluminates (BHA) and $La_xCe_{1-x}O_y$. Consequently, this method should be easily applied for other systems, such as doped ZrO_2 and TiO_2. More importantly, considering the cost of reducible or rare earth oxides, the microemulsion is more efficient than traditional techniques co-precipitation and sol-gel syntheses in preparation of highly dispersed CeO_2 in Al_2O_3 or SiO_2. After the formation of oxide support, it is expected that the active metals can be preferentially supported on CeO_2 because of the strong metal-ceria interaction.

In addition, the hydrothermal synthesis is relatively simple and straightforward to control the shape of oxide on nanoscale without using excessive amount of structuring agents. The well-defined crystal structure from hydrothermal condition enables the investigation of the impact behind the shape and morphology–surface orientation, which fundamentally determines not only the activity but also the stability and robustness of nanocatalysts.

APPENDIX A

PARAMETERS FOR GC AND CALCULATIONS OF CONVERSION

For this reaction system the inlet concentrations of H_2, He, CO and CO_2 are determined by feeding the reaction mixture to the GC directly while bypassing the reactor at room temperature. CO conversion in general is defined as:

$$X_{CO} = \frac{CO_{in} - CO_{out}}{CO_{in}}$$

The GC used is an Agilent 3000A Micro GC. It is capable of measuring the composition of CH_4, O_2, N_2, H_2, CO, CO_2, ethane, ethylene, and acetylene. H_2O must be condensed prior to entering the GC system in order to prevent column degradation and inaccurate calculations. The parameters for the GC system are listed in Table 11. Channel 1 (Molecular sieve column) is able to separate H_2, He and CO, while channel 2 (Plot U column) is able to analyze CO_2.

Table 11. GC parameter for WGS

Parameter	Channel 1	Channel 2
Carrier gas	Argon	He
Column type	Molecular Sieve	Plot U
Injection type	Backflush	Fixed volume
Inlet temperature	40 ℃	40 ℃
Injection temperature	250 ℃	200 ℃
Column temperature	110 ℃	70 ℃
Detector type	TCD	TCD
Detector sensitivity	Standard	High
Column pressure	40 psi	15 psi
Post run pressure	40 psi	25 psi
Backflush time	9.5 s	---
Sample time	10 s	10 s
Injection time	10 ms	30 ms
Run time	150 s	120 s
Post-run time	10 s	60 s

BIBLIOGRAPHY

[1] G. Ertl, Chemistry for the 21st Century, VCH-Wiley, Weinheim, 2001.

[2] R. Schlögl, S.B. Abd Hamid, Angew. Chem., Int. Ed. 43 (2004) 1628-1637.

[3] D. Zhao, J. Feng, Q. Huo, N. Melosh, G.H. Fredrickson, B.F. Chmelka, G.D. Stucky, Science 279 (1998) 548-552.

[4] D. Zhao, Q. Huo, J. Feng, B.F. Chmelka, G.D. Stucky, J. Am. Chem. Soc. 120 (1998) 6024-6036.

[5] A. Cao, R. Lu, G. Veser, Phys. Chem. Chem. Phys. 12 (2010) 13499-13510.

[6] M. Kirchhoff, U. Specht, G. Veser, Nanotechnology 16 (2005) S401-S408.

[7] T. Sanders, P. Papas, G. Veser, Chem. Eng. J. 142 (2008) 122-132.

[8] J. Schicks, D. Neumann, U. Specht, G. Veser, Catal. Today 81 (2003) 287-296.

[9] G. Veser, Catal. Today 157 (2010) 24-32.

[10] R. Burch, Phys. Chem. Chem. Phys. 8 (2006) 5483-5500.

[11] C. Ungermann, V. Landis, S.A. Moya, H. Cohen, H. Walker, R.G. Pearson, R.G. Rinker, P.C. Ford, J. Am. Chem. Soc. 101 (1979) 5922-5929.

[12] D. Hickman, E. Haupfear, L. Schmidt, Catal. Lett. 17 (1993) 223-237.

[13] W. Vielstich, A. Lamm, H.A. Gasteiger, Handbook of fuel cells : fundamentals, technology, and applications, Wiley, Chichester, 2003.

[14] C. Song, Catal. Today 77 (2002) 17-49.

[15] P. Koci, M. Schejbal, J. Trdlicka, T. Gregor, M. Kubicek, M. Marek, Catal. Today 119 (2007) 64-72.

[16] P. Koci, F. Plat, J. Stepanek, S. Bartova, M. Marek, M. Kubicek, V. Schmeisser, D. Chatterjee, M. Weibel, Catal. Today 147 (2009) S257-S264.

[17] P. Mannila, T. Salmi, H. Haario, M. Luoma, M. Harkonen, J. Sohlo, Appl. Catal., B 7 (1996) 179-198.

[18] B. Whittington, C. Jiang, D. Trimm, Catal. Today 26 (1995) 41-45.

[19] F. Bustamante, R.M. Enick, A.V. Cugini, R.P. Killmeyer, B.H. Howard, K.S. Rothenberger, M.V. Ciocco, B.D. Morreale, S. Chattopadhyay, S. Shi, AIChE J. 50 (2004) 1028-1041.

[20] A. Trovarelli, Catal. Rev. - Sci. Eng. 38 (1996) 439-520.

[21] C. Ratnasamy, J.P. Wagner, Catal. Rev. - Sci. Eng. 51 (2009) 325 - 440.

[22] X. Wang, R.J. Gorte, J.P. Wagner, J. Catal. 212 (2002) 225-230.

[23] S. Hilaire, X. Wang, T. Luo, R.J. Gorte, J. Wagner, Appl. Catal., A 215 (2001) 271-278.

[24] Y. Li, Q. Fu, M. Flytzani-Stephanopoulos, Appl. Catal., B 27 (2000) 179-191.

[25] T. Shido, Y. Iwasawa, J. Catal. 141 (1993) 71-81.

[26] G. Jacobs, U.M. Graham, E. Chenu, P.M. Patterson, A. Dozier, B.H. Davis, J. Catal. 229 (2005) 499-512.

[27] G. Jacobs, P.M. Patterson, U.M. Graham, A.C. Crawford, B.H. Davis, Int. J. Hydrogen Energy 30 (2005) 1265-1276.

[28] C.M. Kalamaras, S. Americanou, A.M. Efstathiou, J. Catal. 279 (2011) 287-300.

[29] F.C. Meunier, D. Tibiletti, A. Goguet, S. Shekhtman, C. Hardacre, R. Burch, Catal. Today 126 (2007) 143-147.

[30] D.C. Grenoble, M.M. Estadt, D.F. Ollis, J. Catal. 67 (1981) 90-102.

[31] G. Germani, Y. Schuurman, AIChE J. 52 (2006) 1806-1813.

[32] O. Thinon, F. Diehl, P. Avenier, Y. Schuurman, Catal. Today 137 (2008) 29-35.

[33] J.A. Rodriguez, Catal. Today 160 (2011) 3-10.

[34] M. Haruta, N. Yamada, T. Kobayashi, S. Iijima, J. Catal. 115 (1989) 301-309.

[35] M. Haruta, Catal. Today 36 (1997) 153-166.

[36] M. Haruta, M. Dat, Appl. Catal., A 222 (2001) 427-437.

[37] M. Haruta, T. Kobayashi, H. Sano, N. Yamada, Chem. Lett. 16 (1987) 405-408.

[38] J. Hua, Q. Zheng, Y. Zheng, K. Wei, X. Lin, Catal. Lett. 102 (2005) 99-108.

[39] A.A. Herzing, C.J. Kiely, A.F. Carley, P. Landon, G.J. Hutchings, Science 321 (2008) 1331-1335.

[40] Q. Fu, H. Saltsburg, M. Flytzani-Stephanopoulos, Science 301 (2003) 935-938.

[41] Q. Fu, W. Deng, H. Saltsburg, M. Flytzani-Stephanopoulos, Appl. Catal., B 56 (2005) 57-68.

[42] Z.-P. Liu, S.J. Jenkins, D.A. King, Phys. Rev. Lett. 94 (2005) 196102.

[43] G. Jacobs, S. Ricote, P.M. Patterson, U.M. Graham, A. Dozier, S. Khalid, E. Rhodus, B.H. Davis, Appl. Catal., A 292 (2005) 229-243.

[44] J. Rodriguez, X. Wang, P. Liu, W. Wen, J. Hanson, J. Hrbek, M. Pérez, J. Evans, Top. Catal. 44 (2007) 73-81.

[45] H. Daly, A. Goguet, C. Hardacre, F.C. Meunier, R. Pilasombat, D. Thompsett, J. Catal. 273 (2010) 257-265.

[46] C. Mohr, H. Hofmeister, J. Radnik, P. Claus, J. Am. Chem. Soc. 125 (2003) 1905-1911.

[47] A. Karpenko, R. Leppelt, V. Plzak, R.J. Behm, J. Catal. 252 (2007) 231-242.

[48] W. Deng, A.I. Frenkel, R. Si, M. Flytzani-Stephanopoulos, J. Phys. Chem. C 112 (2008) 12834-12840.

[49] J.A. Rodriguez, S. Ma, P. Liu, J. Hrbek, J. Evans, M. Pérez, Science 318 (2007) 1757-1760.

[50] J.A. Rodriguez, J. Graciani, J. Evans, J.B. Park, F. Yang, D. Stacchiolam, S.D. Senanayake, S. Ma, M. Pérez, P. Liu, J.F. Sanz, J. Hrbek, Angew. Chem., Int. Ed. 48 (2009) 8047-8050.

[51] L. Barrio, M. Estrella, G. Zhou, W. Wen, J.C. Hanson, A.B. Hungria, A. Hornes, M. Fernandez-Garcia, A. Martinez-Arias, J.A. Rodriguez, J. Phys. Chem. C 114 (2010) 3580-3587.

[52] P. Liu, J. Chem. Phys. 133 (2010) 204705.

[53] S.D. Senanayake, D. Stacchiola, J. Evans, M. Estrella, L. Barrio, M. Perez, J. Hrbek, J.A. Rodriguez, J. Catal. 271 (2010) 392-400.

[54] K.G. Azzam, I.V. Babich, K. Seshan, L. Lefferts, J. Catal. 251 (2007) 163-171.

[55] Y. Sato, K. Terada, S. Hasegawa, T. Miyao, S. Naito, Appl. Catal., A 296 (2005) 80-89.

[56] R. Radhakrishnan, R.R. Willigan, Z. Dardas, T.H. Vanderspurt, Appl. Catal., B 66 (2006) 23-28.

[57] S.Y. Choung, M. Ferrandon, T. Krause, Catal. Today 99 (2005) 257-262.

[58] X. Zhu, T. Hoang, L.L. Lobban, R.G. Mallinson, Appl. Catal., B 94 (2010) 311-317.

[59] S. Sato, J.M. White, J. Catal. 69 (1981) 128-139.

[60] J.M. Pigos, C.J. Brooks, G. Jacobs, B.H. Davis, Appl. Catal., A 319 (2007) 47-57.

[61] Y. Zhai, D. Pierre, R. Si, W. Deng, P. Ferrin, A.U. Nilekar, G. Peng, J.A. Herron, D.C. Bell, H. Saltsburg, M. Mavrikakis, M. Flytzani-Stephanopoulos, Science 329 (2010) 1633-1636.

[62] X. Zhu, M. Shen, L.L. Lobban, R.G. Mallinson, J. Catal. 278 (2011) 123-132.

[63] A.M. Duarte de Farias, A.P.M.G. Barandas, R.F. Perez, M.A. Fraga, J. Power Sources 165 (2007) 854-860.

[64] A.M. Duarte de Farias, P. Bargiela, M.d.G.C. Rocha, M.A. Fraga, J. Catal. 260 (2008) 93-102.

[65] W. Ruettinger, X. Liu, X. Xu, R. Farrauto, Top. Catal. 51 (2008) 60-67.

[66] P.A. Deshpande, M.S. Hegde, G. Madras, Appl. Catal., B 96 (2010) 83-93.

[67] Y.T. Kim, E.D. Park, H.C. Lee, D. Lee, K.H. Lee, Appl. Catal., B 90 (2009) 45-54.

[68] J.B. Park, J. Graciani, J. Evans, D. Stacchiola, S. Ma, P. Liu, A. Nambu, J.F. Sanz, J. Hrbek, J.A. Rodriguez, Proc. Natl. Acad. Sci. U.S.A. 106 (2009) 4975-4980.

[69] J.B. Park, J. Graciani, J. Evans, D. Stacchiola, S.D. Senanayake, L. Barrio, P. Liu, J.F. Sanz, J. Hrbek, J.A. Rodriguez, J. Am. Chem. Soc. 132 (2009) 356-363.

[70] T. Baidya, A. Gayen, M.S. Hegde, N. Ravishankar, L. Dupont, J. Phys. Chem. B 110 (2006) 5262-5272.

[71] M.B. Boucher, S. Goergen, N. Yi, M. Flytzani-Stephanopoulos, Phys. Chem. Chem. Phys. 13 (2011) 2517-2527.

[72] Y. Xin, Y. Qi, X. Ma, Z. Wang, Z. Zhang, S. Zhang, Mater. Lett. 64 (2010) 2659-2662.

[73] M. Hatanaka, N. Takahashi, T. Tanabe, Y. Nagai, K. Dohmae, Y. Aoki, T. Yoshida, H. Shinjoh, Appl. Catal., B 99 (2010) 336-342.

[74] H. Sakurai, T. Akita, S. Tsubota, M. Kiuchi, M. Haruta, Appl. Catal., A 291 (2005) 179-187.

[75] E.S. Bickford, S. Velu, C. Song, Catal. Today 99 (2005) 347-357.

[76] A. Luengnaruemitchai, S. Osuwan, E. Gulari, Catal. Commun. 4 (2003) 215-221.

[77] D. Andreeva, V. Idakiev, T. Tabakova, L. Ilieva, P. Falaras, A. Bourlinos, A. Travlos, Catal. Today 72 (2002) 51-57.

[78] Y. Wang, S. Liang, A. Cao, R.L. Thompson, G. Veser, Appl. Catal., B 99 (2010) 89-95.

[79] P. Panagiotopoulou, D.I. Kondarides, Appl. Catal., B 101 (2011) 738-746.

[80] P. Panagiotopoulou, D.I. Kondarides, J. Catal. 225 (2004) 327-336.

[81] Q.-L. Tang, Z.-P. Liu, J. Phys. Chem. C 114 (2010) 8423-8430.

[82] S. Ricote, G. Jacobs, M. Milling, Y. Ji, P.M. Patterson, B.H. Davis, Appl. Catal., A 303 (2006) 35-47.

[83] B.M. Reddy, A. Khan, Y. Yamada, T. Kobayashi, J. Phys. Chem. B 107 (2003) 11475-11484.

[84] P. Panagiotopoulou, D.I. Kondarides, Catal. Today 112 (2006) 49-52.

[85] G. Balducci, M.S. Islam, J. Kaspar, P. Fornasiero, M. Graziani, Chem. Mater. 12 (2000) 677-681.

[86] G. Balducci, M.S. Islam, J. Kaspar, P. Fornasiero, M. Graziani, Chem. Mater. 15 (2003) 3781-3785.

[87] L. Linganiso, V. Pendyala, G. Jacobs, B. Davis, D. Cronauer, A. Kropf, C. Marshall, Catal. Lett. 141 (2011) 1723-1731.

[88] G. Balducci, J. Kaspar, P. Fornasiero, M. Graziani, M.S. Islam, J. Phys. Chem. B 102 (1998) 557-561.

[89] A. Corma, P. Atienzar, H. Garcia, J.-Y. Chane-Ching, Nat. Mater. 3 (2004) 394-397.

[90] P. Panagiotopoulou, A. Christodoulakis, D.I. Kondarides, S. Boghosian, J. Catal. 240 (2006) 114-125.

[91] C. Loschen, S.T. Bromley, K.M. Neyman, F. Illas, J. Phys. Chem. C 111 (2007) 10142-10145.

[92] T. Janssens, B. Clausen, B. Hvolbæk, H. Falsig, C. Christensen, T. Bligaard, J. Nørskov, Top. Catal. 44 (2007) 15-26.

[93] V. Idakiev, Z.Y. Yuan, T. Tabakova, B.L. Su, Appl. Catal., A 281 (2005) 149-155.

[94] R. Si, M. Flytzani-Stephanopoulos, Angew. Chem., Int. Ed. 47 (2008) 2884-2887.

[95] K. Zhou, X. Wang, X. Sun, Q. Peng, Y. Li, J. Catal. 229 (2005) 206-212.

[96] C.M.Y. Yeung, S.C. Tsang, J. Phys. Chem. C 113 (2009) 6074-6087.

[97] C.M.Y. Yeung, S.C. Tsang, J. Mol. Catal. A: Chem. 322 (2010) 17-25.

[98] C.M.Y. Yeung, K.M.K. Yu, Q.J. Fu, D. Thompsett, M.I. Petch, S.C. Tsang, J. Am. Chem. Soc. 127 (2005) 18010-18011.

[99] C. Yeung, S. Tsang, Catal. Lett. 128 (2009) 349-355.

[100] M. Cargnello, N.L. Wieder, T. Montini, R.J. Gorte, P. Fornasiero, J. Am. Chem. Soc. 132 (2009) 1402-1409.

[101] M. Cargnello, T. Montini, S. Polizzi, N.L. Wieder, R.J. Gorte, M. Graziani, P. Fornasiero, Dalton Trans. 39 (2010) 2122-2127.

[102] N.L. Wieder, M. Cargnello, K. Bakhmutsky, T. Montini, P. Fornasiero, R.J. Gorte, J. Phys. Chem. C 115 (2010) 915-919.

[103] T.S. Kim, J. Gong, R.A. Ojifinni, J.M. White, C.B. Mullins, J. Am. Chem. Soc. 128 (2006) 6282-6283.

[104] A. Gayen, M. Boaro, C.d. Leitenburg, J. Llorca, A. Trovarelli, J. Catal. 270 (2010) 285-298.

[105] J.E. Martin, J. Odinek, J.P. Wilcoxon, R.A. Anderson, P. Provencio, J. Phys. Chem. B 107 (2002) 430-434.

[106] P. Buffat, J.P. Borel, Phys. Rev. A 13 (1976) 2287-2298.

[107] A. Goguet, R. Burch, Y. Chen, C. Hardacre, P. Hu, R.W. Joyner, F.C. Meunier, B.S. Mun, D. Thompsett, D. Tibiletti, J. Phys. Chem. C 111 (2007) 16927-16933.

[108] A. Cao, G. Veser, Nat. Mater. 9 (2010) 75-81.

[109] X. Liu, A. Wang, X. Yang, T. Zhang, C.-Y. Mou, D.-S. Su, J. Li, Chem. Mater. 21 (2008) 410-418.

[110] Z. Ma, S. Dai, ACS Catal. 1 (2011) 805-818.

[111] M.A. Pablo, C. Massimiliano, S. Ferdi, Angew. Chem., Int. Ed. 118 (2006) 8404-8407.

[112] W. Yan, S.M. Mahurin, Z. Pan, S.H. Overbury, S. Dai, J. Am. Chem. Soc. 127 (2005) 10480-10481.

[113] Z. Ma, S. Brown, J.Y. Howe, S.H. Overbury, S. Dai, J. Phys. Chem. C 112 (2008) 9448-9457.

[114] S.N. Rashkeev, S. Dai, S.H. Overbury, J. Phys. Chem. C 114 (2010) 2996-3002.

[115] Y. Dai, B. Lim, Y. Yang, C.M. Cobley, W. Li, E.C. Cho, B. Grayson, P.T. Fanson, C.T. Campbell, Y. Sun, Y. Xia, Angew. Chem., Int. Ed. 49 (2010) 8165-8168.

[116] E. Xue, M. O'Keeffe, J.R.H. Ross, Catal. Today 30 (1996) 107-118.

[117] C.T. Campbell, B.E. Koel, Surf. Sci. 183 (1987) 100-112.

[118] Y. Okamoto, Catal. Today 39 (1997) 45-59.

[119] L. Zhang, J.-M.M. Millet, U.S. Ozkan, J. Mol. Catal. A: Chem. 309 (2009) 63-70.

[120] Y.S. Chen, C. Xie, Y. Li, C.S. Song, T.B. Bolin, Phys. Chem. Chem. Phys. 12 (2010) 5707-5711.

[121] K. Lee, C.S. Song, M.J. Janik, Appl. Catal., A 389 (2010) 122-130.

[122] J.A. Schaidle, A.C. Lausche, L.T. Thompson, J. Catal. 272 (2010) 235-245.

[123] J. Boon, E. van Dijk, Ö. Pirgon-Galin, W. Haije, R. van den Brink, Catal. Lett. 131 (2009) 406-412.

[124] J.J. Strohm, J. Zheng, C. Song, J. Catal. 238 (2006) 309-320.

[125] A.-M. Azad, M.J. Duran, Appl. Catal., A 330 (2007) 77-88.

[126] E. Xue, M. O'Keeffe, J.R.H. Ross, in: F.V.M.S.M. Avelino Corma, G.F. José Luis (Eds.), Stud. Surf. Sci. Catal., Elsevier, 2000, pp. 3813-3818.

[127] T. Luo, R.J. Gorte, Catal. Lett. 85 (2003) 139-146.

[128] B. Liu, A. Goldbach, H. Xu, Catal. Today 171 (2011) 304-311.

[129] S. Arrii, F. Morfin, A. Renouprez, J. Rousset, J. Am. Chem. Soc. 126 (2004) 1199-1205.

[130] W. Deng, C. Carpenter, N. Yi, M. Flytzani-Stephanopoulos, Top. Catal. 44 (2007) 199-208.

[131] Q. Fu, A. Weber, M. Flytzani-Stephanopoulos, Catal. Lett. 77 (2001) 87-95.

[132] J.A. Rodriguez, P. Liu, J. Hrbek, J. Evans, M. Perez, Angew. Chem., Int. Ed. 46 (2007) 1329-1332.

[133] T. Bunluesin, R. Gorte, G. Graham, Appl. Catal., B 15 (1998) 107-114.

[134] A. Kozlov, D. Kim, A. Yezerets, P. Andersen, H. Kung, M. Kung, J. Catal. 209 (2002) 417-426.

[135] A. Bueno-Lopez, K. Krishna, M. Makkee, J. Moulijn, J. Catal. 230 (2005) 237-248.

[136] C. Bozo, N. Guilhaume, J. Herrmann, J. Catal. 203 (2001) 393-406.

[137] M.F. Wilkes, P. Hayden, A.K. Bhattacharya, J. Catal. 219 (2003) 305-309.

[138] J.S. Bae, W.K. Choo, C.H. Lee, J. Eur. Ceram. Soc. 24 (2004) 1291-1294.

[139] K.M. Ryan, J.P. McGrath, R.A. Farrell, W.M.O. Neill, C.J. Barnes, M.A. Morris, J. Phys.: Condens. Matter (2003) L49-L58.

[140] S. Dikmen, P. Shuk, M. Greenblatt, Solid State Ionics 126 (1999) 89-95.

[141] P.G. Harrison, A. Kelsall, J.V. Wood, J. Sol-Gel Sci. Technol. 13 (1998) 1049-1055.

[142] B.C. Morris, W.R. Flavell, W.C. Mackrodt, M.A. Morris, J. Mater. Chem. 3 (1993) 1007-1013.

[143] V. Belliere, G. Joorst, O. Stephan, F.M.F. de Groot, B.M. Weckhuysen, J. Phys. Chem. B 110 (2006) 9984-9990.

[144] M.P. Pileni, Langmuir 13 (1997) 3266-3276.

[145] M. Fanun, Microemulsions: properties and applications, CRC Press, Boca Raton, 2009.

[146] A.J. Zarur, J.Y. Ying, Nature 403 (2000) 65-67.

[147] D.M. Lyons, L.P. Harman, M.A. Morris, J. Mater. Chem. 14 (2004) 1976-1981.

[148] J. Sheng, S. Zhang, S. Lv, W. Sun, J. Mater. Sci. 42 (2007) 9565-9571.

[149] S. Lacombe, C. Geantet, C. Mirodatos, J. Catal. 151 (1995) 439-452.

[150] X. Luo, R. Wang, J. Ni, J. Lin, B. Lin, X. Xu, K. Wei, Catal. Lett. 133 (2009) 382-387.

[151] M. Flytzani-Stephanopoulos, M. Sakbodin, Z. Wang, Science 312 (2006) 1508-1510.

[152] G.A.H. Mekhemer, B.A.A. Balboul, Colloids Surf., A 181 (2001) 19-29.

[153] S. Bernal, F.J. Botana, R. Garc á, J.M. Rodr guez-Izquierdo, React. Solid. 4 (1987) 23-40.

[154] K.S.W. Sing, D.H. Everett, R.A.W. Haul, L. Moscou, R.A. Pierotti, J. Rouquerol, T. Siemieniewska, Pure Appl. Chem. 57 (1985) 603-619.

[155] S. Lowell, J.E. Shields, M.A. Thomas, M. Thommes, Characterization of porous solids and powders: surface area, pore size and density, Kluwer Academic Publishers, Dordrecht, 2004.

[156] Z. Wang, M. Flytzani-Stephanopoulos, Energy Fuels 19 (2005) 2089-2097.

[157] A. Thurber, K.M. Reddy, V. Shutthanandan, M.H. Engelhard, C. Wang, J. Hays, A. Punnoose, Phys. Rev. B 76 (2007) 165206.

[158] X.D. Zhou, W. Huebner, Appl. Phys. Lett. 79 (2001) 3512-3514.

[159] S. Patil, S. Seal, Y. Guo, A. Schulte, J. Norwood, Appl. Phys. Lett. 88 (2006) 243110-243113.

[160] G. Dutta, U.V. Waghmare, T. Baidya, M.S. Hegde, K.R. Priolkar, P.R. Sarode, Chem. Mater. 18 (2006) 3249-3256.

[161] D. Terribile, A. Trovarelli, C. de Leitenburg, G. Dolcetti, J. Llorca, Chem. Mater. 9 (1997) 2676-2678.

[162] X. Wang, G. Lu, Y. Guo, L. Jiang, Y. Guo, C. Li, J. Mater. Sci. 44 (2009) 1294-1301.

[163] P. Burroughs, A. Hamnett, A.F. Orchard, G. Thornton, J. Chem. Soc., Dalton Trans. (1976) 1686-1698.

[164] A. Trovarelli, Catalysis by ceria and related materials, Imperial College Press, London, 2002.

[165] R. Fuentes, L. Acuna, M. Zimic, D. Lamas, J. Sacanell, A. Leyva, R. Baker, Chem. Mater. 20 (2008) 7356-7363.

[166] X. Wang, M. Wang, H. Song, B. Ding, Mater. Lett. 60 (2006) 2261-2265.

[167] S. Scire, S. Minico, C. Crisafulli, C. Satriano, A. Pistone, Appl. Catal., B 40 (2003) 43-49.

[168] Q. Fu, S. Kudriavtseva, H. Saltsburg, M. Flytzani-Stephanopoulos, Chem. Eng. J. 93 (2003) 41-53.

[169] V. Idakiev, T. Tabakova, A. Naydenov, Z. Yuan, B. Su, Appl. Catal., B 63 (2006) 178-186.

[170] A. Sandoval, A. Gomez-Cortes, R. Zanella, G. Diaz, J. Saniger, J. Mol. Catal. A: Chem. 278 (2007) 200-208.

[171] S. Collins, J. Cies, E. del Rio, M. Lopez-Haro, S. Trasobares, J. Calvino, J. Pintado, S. Bernal, J. Phys. Chem. C 111 (2007) 14371-14379.

[172] F. Boccuzzi, A. Chiorino, M. Manzoli, D. Andreeva, T. Tabakova, J. Catal. 188 (1999) 176-185.

[173] D. Mullins, S. Overbury, J. Catal. 188 (1999) 340-345.

[174] Z. Pu, X. Liu, A. Jia, Y. Xie, J. Lu, M. Luo, J. Phys. Chem. C 112 (2008) 15045-15051.

[175] L. Liotta, M. Ousmane, G. Di Carlo, G. Pantaleo, G. Deganello, G. Marci, L. Retailleau, A. Giroir-Fendler, Appl. Catal., A 347 (2008) 81-88.

[176] E. Fox, S. Velu, M. Engelhard, Y. Chin, J. Miller, J. Kropf, C. Song, J. Catal. 260 (2008) 358-370.

[177] L. Ilieva, G. Pantaleo, I. Ivanov, R. Nedyalkova, A.M. Venezia, D. Andreeva, Catal. Today 139 (2008) 168-173.

[178] C.M. Ho, J.C. Yu, X.C. Wang, S.Y. Lai, Y.F. Qiu, J. Mater. Chem. 15 (2005) 2193-2201.

[179] R. Di Monte, J. Kaspar, J. Mater. Chem. 15 (2005) 633-648.

[180] G.R. Rao, J. Kašpar, S. Meriani, R. Monte, M. Graziani, Catal. Lett. 24 (1994) 107-112.

[181] C. de Leitenburg, A. Trovarelli, J. Llorca, F. Cavani, G. Bini, Appl. Catal., A 139 (1996) 161-173.

[182] S. Liang, E. Broitman, Y. Wang, A. Cao, G. Veser, J. Mater. Sci. 46 (2011) 2928-2937.

[183] H.-X. Mai, L.-D. Sun, Y.-W. Zhang, R. Si, W. Feng, H.-P. Zhang, H.-C. Liu, C.-H. Yan, J. Phys. Chem. B 109 (2005) 24380-24385.

[184] K.-S. Lin, S. Chowdhury, Int. J. Mol. Sci. 11 (2010) 3226-3251.

[185] F. Niu, D. Zhang, L. Shi, X. He, H. Li, H. Mai, T. Yan, Mater. Lett. 63 (2009) 2132-2135.

[186] Y. Yang, X. Wang, C. Sun, L. Li, J. Am. Ceram. Soc. 93 (2010) 2555-2559.

[187] F. Zhang, Q. Jin, S.W. Chan, J. Appl. Phys. 95 (2004) 4319-4326.

[188] F. Lin, D. Hoang, C.-K. Tsung, W. Huang, S. Lo, J. Wood, H. Wang, J. Tang, P. Yang, Nano Res. 4 (2011) 61-71.

[189] D.C. Sayle, S.A. Maicaneanu, G.W. Watson, J. Am. Chem. Soc. 124 (2002) 11429-11439.

[190] X.-S. Huang, H. Sun, L.-C. Wang, Y.-M. Liu, K.-N. Fan, Y. Cao, Appl. Catal., B 90 (2009) 224-232.

[191] Q. Yuan, H.-H. Duan, L.-L. Li, L.-D. Sun, Y.-W. Zhang, C.-H. Yan, J. Colloid Interface Sci. 335 (2009) 151-167.

[192] B. Klingenberg, M.A. Vannice, Chem. Mater. 8 (1996) 2755-2768.

[193] S. Liang, G. Veser, Nanomaterials and Energy DOI 10.1680/nme.11.00006 (2011).

[194] H. Zhu, Z. Ma, S. Overbury, S. Dai, Catal. Lett. 116 (2007) 128-135.

[195] T. Kanazawa, Catal. Lett. 108 (2006) 45-47.

[196] P. Zhang, M. Chi, S. Sharma, E. McFarland, J. Mater. Chem. 20 (2010) 2013-2017.

[197] K. Nakagawa, Y. Tanimoto, T. Okayama, K.-I. Sotowa, S. Sugiyama, S. Takenaka, M. Kishida, Catal. Lett. 136 (2010) 71-76.

[198] M.-V. Mathieu, M. Primet, Applied Catalysis 9 (1984) 361-370.

[199] K. Föttinger, E. Halwax, H. Vinek, Appl. Catal., A 301 (2006) 115-122.

[200] J.M. Jones, V.A. Dupont, R. Brydson, D.J. Fullerton, N.S. Nasri, A.B. Ross, A.V.K. Westwood, Catal. Today 81 (2003) 589-601.

[201] M. Kobayashi, M. Flytzani-Stephanopoulos, Ind. Eng. Chem. Res. 41 (2002) 3115-3123.

[202] Y. Nagai, T. Hirabayashi, K. Dohmae, N. Takagi, T. Minami, H. Shinjoh, S.i. Matsumoto, J. Catal. 242 (2006) 103-109.

[203] C.R. Apesteguia, T.F. Garetto, A. Borgna, J. Catal. 106 (1987) 73-84.

[204] C.R. Apesteguia, C.E. Brema, T.F. Garetto, A. Borgna, J.M. Parera, J. Catal. 89 (1984) 52-59.

[205] H.-P. Zhou, H.-S. Wu, J. Shen, A.-X. Yin, L.-D. Sun, C.-H. Yan, J. Am. Chem. Soc. 132 (2010) 4998-4999.

[206] N.M. Schweitzer, J.A. Schaidle, O.K. Ezekoye, X. Pan, S. Linic, L.T. Thompson, J. Am. Chem. Soc. 133 (2011) 2378-2381.

[207] N.C. Strandwitz, G.D. Stucky, Chem. Mater. 21 (2009) 4577-4582.

[208] W. Deng, M. Flytzani-Stephanopoulos, Angew. Chem., Int. Ed. 45 (2006) 2285-2289.

[209] X. Liu, W. Ruettinger, X. Xu, R. Farrauto, Appl. Catal., B 56 (2005) 69-75.

[210] X. Liang, J. Li, M. Yu, C.N. McMurray, J.L. Falconer, A.W. Weimer, ACS Catal. 1 (2011) 1162-1165.